Metallic Nanostructures Based on Self-Assembling DNA Templates for Studying Optical Phenomena

by

Mauricio Pilo-Pais

Department of Physics
Duke University

Date: _____

Approved:

_____
Gleb Finkelstein, Supervisor

_____
Thomas LaBean

_____
Harold Baranger

_____
Henry Everitt

_____
Nicholas Buchler

Dissertation submitted in partial fulfillment of the requirements for the degree of
Doctor of Philosophy in the Department of Physics
in the Graduate School of Duke University
2014

Abstract

Metallic Nanostructures Based on Self-Assembling DNA Templates for Studying Optical Phenomena

by

Mauricio Pilo-Pais

Department of Physics
Duke University

Date: _____

Approved:

_____
Gleb Finkelstein, Supervisor

_____
Thomas LaBean

_____
Harold Baranger

_____
Henry Everitt

_____
Nicholas Buchler

An abstract of a dissertation submitted in partial fulfillment of the requirements for the degree of Doctor of Philosophy in the Department of Physics in the Graduate School of Duke University
2014

Abstract

DNA origami is a novel self-assembly technique that can be used to form various 2D and 3D objects, and to position matter with nanometer accuracy. It has been used to coordinate the placement of nanoscale objects, both organic and inorganic; to make molecular motor and walkers; and to create optically active nanostructures. In this dissertation, DNA origami templates are used to assemble plasmonic structures. Specifically, engineered Surface Enhanced Raman Scattering (SERS) substrates were fabricated. Gold nanoparticles were selectively placed on the corners of rectangular origami and subsequently enlarged via solution-based metal deposition. The resulting assemblies exhibited hot spots of enhanced electromagnetic field between the nanoparticles. These hot spots significantly enhanced the Raman signal from Raman molecules covalently attached to the assemblies. Control samples with only one nanoparticle per DNA template, which therefore lacked inter-particle hot spots, did not exhibit strong enhancement. Furthermore, Raman molecules were used to map out the hot spots distribution, as the molecules are photo-damaged when experiencing a threshold electric field. This method opens up the prospect of using DNA origami to rationally engineer and assemble plasmonic structures for molecular spectroscopy.

"I prefer to be a dreamer among the humblest,

with visions to be realized,

than lord among those without dreams and desires."

- Kahlil Gibran

Contents

List of Figures

List of Abbreviations and Symbols

Abbreviations

T_m	Melting Temperature
A	Adenine
AuNPs	Gold Nanoparticles
BME	Boundary Element Method
bp	Basepair
C	Cytosine
cDNA	Complementary Strands
DDA	Discreet Dipole Approximation
dsDNA	double strand DNA
EF	Enhancement Factor
FDTD	Finite Difference Time Domain
G	Guanine
LSPs	Localized Surface Plasmons
MD	Molecular Dynamics
QSA	Quasi-Static Approximation
SERS	Surface Enhanced Raman Scattering
SPPs	Surface Plasmon Polaritons
ssDNA	Single Strand DNA
T	Thymine

Acknowledgements

This project was performed under (the superb) guidance of Prof. Gleb Finkelstein and Prof. Thomas LaBean, from 2009 through 2014. Their intuitive approach toward any subject is simple admirable. I will always be indebted to Gleb for his continuous trust and support throughout my graduate studies.

My current and former labmates provided the required environment to remain sane: Chung-Ting Ke, Anne Watson, Henok Mebrahtu, Ivan Borzenets, Steven Demers, Yuriy Bomze, and Ulas Coskun. I thanks Prof. Enrique Samano for his help during crucial experiments. Special thanks to Sarah Goldberg, who taught me the value of a detailed lab notebook, and the universal truth of *GIGO*: "garbage in, garbage out." I am grateful to Thom's students: Alex Marchi, Ronnie Pedersen, and Briana Vogen for showing me various wet lab techniques. Insightful (and sometimes endless) discussions were possible thanks to a joint journal club with Prof. Reif's students: Sudhanshu Garg, Reem Mokhtar, Hieu Bui, and Tianqui Song.

Thanks to Jack Mock for providing insight towards plasmonics experimentation; and to Cristian Ciraci, and Christos Argyropoulos for showing me the ropes of numerical calculations. I appreciate valuable discussions with Prof. Henry Everitt.

I thank Prof. Maiken Mikkelsen for serving as my M.Sc. degree adviser at the department of Electrical and Computer Engineering. I am very grateful to Prof. Steven Teitsworth, Prof. Joshua Socolar and Prof. Henry Greenside, whom provided me with the required coaching to be successful on my graduate studies.

I acknowledge various sources of funding: Duke GPNANO for a one year fellowship. Salary and work support was possible thanks to the Office of Navy Research, award N000140910249, and the National Science Foundation through the NSF-ECCS-12-32239 award. Travel Funding was granted by FNANO2010, DNA19, and the Duke Graduate School.

Finally, I thank Carolina, who endured my ups and downs as they mirrored my day-to-day experiments. To her, I am grateful for her continuous reminding that despite our best efforts, there is always room for improvement.

Chapter 1

Introduction

The goal of this project is to explore the capabilities and limitations of DNA as a fabrication tool for plasmonic nanostructures. The aim is to present my experimental observations while providing the necessary background of two very distinct fields: Plasmonics and DNA Nanotechnology [96]. Since Seeman's visionary proposal of assembling DNA-based rigid junctions in the early 80's [115], DNA Nanotechnology has matured to a field of its own. DNA can now be pre-programmed to acquire well-defined structures that are functional and/or serve as pathways toward a specific reaction. The advent of DNA-origami [104] further provided functional nano-breadboards. DNA origami is a product of a one-pot reaction in which DNA strands of specific sequences self-assemble into a large structure ($\sim 100\ nm$) of a predetermined shape [104], thereby providing an alternative to conventional top-down fabrication methods. The resulting templates are highly addressable and can serve as versatile tools for site-specific placement of various nanocomponents.

In a different realm, the field of Plasmonics is more than a century old. Recent advances in plasmonics nanofabrication and phenomenological understanding have avalanched the study of exciting phenomena such as plasmon hybridization [32, 101], Surface Enhanced Raman Scattering (SERS) [97], and strong coupling between emitters and absorbers [34, 111]. A wide range of applications are being currently

explored including cancer therapy [9, 41], biosensors [7, 49], and plasmonic waveguides [3, 107].

The construction of nanoscale plasmonic structures requires the controlled placement of metal with nanometer resolution, and the ability to couple to the resulting structures, either electrically or optically. This can be challenging when using a top-down approach such as lithography. One alternative is to use DNA as a building component to self-assemble nanostructures. In fact, DNA Nanotechnology is currently able to produce complex architectures in 1-, 2-, and 3-dimensions, and virtually any shape. There are several clear advantages to using DNA for assembling plasmonic structures:

1. Pre-programmability
2. Self-assembly in solution
3. Retention of functionality after assembly
4. Massive parallel assembly

The rational self-assembly of 10^8 structures upon pipetting a few microliters of solution is undoubtedly striking. There are nonetheless multiple challenges that still need to be addressed. First, although DNA Origami's maximum length is constantly being expanded by using larger scaffolds or clever attachment schemes between subunits, it is still currently limited to a few hundreds of nanometers. Moreover, DNA's lack of rigidity puts it at a great disadvantage compared to other sturdier nano-assembly techniques, jeopardizing its key selling point: DNA's astonishing base-pair precision.

I have decided to explore such limitations toward fabricating precise, functional and robust plasmonic structures. As is the nature of any interdisciplinary research, there is a gap between merging fields. I hope this thesis provides a comprehensive introduction to fill this void. My objective is to provide enough extensive background of to describe my graduate research. Nonetheless, DNA Nanotechnology and Plas-

monics are broad fields, preventing an exhaustive and rigorous review within this thesis. For that I have referred the reader to the appropriate references.

The thesis is divided into two parts. **Part I** discusses DNA as a tool to create functional nanostructures: *Chapter* 2 does a brief survey on DNA self-assembly stepping-stones and introduces to DNA hybridization models. *Chapter* 3 discusses current schemes used to create DNA-functional nanocomponents.

Part II is devoted to the fields of plasmonics and SERS. *Chapter* 4 introduces plasmons and provides models describing the interaction between incident light and spherical metallic nanoparticles. Hybridization of plasmon modes is also described. *Chapter* 5 introduces SERS and discusses the effectiveness of using DNA-based templates as SERS substrates.

Chapter 2

DNA Self-Assembly

In the first section of this chapter I will present an overview of the fundamentals of DNA. First, I will describe two different treatments towards double strand DNA (dsDNA) hybridization: a hamiltonian approach [93] and a two-state model [57, 99]. I will then describe a semi-empirical method [108] widely used to predict DNA's melting temperature (T_m) and structure formation [139]. In the second section I will provide a brief account on how DNA is used as a building block for structural DNA Nanotechnology. Lastly, I will focus on the main part of this chapter: our own contribution towards using DNA origami as a nanobreadboard to fabricate complex metallic nanostructures [96].

2.1 Fundamentals of DNA Self-Assembly

DNA is a fundamental component of living species, responsible for storing the information required to build and maintain individual cells, as well as supra-cellular organisms. Its structural unit is made out of four nitrogenous bases, which are pair complementary: Adenine (A) with Thymine (T), and Guanine (G) with Cytosine (C). An individual nucleoside has its base linked to the 1' carbon of a deoxyribose (sugar). Nucleosides can form ester bonds with phosphates at the 3' and 5' carbons 2.1. A single strand DNA (ssDNA) is a chain of individual nucleosides held

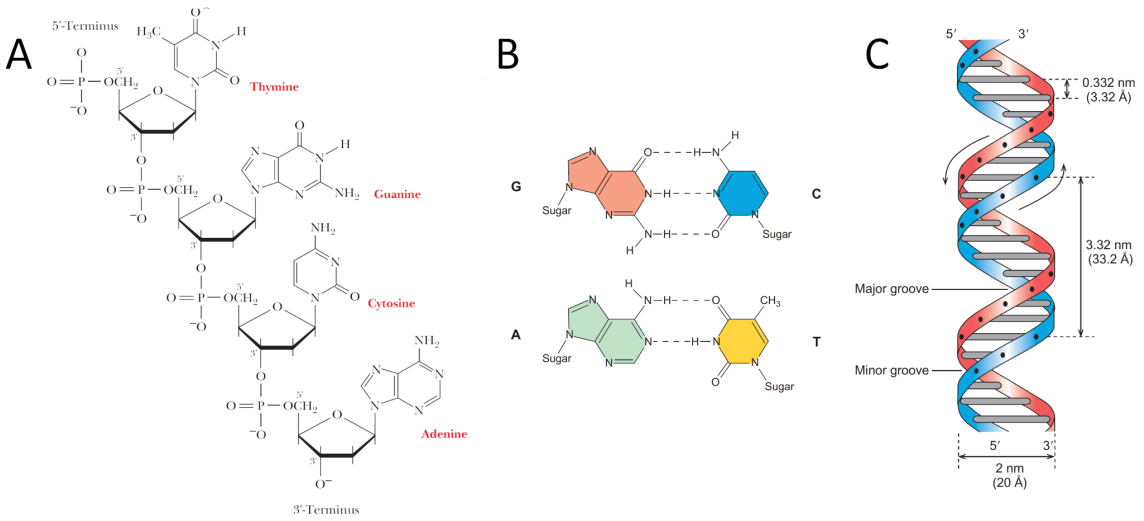

FIGURE 2.1: **a)** Single strand DNA showing four nucleotides: Adenine, Thymine, Guanine, and Cytosine **b)** DNA basepair complementarity: Cytosine-Guanine and ThymineAdenine **c)** Double strand DNA B-helix conformation. The strands run antiparallel and form two distinct groves (major and minor). Figures adapted from Ref. [129].

together through a phosphate-deoxyribose "backbone." The carbon number associated with the phosphodiester bond is used to indicate the directionality of ssDNA. A double strand DNA (dsDNA) is made of two fully complementary ssDNA segments running antiparallel to each other, in a helical conformation. The formation and stability of a duplex structure is mediated by both energy and entropy considerations, as will be explained on detail below. Let's note for now that there are two main electrostatic interactions: i) hydrogen bonding between complementary bases and ii) base-stacking. The most common dsDNA helical conformation is the right handed B-helix, which makes a full turn every 10.4 basepair (bps) or 3.4 nm. Other helical forms are the A-helix and the left handed Z-helix, but these are less stable and therefore transient in nature [82]. More complex configurations such as G-quadruplexes [12] and I-motifs [11] are also possible but will not be discussed here. A very thorough introduction to DNA is provided in Ref. [82]. In this thesis it is assumed that a DNA duplex adopts a B-helix conformation.

DNA Nanotechnology uses DNA as the primary building block, exploiting its

complementarity nature to create supramolecular structures of pre-programmed shape, and functionality. Understanding the underlying mechanisms involved in the binding and stability of interacting DNA strands is crucial for the design of DNA-based structures. Light absorption studies show that DNA hybridization (or denaturation) appears to be a first-order transition as a function of temperature. The transition temperature is commonly referred to as the melting temperature T_m and it is determined by the DNA sequence, length, concentration, and solvent composition. The latter includes the solvent polar strength and permitivity, as well as the presence of ions in solution which contribute to charge screening. Base-pairing and base-stacking both play a crucial role in stabilizing the duplex structure [134]. Base-pairing between $G-C$ contains three hydrogen bonds, adding additional stability compared to its counterpart $A-T$ which contains only two hydrogen bonds. Base-stacking interactions are due to the $\pi-\pi$ interactions between the aromatic rings of neighboring bases. Backbone repulsion also contributes to the T_m of DNA segments. For a large number of DNA strands, the T_m is defined as the temperature at which half the dsDNA are dissociated.

I will now describe two physical treatments towards dsDNA hybridization. The first approach uses a hamiltonian to describe the interactions between parallel strands [93], while the second approach is a two-state model which fully uses statistical thermodynamics [57, 99]. The hamiltonian model was first proposed by Peyrard and Bishop [93]. There are four terms in the hamiltonian:

$$
\begin{aligned}
H = & \sum_n \frac{1}{2}\left(\dot{u}_n^2 + \dot{v}_n^2\right) \\
& + \frac{1}{2}k\left[(u_n - u_{n-1})^2 + (v_n - v_{n-1})^2\right] \\
& + D\left[e^{-a(u_n - v_n)} - 1\right]^2 \\
& + \frac{1}{2}K\left[(u_n - v_{n+1})^2 + (u_n - v_{n-1})^2\right]
\end{aligned}
\tag{2.1}
$$

The first term describes the kinetic energy of the system. The second one is a harmonic coupling term that accounts for base-stacking interactions. The third is a Morse Potential to represent the attractive interactions due to hydrogen bonding between base pairs, as well as repulsion between negatively charged phosphate backbones. More complex potentials can be used to account for the DNA helix stiffness, water presence and ions interactions [94]. The fourth term was introduced by Dauoxois to better account for the helicity of DNA [19]. By providing such an inter-base coupling term, the model was able to better describe DNA breathing fluctuations. Equation 2.1 is known as the Poland-Bishop-Dauoxois (PBD) hamiltonian. The PBD model provides great phenomenological insight towards duplexes formation, and is able to predict a DNA melting transition. Although the model was originally introduced as part of a statistical approach, it has been used in Molecular Dynamics (MD) along with the incorporation of sophisticated potentials. This pursuit has generated criticism for its attempts to solve time-dependent motion of DNA [35]. Although great advances are continuously being done on the MD front, it is highly limited to improvements on computational power: current simulations are on the order of microseconds [92]. In Peyrard and Dauoxois words [95], although the equations of motion can be readily written from the PDB hamiltonian, it would be "hopeless" to expect MD to accurately predict the movement involving several thousand of base pairs. They suggest that the hamiltonian model is better suited

to be solved with a statistical approach. In fact, it has recently been shown that such course can accurately predict melting profiles of large DNA sequences [125]. An alternative approach to MD is to coarse-grain the force fields. The method permits us to access longer time-scales (through faster calculations) at the cost of smoothing the energy landscape (lower resolution) [83]. This type of modeling has already been used to accurately predict various DNA interactions, such as duplex hybridization and toehold mediated strand displacement [25, 85].

The second approach is based on purely statistical thermodynamic grounds: the two-state model (bound or unbound). The formation of a single duplex from two ssDNA is simultaneously enthalpy favorable and entropy unfavorable. Enthalpy is driven by hydrogen bonding between base pairs as well as base-stacking interactions. It is interesting to note that the competition between entropy and enthalpy provides a modest stability of DNA duplexes, crucial for various biological processes such as transcription. The combination of the driving landscapes can be expressed in terms of the Gibbs energy, which is responsible for driving hybridization,

$$\Delta G = \Delta H - T\Delta S \tag{2.2}$$

A complete statistical model that describes DNA hybridization would have to include ΔG_i of all possible configurations. As one expect, the number of configurations sharply increases with the DNA strand length. For example, in the case of two complementary strands of length N, the conformations are not limited between the nth bases of opposite strands ($A_{1,nth}$, $A_{2,nth}$), but must account for all possible configurations, including intra-strand internal loops as well as stem-loops (hairpins).

The partition function could be greatly reduced by restricting DNA's aperture to occur from one end only. Despite its simplicity, the DNA zipper model [57] is able to predict a first order state transition. The energy of the two DNA strands of length

N in a state with n-bps "zipped" is given by,

$$E = \sum_{i=1}^{N} \epsilon_i = -n\epsilon \tag{2.3}$$

The entropy of such state is determined by the number of configurations g for each $(N-n)$ free bases,

$$\begin{aligned} S &= \sum_{n=1}^{N-n} k_B ln g \\ &= -k_B (N-n) ln g \end{aligned} \tag{2.4}$$

The partition function is then given by,

$$\begin{aligned} Z &= \sum_{n=1}^{N} g^n \, e^{-n\epsilon\beta} = \sum_{n=1}^{N} x^n \\ &= \frac{x^{N+1} - 1}{x - 1} \end{aligned} \tag{2.5}$$

where $x = gexp(-n\epsilon\beta)$. The entropy is finally written as,

$$\begin{aligned} \langle S \rangle &= \frac{\sum n x^N}{z} = x \frac{\partial}{\partial x} ln Z \\ &= \frac{N x^N}{x^N - 1} - \frac{x}{x - 1} \end{aligned} \tag{2.6}$$

The degeneracy of an open link g is related to the rotational freedom of each base, and may be up to 10^4 [57].

Poland and Sheraga [99] proposed a more realistic statistical partition function by assigning different weights to the bound and unbound segments. Their main motivation was that DNA strands exhibit local denaturation (breathing bubbles), not present on the zipper model. Bubbles typically occur in segments that are rich in T and A bases. These loops are both, enthalpy favorable, since they release the strain produce by the double helix from the rest of the bounded segment, and

entropy favored. The simplification of the partition function comes from assuming that bound segments are mainly driven by their binding energy while loops are by the number of configurations S_i, entropy. With this simplification the statistical weights are given by,

$$\begin{aligned} e^{S_i T\beta} \quad & unbound(loop) \\ e^{nE\beta} \quad & bound(dsDNA) \end{aligned} \tag{2.7}$$

The partition function acquires the form of,

$$Z_n = \sum_{n=1}^{N} e^{S_i T\beta} e^{-nE\beta} \tag{2.8}$$

Poland and Scheraga resorted to polymer physics to simplify the entropy given by the loops [99]. They provided the entropy S_i for a chain of length i to be,

$$S(i) = k_B[ai - cln(i) + b] \tag{2.9}$$

Solving such a partition function goes beyond the scope of this thesis. One major problem that arises with statistical models is that same base pairs on different DNA sequences do not carry the same equilibrium constants. For example, the coupling strength between base pairs located at the end strands or adjacent to internal loops carry different weights, not to mention base-stacking interactions dependent on the neighboring bases. Moreover, effects such as torsional deformation and bending are hard to incorporate. For these reasons, semi-empirical models based on statistical thermodynamics, such as the *Nearest Neighbor Model* [108], are widely preferred. They are used to predict both structure formation as well as T_m. Let us first describe how can the thermodynamic variables ΔG, ΔH, and ΔS be obtained from experimental melting curves. The Gibbs energy of a given duplex can be found via the thermodynamic relation,

$$\Delta G = \Delta H - T\Delta S = -RTln(K) \tag{2.10}$$

Here, T_m is an experimental observable, while K is the equilibrium constant. For an arbitrary pair of complementary ssDNA strands, we can describe the hybridization process by,

$$dsDNA = ssDNA_1 + ssDNA_2 \tag{2.11}$$

The equilibrium constant K is defined as the products and reactants concentration fraction when equilibrium is reached,

$$K = \frac{[ssDNA_1][ssDNA_2]}{[dsDNA]} \tag{2.12}$$

At the T_m,

$$[dsDNA] = [ssDNA_1] = [ssDNA_2] = [dsDNA]_{initial}/2 \tag{2.13}$$

and the equilibrium constant reduces to $K = 4/[dsDNA]_{initial}$ for non-complementary strands. An additional factor of two must be added for self complementary strands. It is then possible to extract ΔG from experimental melting curves, as well as ΔH and ΔS from measuring T_m vs $[dsDNA]$ curve via,

$$\frac{1}{T_m} = \frac{-RTln(4/[dsDNA])}{\Delta H} - \frac{\Delta S}{\Delta H} \tag{2.14}$$

Different T_m have been obtained by different groups due to variations in DNA and salt concentrations. A Unified Nearest Neighbor model was introduced by SantaLucia Jr. [108, 109], where individual ΔG_{NN} terms describe the Gibbs energy between contiguous base pairs. The model also incorporates initiation terms ($\Delta G_{initiation}$) to account for the formation energy, assumed to start only from the terminal bases. Each empirical G_{NN} value is assumed to account for multiple effects such as hydrogen bonding, base-stacking interactions, and the repulsion between the negatively charged backbones. Additional correction terms can be added to account for duplex self-complementary, as well as for salt and DNA concentrations.

Numerous software packages [5] such as NUPACK [139] and Mfold [146] use experimental ΔG_{NN} values to predict DNA folding. Most of them have the common theme of calculating the Gibbs free energy for each possible configuration, and choosing the predicted structure to be the one with the lowest ΔG. One of the main schemes that DNA nanotechnology uses is to expand upon DNA duplex formation to create complex DNA structures of a desired conformation. Provided that the target structure resides in a global energy minimum, it is possible to fabricate it by following an energy path minimization. However, one has to be careful to avoid local minimum traps. In a laboratory setting, this energy path minimization is accomplished through thermal annealing. The slow cooling of the samples ensures that the system does not get "frozen" into non-desired states. Let's now look at what structures have been realized using the described scheme.

2.2 DNA as a Building block: Structural DNA Nanotechnology

Artificial two-dimensional DNA assemblies provide a programmable methodology for bottom-up fabrication of complex nanostructures [114]. The first artificial DNA structure was proposed in 1982 [115] and experimentally realized the following year [50] by Nadrian Seeman. Inspired by the Holliday Junctions which naturally occur during cell meiosis, Seeman envisioned it was possible to avoid branch migration by eliminating their symmetry, and thus obtaining a rigid four-arm formation (Figure 2.2 A). In 1993, Seeman and Fu introduced a new class of DNA structures (Figure 2.2 B) which they coined double-crossovers (DX) [36]. These consist of two helical domains joined through crossover links, and have become one of the fundamental schemes to assemble DNA structures. More complex designs can be created by expanding the number of arm junctions or using crossovers to link multiple heli-

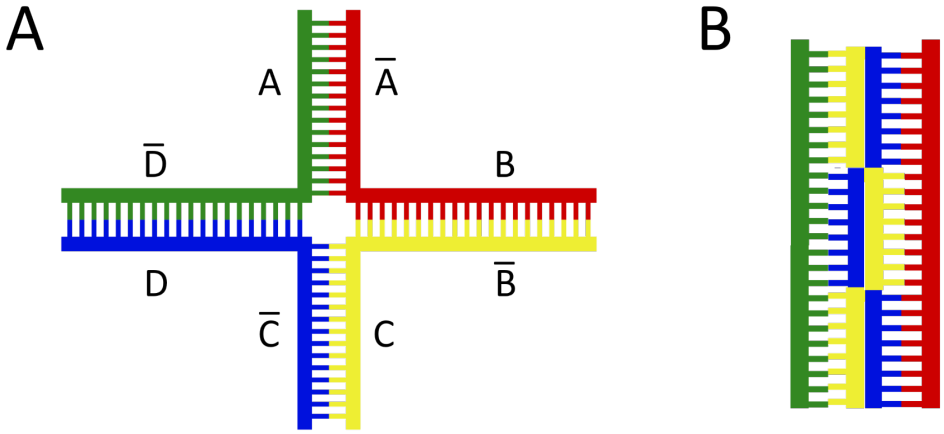

FIGURE 2.2: Artificial DNA structures: **a)** a Four-arm Holliday Junction and **b)** a Double Crossover (DX). Both structures were proposed and experimentally realized by Nadrian Seeman [115, 50, 36].

cal domains. By 1998, Winfree, Seeman and coworkers had fabricated extended tile latices by introducing complementarity between two classes of DX motifs [133]. In 2004, Shih and coworkers were able to controllably fold a 1.7 kilo-base ssDNA into a 3D octahedron. For that, they amplified 40-mer synthetic DNA strands using a polymerases chain reaction (Fig. 2.2 A) [119]. Two years later, the flexibility and addressability of these systems were greatly improved by Paul Rothemund with the advent of scaffolded "DNA origami," a method of creating arbitrary shapes and patterns on a $100x100\ nm^2$ scale (Fig. 2.3 B) [104]. The original origami is composed of a natural DNA strand (scaffold) of approximately 7-kilobase and roughly 200 short synthetic complementary DNA strands, known as "staples." During a one-pot annealing step, these staples fold the scaffold strand back upon itself and determine the shape of the origami. The typical scaffold used to make DNA origami is a circular ssDNA obtained from a bacteriophage (M13mp18). Taking advantage of the DNA B-helical formation, staple crossovers between scaffold segments are located every 1.5 turns (16 bps). This ensures that the staples attach to both of the adjacent helices (Figure 2.3 B). Shih's ssDNA origami [119] is considered a precursor

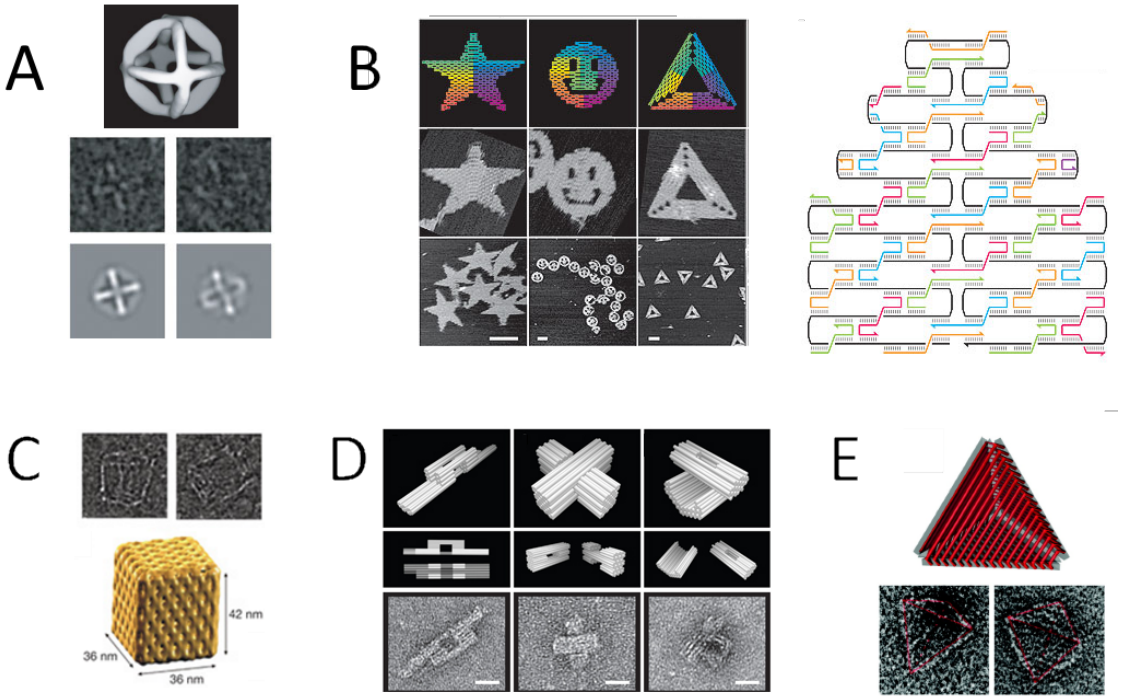

FIGURE 2.3: Progression of DNA Folding Technique: **a)** Single stranded origami, Octahedral (2004) [119] **b)** Scaffolded 2D DNA Origami (2006) [104]. Templates are formed on a single-pot annealing using a 7 kilo-base bacteriophage folded using 200 synthetic DNA strands (32 bases long). Scaffolded 3D DNA Origamis (2009) **c)** A square box with a dynamic lid [5] **d)** A Railed bridge, a slotted cross, and a stacked cross using double helices [24] **e)** A closed faced tetrahedral containers [52].

of Rothemund's staple-based dsDNA origami (Figure 2.3 A). The scaffolded DNA origami technique was later on expanded to three-dimensional structures almost simultaneously by multiple groups [5, 23, 52]. Figures 2.3 C-E show cryogenic TEM images of various three-dimensional DNA origami. The successful formation of DNA origami has been attributed to multiple effects [104]. First, the staple sequences are chosen so that binding between staples is low. Defects are minimized by mixing a large excess of staples per scaffold (typically 10-fold). As previously mentioned, slow thermal annealing prevents trapping the structure on a local minimum conformation; it gives enough time for strand displacement (or invasion) of energy favored staples (i.e. those having greater length of overlap). The formation process is as-

sumed to start when staples with higher T_m act as "seeds" for domain formations, facilitating the binding of subsequent staples [8, 104]. It is interesting to note that since the melting is independent of neighboring staples, it produces a hysteresis on annealing-melting curves. The size of the original DNA origami is limited by the length of the scaffold. For this reason, scaffold-less origamis [51, 130] as well as larger scaffolds [73] have been created. A potential problem with these approaches is that the uniqueness of individual staples strands becomes more difficult as the size of the suprastructure increases. Alternatively, a modular approach can be followed, in which DNA origami serve as tiles [145, 104]. Despite the efforts towards increasing its size, the original DNA origami is sufficiently large to be precisely positioned and oriented on microfabricated substrates, thereby providing a bridge between lithographic and self-assembly methods [44, 54]. Besides structural purposes, DNA can also be used as a dynamic tool. Yurke, Turberfield and coworkers introduced the concept of toehold-strand displacement [138]. With the help of catalytic "fuel" strands, a chain of pre-programmed events can cascade upon the insertion of an initiator strand. Such processes fall under the domain of DNA nanomachines (Fig. 2.4 A). To avoid adding strands, one could store the building components of a larger structure within individual floating DNA strands [22]. Its self-assembly can then be triggered upon introduction of a single initiator strand (Fig. 2.4 B). Hairpins can be used in both instances to store the information required for the pathway of reaction. Reference [141] contains a thorough review of strand-displacement mediated reactions.

2.3 DNA as a Programmable Template

DNA structures can be used to attach nanocomponents using various crosslinkers. One scheme is to use DNA complementarity to attach objects functionalized with complementary strands (cDNA). With DNA origami, the cDNA can naturally

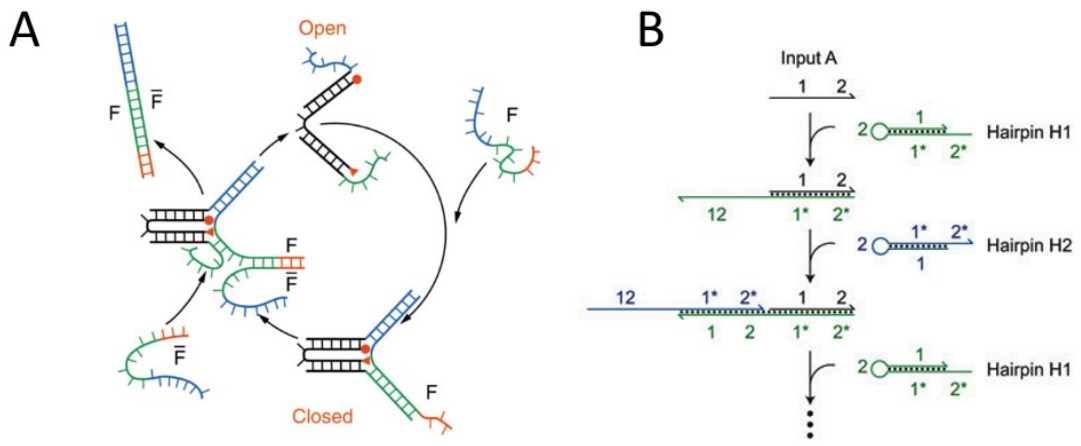

FIGURE 2.4: Not only is DNA used as a structural tool, but can be used to artificially program dynamic pathways **a)** Sequential DNA machine. Through toehold mediated strand displacement one is able to generate a specific output for a given input [138] **b)** Triggered self-assembly of a larger structure using hairpins strand displacement [22].

be an extension of its staple strands. The fact that any of the 200+ staples can be used as a binding site makes DNA origami a versatile programmable breadboard for placement of nanoscale objects. Another common crosslinker used to attach nanocompents onto DNA is through biotin-streptavidin complementarity [15]. DNA origami has already been successfully used as a template for site-specific binding of metallic nanoparticles [21, 43, 86, 87, 96], quantum dots [15], fluorophores [122], and carbon nanotubes [77]. A comprehensive review of attachment of metallic nanocomponents is provided in Ref. [67]. In addition, DNA origami have been used as templates for dynamic processes such as single-molecule chemical reactions [128], DNA motors [126] and "walkers" [38, 70, 131]. Nanocomponents could be further modified after being attached to DNA templates, for example to create metallic wires. Individual DNA strands have been previously metallized by reduction of metal ions from solution, resulting in the formation of conducting wires [53]. Different metals have been deposited, including Ag, Cu, Pd, Pt, and Co (see Ref. [39] for a comprehensive review). Multistrand DNA assemblies have also been metallized, including

DNA nanoribbons [135], DNA nanotubes [91], three-helix bundles [89], and DNA origami [66]. Other methods utilize nanoparticles, assembled using DNA, as templates for metallization [88, 113, 132]. However, in all of these works the reduced metal coated the entire structure, and did not fully utilize the addressability of the underlying DNA template. Our group pursued an alternative approach, in which seed nanoparticles are first attached to the DNA template at specific locations, and are then fused together by metal-on-metal deposition. Specifically, we used DNA origami templates to accurately place gold nanoparticles (AuNPs) that act as nucleation sites for subsequent metal deposition. Furthermore, when AuNPs are positioned sufficiently close, metal ions can fuse neighboring particles into contiguous shapes. This method creates predesigned metallic structures such as rings, pairs of parallel bars, and H-shapes with outer dimensions close to those of the DNA origami.

We used the previously reported "tall rectangle" DNA origami [104] ($90x70\ nm^2$) as the DNA template for all of the metallic structures presented here, but the methodology can be extended to any DNA structure. The origami was formed as originally designed by Rothemund [104], but with the following changes: All of the side staples were left out to prevent aggregation via helix stacking interactions between adjacent origamis (see Supplementary Note S5.7 in Ref. [104]). Additionally, two consecutive staples located at each of the AuNP binding sites were extended on the 3' end by a short spacer sequence (T_5) followed by a specific 24 bases DNA sequence (X_{24}). DNA extensions serve as anchors to attach given nanocomponents; if the anchors are in close proximity to each other then they are considered to be part of the same binding site. As previously mentioned, we use an excess of DNA strands when preparing the DNA template to ensure its proper formation (i.e. minimize vacancies). It is crucial to remove the unused DNA strands during the origami formation, else they will compete with the nanocomponent for attaching to the template. For this reason, the prepared DNA origami (5 nM) was filtered by performing five buffer exchanges

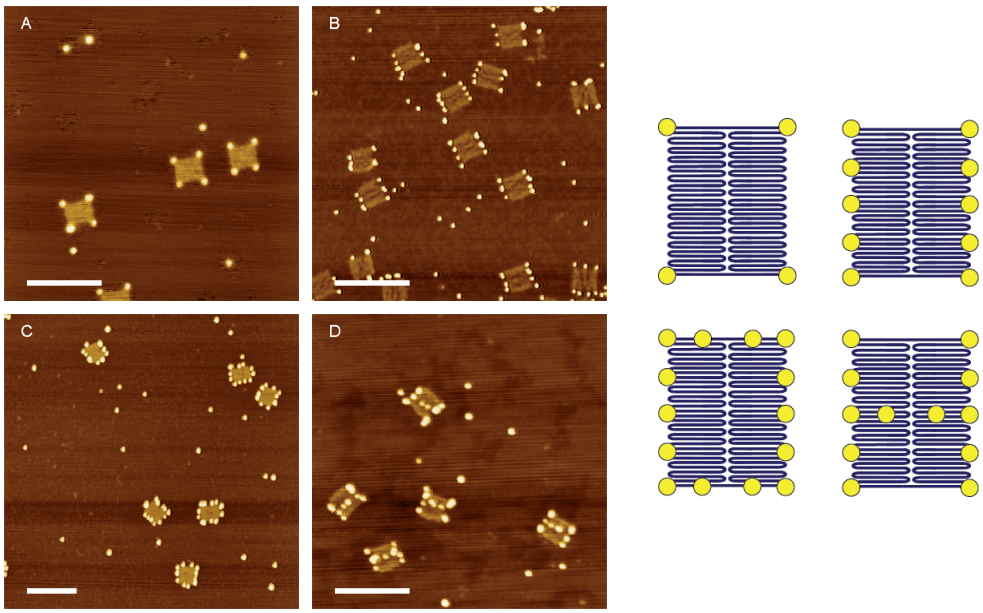

FIGURE 2.5: AFM images of different AuNP assemblies on mica: **a)** 4-corners, **b)** a pair of parallel bars, **c)** ring, and **d)** H-shape. The patterns are programmed by extending different staples with the same complementary sequence, permitting the use of the same AuNP-DNA conjugates for all assemblies. All scale bars are 250 nm. The size of the particles appears enlarged, due to convolution with the AFM tip. Schematic on the right shows the designed structures.

in 1xTAE/12.5 mM Mg^{2+} buffer (40 mM Tris-acetate, 1 mM EDTA, pH 8.2) with a single ultra-filtration centrifuge unit (100 kDa MWCO, Millipore) to remove the extra staple strands. Various groups report more thorough purification steps such as running the DNA structure through gel electrophoresis [62, 112]. We found that the buffer exchange method was sufficient to obtain a good attachment yield. The 5 nm gold nanoparticles (AuNPs) to be attached to the DNA templates were conjugated to a specific oligonucleotide chain ($X_{24,comp}$) at a AuNP:DNA ratio of 1:5 and left to incubate overnight, following the recipe of Refs. [69, 140] and described in detail in Chp. 3. The DNA strands used for conjugation were synthetic oligos purchased from IDT (Integrated DNA Technologies, Inc). They had a disulfide modification (lipoic acid) on the 5' end followed by a 5 base spacer (T_5) and the complementary sequence

to that of the binding sites ($X_{24,comp}$). The AuNP-DNA conjugates were then backfilled with thiolated T_5 sequences (IDT) to prevent aggregation of AuNPs that would otherwise occur in the presence of 50 mM Mg^{2+} concentration buffers; this incubation lasted 24 hours at room temperature to ensure maximal coverage. The typical backfilling ratio was 60:1 (T_5:AuNP). Unconjugated DNA strands were then removed from the AuNP-DNA conjugate solution using gel electrophoresis (3% agarose, 10 V/cm, 15 min run, 1xTAE). The AuNP-DNA conjugates were recovered from the gel using gel extraction columns (Squeeze and Freeze, Bio-Rad Laboratories, Inc). The purpose of running the conjugates through the gel was for filtration purposes only, since 5 nm AuNPs conjugated to a 29-base sequence do not exhibit discrete bands. We surmise that without this procedure, the unconjugated X_{24} strands saturate the binding sites on the origami. In our experience, we were not able to fully remove unconjugated DNA strands using an ultrafiltration centrifuge, contrary to DNA origami buffer exchange purification [43].

We next placed the DNA templates on substrates. Mica (Ted Pella) and Si/SiO2 (Silicon Quest, both native and 1 μm thick oxide) substrates were used in our experiments. Freshly-cleaved mica was used for AFM imaging of both origami formation and gold binding (Fig. 2.5). For mica, the origami buffer was kept at 1xTAE/12.5 mM Mg^{2+} . Silicon was used for samples that were later metallized and for SEM imaging of the resulting structures (Fig. 2.7). Silicon substrates were cleaned by the standard RCA I and II steps, followed by oxygen plasma ashing for 5 min at 100 W using an SPI Plasma Prep II. The origami solution was adjusted to 1xTAE/100 mM Mg^{2+} . The high Mg^{2+} concentration is used to promote attachment between the negatively charged DNA template and the negatively charged silicon dioxide substrate [54]. TAE serves as a chelator of divalent cations such as Mg^{2+}. Since many enzymes need ions as co-factors, TAE helps against contaminant enzymatic degradation. For this reason our current protocols have been adjusted to keep the 1xTAE:12.5 mM Mg^{2+}

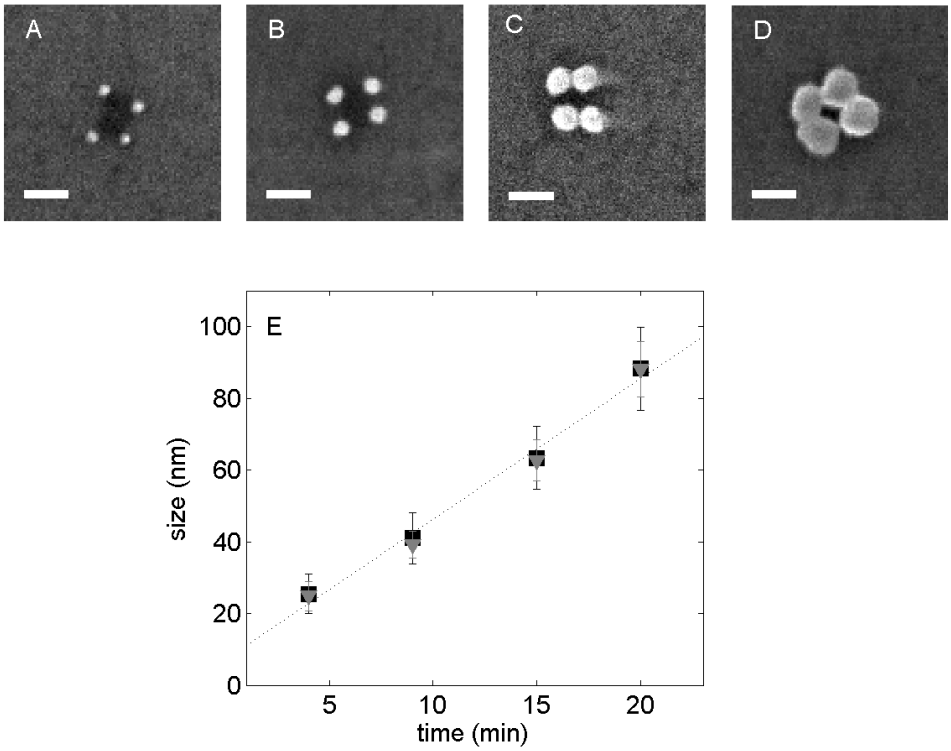

FIGURE 2.6: Controlled growth due to silver reduction of 5 nm AuNPs bound to the four corners of the rectangle origami. Metallization times: **a)** 4, **b)** 9, **c)** 15, and **d)** 20 min. All scale-bars are 100 nm e) Average particle dimensions in horizontal (squares) and vertical (triangles) directions for different metallization times, as measured from SEM images.

concentration ratio when using high Mg^{2+} ions buffers (i..e 10xTAE/125mM Mg^{2+}). The 5 nm AuNPs attachment was performed after deposition of the DNA templates on the substrate. I will refer to this technique as surface-attachment, contrary to in-solution attachment. On both types of substrates, the origami (0.5 nM, 5 μL) was deposited onto the surface and left for 5 min to adsorb. A solution containing functionalized AuNPs (15-100 nM) was then added and left to incubate at room temperature for an additional 30 minutes. The sample was then washed by immersing the substrate in deionized water (18 $M\Omega$) for 10 sec. to remove excess unconjugated AuNPs and dried gently under a stream of nitrogen. Unlike Ref. [43], in our case it was not necessary to anneal the samples at elevated temperature or to incubate

them for longer periods of time in order to obtain good binding. This is attributed to AuNPs of 5 nm having faster diffusion than particles of bigger size, so they are able to find their binding site in a short time scale (few minutes) and without been sunk onto the substrate. We programmed different AuNP binding sites by extending different subsets of staples from the original "tall origami" staple set. The extension sequence was X_{24}, which allowed us to use the same 5 nm AuNPs functionalized with $X_{24,comp}$ for all assemblies. The resulting assemblies are shown in Figure 2.5. We found that functionalized particles avoid attachment if the adjacent binding sites are closer than 20 nm apart (center-to-center), as expected for DNA-functionalized particles with negative surface charge (see discussion in Ref. [117]). We found that when functionalized AuNPs are stored for a few weeks in their gel-recovered buffer (i.e. TAE) they repel each other less (attach in closer proximity). This suggests that the phosphine coating is partially detached. This could be avoided (or purposely implemented) by further phosphinating the storing buffer upon gel recovery. Sample imaging was performed using dry AFM in tapping mode (Nanoscope IIIa with a Multimode head and NT-MDT NSG30 tips from Nanoscience Instruments, Inc). This lets us reuse AFM tips while still obtaining good image resolution of the DNA origami and AuNPs. We enlarged the AuNPs bound to origami templates by reducing silver ions from solution (Fig. 2.6). The AuNP assemblies adsorbed on silicon substrates were metallized by applying a commercially available microscopic staining kit (HQ-Silver, Nanoprobes, Inc), which we used previously for fabrication of silver nanowires [90]. The metallization procedure was performed at room temperature inside a red-light illuminated dark room. Equal volumes of the three kit components (initiator, moderator, and activator) were mixed. Conveniently, the reaction proceeded at a slow rate that allowed us to easily control the amount of deposited metal by varying the metallization time. The metallization process was halted by a brief immersion and rinsing of the samples in DI water. The SEM images in Figure 2.6,

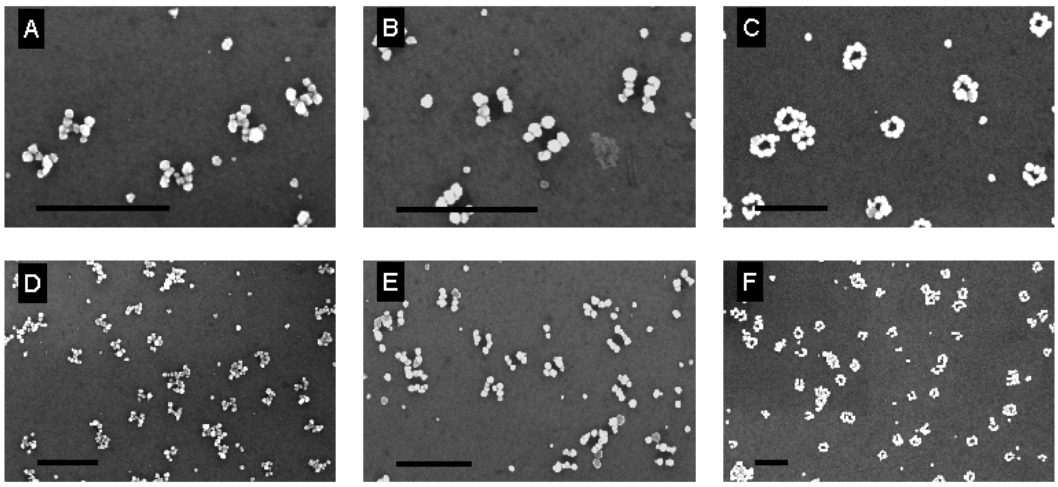

FIGURE 2.7: SEM images of different metallic nanostructures: **a)** and **d)** H-shapes, **b)** and **e)** pairs of parallel bars, **c)** and **f)** rings. All scale bars are 500 nm.

panels A-D show the growth of NPs bound to the four corners of the origami template and metallized for different times. The measured size of the NPs as a function of metallization time is plotted in Figure 2.6 E.

Figure 2.7 shows the successful fabrication of metallic structures based on the seed particle assemblies of Figures 2.5 B-D, resulting in rings, pairs of parallel bars, and H-shapes. In these structures, the metallization times are long enough, and the seed particles are placed close enough, to fuse the particles together. Although not all of the binding sites were occupied by AuNPs, as shown in Figure 2.5, the programmed structures such as H-shapes or rings were still formed, as clearly shown in Figure 2.7. Typically, the center-to-center distance between the seed AuNPs was 20 nm, and the metallization times were 10 min. The metallic lines formed from four seed particles along the origami side had to be roughly 50 nm thick in order to appear contiguous in SEM images (Fig. 2.7 B). The narrowest metallic line width is ultimately limited by the distance between neighboring AuNP seeds and the variation in particle size after metallization.The feature sizes might be reduced

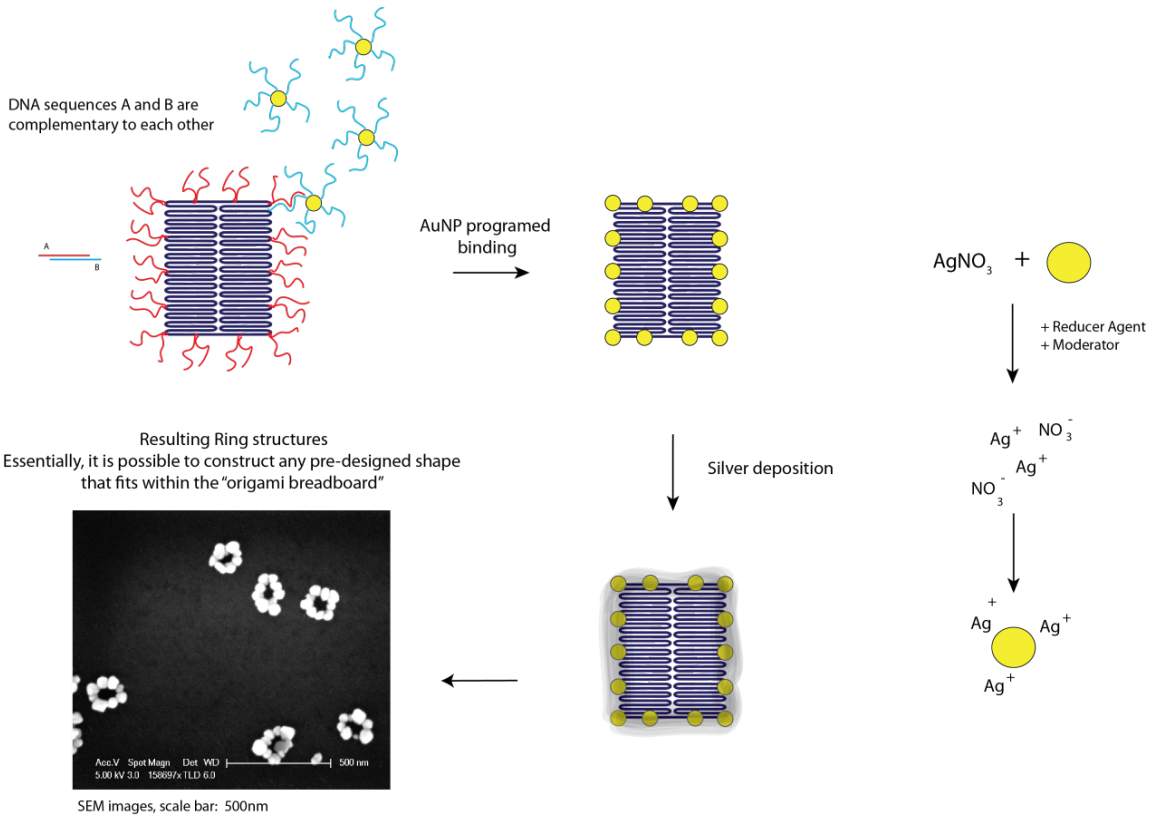

FIGURE 2.8: Schematics of the full assembly process: Attachment of AuNPs, followed by their enlargement using silver ion deposition. NPs are fused after long enough incubation periods.

in the future by packing particles closer together, which would require a reduction in the effective hydrodynamic radius of the AuNP-DNA conjugates. This could be accomplished by tuning the amount of positive counterions in the buffer, using smaller AuNP-DNA conjugates, or decharging the particles by partially removing the excess phosphine as previously discussed. Smaller interparticle distance would reduce the metallization time required to fuse the particles, which would ultimately decrease the width of the resulting metallic structures. In addition, proof of structural continuity is necessary. This could be demonstrated using electrical measurements. However, placing contacts on these samples is challenging due to their size.

2.4 Conclusions

Through this chapter, we have shown the great capabilities of DNA to be used as a structural-formation tool. We demonstrated that complex metallic nanostructures can be assembled programmatically using DNA templates, DNA functionalization of seed nanoparticles, and metallization via silver-reduction chemistry. While the amount of successfully assembled structures (Fig. 2.7) appears encouraging, there are many parameters one could still optimize to increase the overall yield even further, among them the design of the binding sites on the DNA origami; the concentrations of the DNA origami and the AuNP-DNA conjugates; the parameters that control the surface attachment; and the metallization protocol. The presented programmable templates should enable the fabrication of a wide range of components for nanoelectronic and plasmonic applications. For example, I will describe on Chp. 5 how the fabricated templates can be used to fabricate SERS substrates.

Chapter 3

Functionalization of Nanocomponents

This chapter discusses the various schemes used to functionalize nanocomponents. The main focus will be on the functionalization of AuNPs with ssDNA strands. General principles about conjugation applicable to other nanocomponents are discussed, including their stability in the context of DNA nanotechnology.

3.1 Fundamentals of Functionalization

Due to their quantum nature, nanocomponents such as fluorophores, semiconductor quantum dots, and metallic nanoparticles exhibit unique properties not usually encountered in bulk materials. A wide range of applications are encountered in virtually any area of science including electronics, optics, biosensors, and medicine. Not only do nanocomponents have intrinsic individual properties, but these properties change due to interaction among themselves. It is therefore desirable to control their placement and functionality. As we have seen in Chapter 2, DNA base complementarity offers a route to self assemble nanocomponents with well defined inter-particle arrangements.

It is useful to abstract some basic principles associated with conjugation and functionalization. Conjugation is the process of attaching two components together.

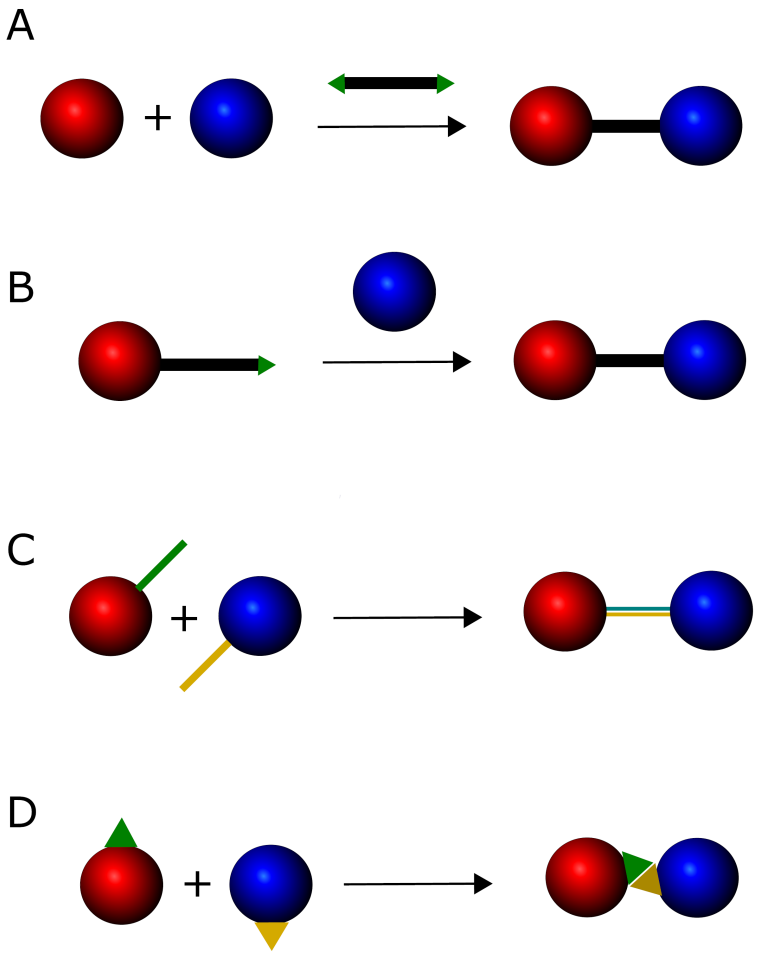

FIGURE 3.1: Conjugation schemes for crosslinking: a)Two functional groups extended by a ligand b) Component has a ligand with a functional group c) Two complementary ligands d) Components with complementary functional groups.

As shown in Figure 3.1, the conjugation process requires two components and a crosslinker. There is a variety of molecular and supremolecular crosslinkers that can be used depending on the desired application. Examples of molecular crosslinkers are thiol, amines, aldehydes and carboxylates, and supramolecular croslinkers include streptaividin-biotin, protein-protein, and DNA-DNA. Zero-length crosslinkers are molecules that form linkage without spacing from additional atoms. Extensions of crosslinkers can be achieved using molecular spacers (e.g. ligands). Functional components posses crosslinkers yet to be attached to another components. Function-

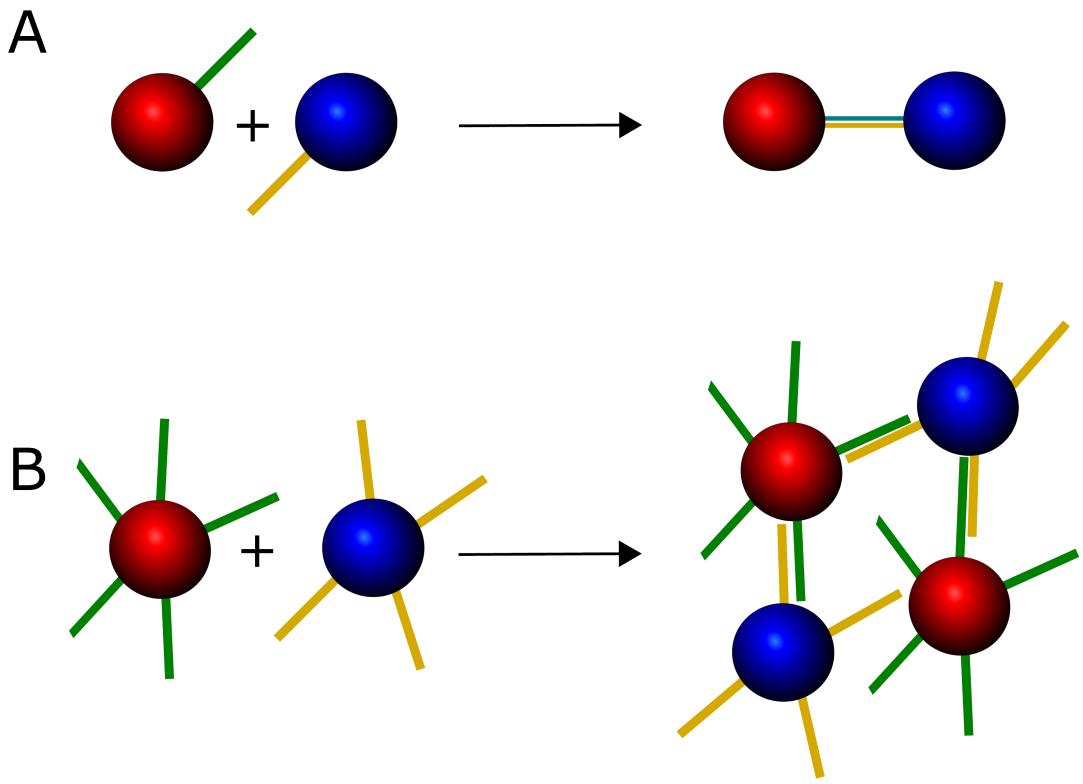

FIGURE 3.2: Depending on the assembly scheme, controlled functionalization of components might be required **a)** Two complementary species of monofunctionalized AuNPs form dimers, while **b)** polyfunctionalized species form aggregates.

alization is the process of conjugating potential crosslinkers to a given component. Here, we focus on the attachment of DNA strands to gold nanoparticles.

For certain assembly schemes, the number of functionalized groups attached become important. For example, in order to assemble AuNPs dimers in solution, one requires two complementary monofunctionalized species (blue or red, figure 3.1). If the particles were instead polyfunctionalized, aggregates would form. By careful control of DNA strands on AuNPs, Alivisatos et al. have beautifully demonstrated the rational assembly of polycomponents in solution [75]. Assembly of more complex structures by the sole use of individual DNA strands is not only a difficult task, but it also lacks structural rigidity. DNA origami provides a stiffer support to assemble nanocomponents, as has been vastly demonstrated. Please refer to Ref. [67] for a

comprehensive review.

3.2 Gold Nanoparticles Functionalization

Gold-DNA functionalization was simultaneously demonstrated by Alivisatos [4] and Mirkin's [79] groups. Both approaches used sulfide crosslinkers to covalently attached DNA strands to AuNPs. DNA's negatively charged backbone is repelled by the negatively citrate-capped AuNPs and by other DNA strands, preventing the formation of a close packing structure. Mirkin's approach consists of the slow addition of sodium chloride (NaCl). The key idea is that if much NaCl is added too quickly, the metallic particles will irreversibly aggregate before DNA has a chance to attach to them. As the size of the particle increases, they are more susceptible to aggregation, and thus the NaCl aliquots must be smaller. Alivisatos took a different approach in which first the AuNPs were stabilized through a phosphination process (e.g. BSPP), and then DNA and NaCl were added, in a single step. I found that the phosphination approach works well for particles up to (15 nm), while for larger particles the slow salt addition is easier to implement (BSPP itself is charged enough to cause aggregation on bigger particles). AuNPs usually come in concentrations below what is desired for most applications. The necessary concentration can be achieved by forming a small pellet of AuNPs through centrifugation, followed by removing the supernatant. The pellet is then reconstituted in the desired volume to achieve a given concentration. In the case of particles below 15 nm, centrifugation by itself is not enough to form a pellet. One can cause a temporary aggregation by adding a small amount of NaCl to previously stabilized AuNPs (phosphinated, or already DNA capped). The removal of the first supernatant eliminates most of the NaCl excess, but leaves enough trace to cause partial aggregates. Unfortunately, this trace amount is not enough to form a pellet by centrifugation unless methanol is added.

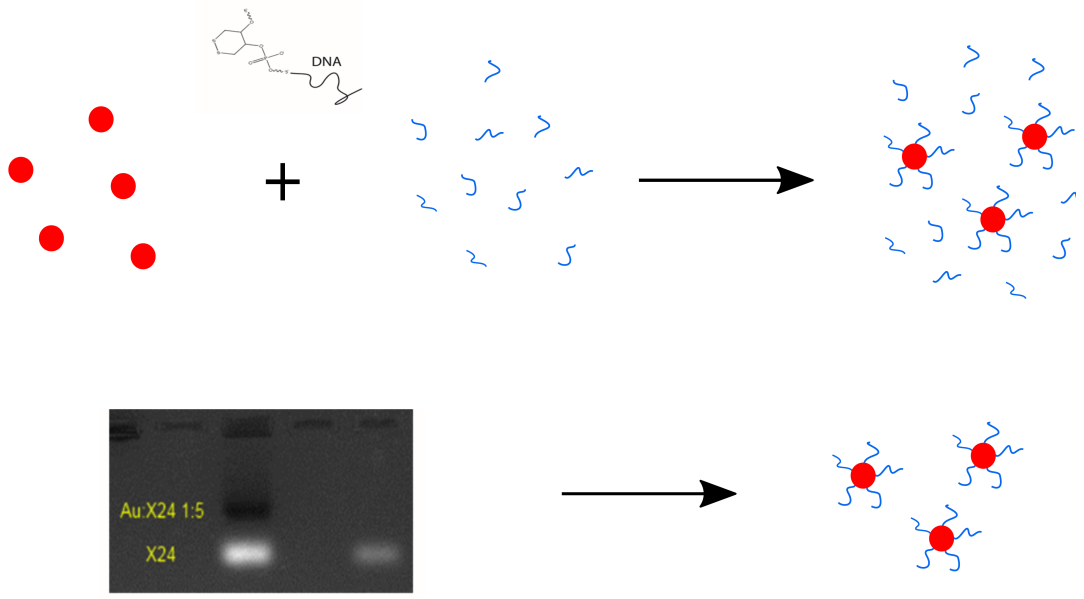

FIGURE 3.3: Functionalization of nanocomponents. First, the AuNPs are functionalized with a DNA via a disulfide crosslinker. Then, the particles are gel purified using gel electrophoresis. The removal of unconjugated DNA excess is an imperative step to prevent them from later on hindering the binding sites.

An alternative to both methods described (phosphination and salt addition) has been recently demonstrated. It takes advantage of the fact that the A and C bases become partially positively charged under low pH conditions (pH 3), avoiding the charge repulsion between themselves as well as the negatively charged citrate capping. This novel method decreases the conjugation time (and efficiency) of the DNA-AuNPs functionalization to just a few minutes [142, 143, 144]. It must be noted that for large particles (e.g. 60 nm), the pH itself does not provide close enough packing to make the AuNPs resistant under highly ionic buffer conditions, and one must resort to hybrid methods. This is discussed in more detail in the next section.

Lastly, let's mention an alternative to thiol as a crosslinker: Carboxylate-amine conjugation. A carboxylic acid group reacts with an amine to produce an amide bond. Carbodiimide serves as a necessary activation agent which, together with a carboxylic acid, produces an unstable highly reactive O-acylsourea intermediate. The

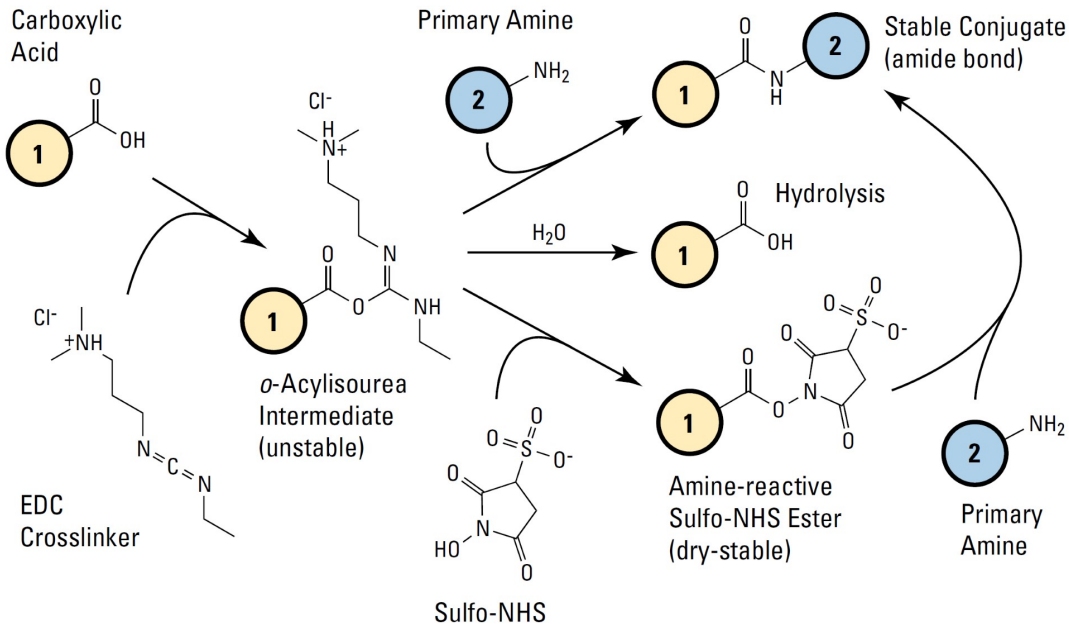

FIGURE 3.4: Mechanism pathways for carboxyl-amine carbodiimide reaction. The carboxylic group reacts with EDC to form an unstable Acylisourea intermediate state, which can react directly with an amine, or hydrolize back. The reaction can be catalyzed by incorporation of a third pathway via Na sulf-NHS state.

carbodiimide EDC is water soluble and can be used with most buffers. Additionally, one could add NHS to catalyze the reaction. Figure 3.2 shows the mechanism of the reaction. A detailed protocol is described in Appendix D.1.1.

As discussed in Chapter 2.1, it is imperative to remove the unconjugated DNA strands before performing the desired conjugation, else they will compete with the nanocomponent for the target strand. They can be completely removed by running the conjugated structures through agarose gel (Figure 3.3). One does not need to resort to additional labeling (i.e. ethidium bromide) since the AuNP-conjugate band is visibly red. Figure 3.2 A shows how the gel can be used to separate AuNPs functionalized with different numbers of conjugated strands. This is possible as long as the length of the strand is sufficient (70 bases) to separate the bands. Figure 3.2 B shows AuNPs conjugated at different AuNPs:DNA ratios. Structures are recovered

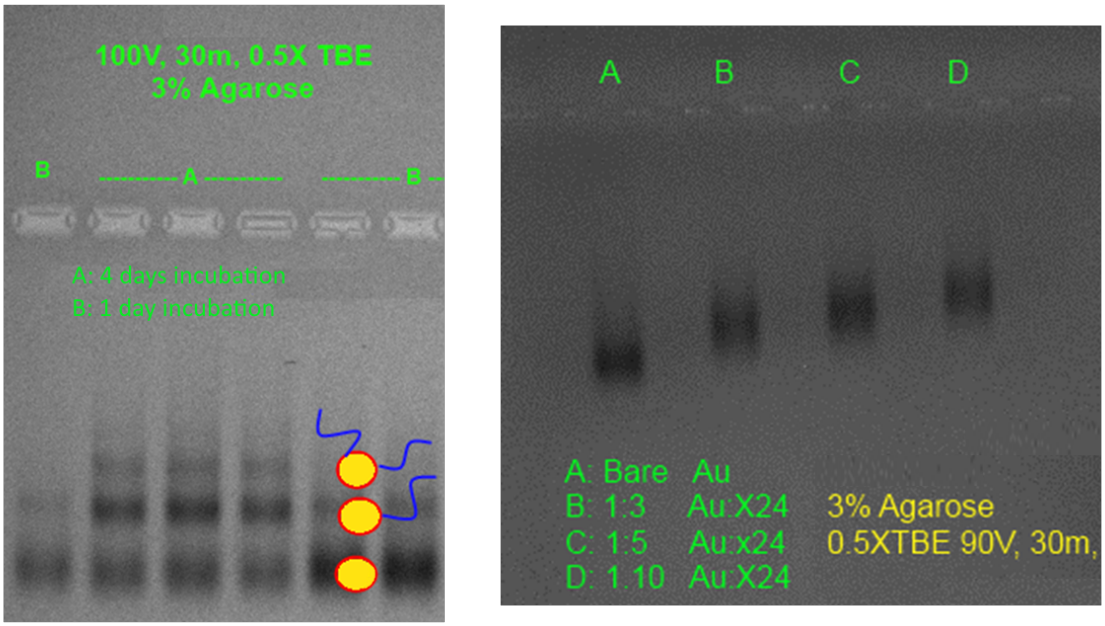

FIGURE 3.5: **a)** Gel can be used to separate AuNPs with discrete number of conjugated strands (70 bases). **b)** shows AuNPs conjugated with 24 bases DNA at different AuNPs:DNA ratios.

from the gel by cutting the band of interest, finely chopping it and centrifuging it using a filter. The buffer with the resulting particles is the same as the one used to form the agarose gel.

3.3 Nanocomponents Stability and DNA Origami

As discussed in Chapter 2, one scheme used to attach nanocomponents onto DNA templates is through DNA self-complementarity. The stability of DNA origami at room temperature requires the use of highly ionic buffers. The typical buffer used during DNA origami formation is composed of 40 mM Tris, 20 mM acetic acid, 1 mM EDTA, and 12.5 mM Mg^{2+} (1xTAE/Mg^{2+}). The amount of ions present in the solution is increased if DNA origami is placed on substrates. DNA origami attachment to silicon dioxide or glass requires Mg^{2+} concentration on the order of (~100 mM). Therefore, functionalized nanocomponents must be stable enough to

stand 10xTAE/Mg . As the size of the metallic particle increases, they become less stable under ionic environments, and their passivation becomes even more relevant. Stabilization schemes include the use of surfactants, maximizing DNA loading, or charging them (i.e. phosphination). Each of the DNA-AuNPs conjugation methods described previously provide different insights into parameters that can be varied to stabilize the AuNPs. Hurst et al. [45] elegantly played with the parameters associated with AuNP-DNA conjugation, and identified what is required to maximize the DNA loading. Salt aging decreases DNA repulsion, maximizing loading when added up to 0.7 M NaCl. Monothiol crosslinkers pack more DNA than bulkier dithiol crosslinkers. PEG neutral spacers pack tighter than DNA negatively charged spacers. Shorter oligos pack tighter than larger oligos providing additional energy increases packing (i.e. 10 sec sonication or heating). These principles combined with the previously described methods provided our own hybrid recipe for AuNPs functionalization. The most stable particles are achieved when a discrete amount of the functional DNA strand is conjugated (usually 20 bases) followed by a "backfilling" of shorter oligos (i.e. TTTTT or T5). Further stability (but not substantial) can be obtained by adding a small PEG molecule(thiolPEG5).[1] PEGs are molecules with no charge, small enough to fit into any remaining open surface. We have found that the following hybrid recipe to provide thus far be the most efficient and fastest way of conjugating spherical AuNPs of sizes ranging from 5 nm - 60 nm.

1. Addition of SDS surfactant (0.02%)
2. Bringing pH down to 3 (via sodium citrate buffer).
3. Addition of functional thiolated DNA (e.g. X_{24}, reduced or not - 5 strands for 5 nm and 20-50 strands for 60 nm)
4. Addition of thiolated DNA backfiller (shorter T_5, reduced or not) in 100 times

[1] polyethylene glycol

FIGURE 3.6: Test of conjugated 50 nm AuNPs stability under 5xTAE/Mg^{2+} . Red vial shows the low pH method with the slow addition of NaCl. The low pH method only (no NaCl addition) was used for the blue vial.

excess the maximum reported loading capacity (Max. load amount obtain from [45]).

5. Addition of NaCl aliquots while testing their stability under 10xTAE/Mg^{2+} buffer

The ideas behind this recipe can be extended to the functionalization of other nanocomponents. As an example, Figure 3.3 shows 50 nm AuNPs conjugated using our hybrid conjugation method under 10x TAE/Mg^{2+} conditions (red vial suspended particles), while the blue vial (aggregates) was obtained using the low pH conjugation method only. The thiol was not activated in either case.

One rapid way to test if the conjugated AuNPs are stable enough to be used with DNA origami is to place them under the same buffer conditions (i.e. 1x - 10x TAE/Mg^{2+}) and to observe if there is a color change. It is worth noting that although all the mentioned AuNPs recipes suggest the necessity of "activating" the

thiol crosslinker through TCEP or other agent. Sulfide-modified DNA (mono- and di-thiol) usually comes in protected forms We have found that it is not necessary to activate them (i.e. using TCEP) since gold itself is able to cleave S-S bonds. The rate of attachment is certainly lower for non-activated sulfides, which could be a drawback if a tight packing is required (i.e. for larger metallic particles)

3.4 Conclusions

Through this chapter, we have described the principles of nanocomponent functionalization. Specifically, we looked at four methods of functionalizing AuNPs with ssDNA: i) Phosphination (Alivisatos), ii) salt-aging (Mirkin), iii) low pH (Liu), and iv) a carboxyl-amine via carbodiimide reaction. We discussed ways to increase the loading on AuNPs, necessary to have a stable nanocomponent under high ionic solutions and described our hybrid conjugation method used to conjugate spherical AuNPs ranging from 5 nm to 60 nm.

Chapter 4

Plasmonics

In this chapter I will introduce three classical analytical approaches used to describe localized surface plasmons: the Quasi-Static Approximation (QSA), the Mie solutions approach, and the plasmon-hybridization fluid model. I will focus on discussing the parameters that affect the plasmon resonance frequencies and the electromagnetic field spatial distribution. The discussion will serve as a preamble to understanding the origins of the "hot spots" associated with SERS (Chp. 5).

4.1 Fundamentals of Plasmonics

Plasmons are the quantized collective oscillation of electrons, just as phonons are the collective oscillations of the atomic lattice. They are better supported by metals where the electrons are free to oscillate. Plasmons can be excited with incident electromagnetic waves [71] , and their resonance frequency is dependent on several parameters such as the geometry, composition, size, and interparticle arrangement. For structures with size and inter-particle gaps down to the nanometer scale, plasmons can be described using classical electrodynamics, and their behavior is determined by Maxwell's equations. Structures that do not follow classical behavior (sub-nanometer scale) must take into account electron quantum tunneling as well as permittivity variations close to the metallic interface [74]. This thesis will restrict

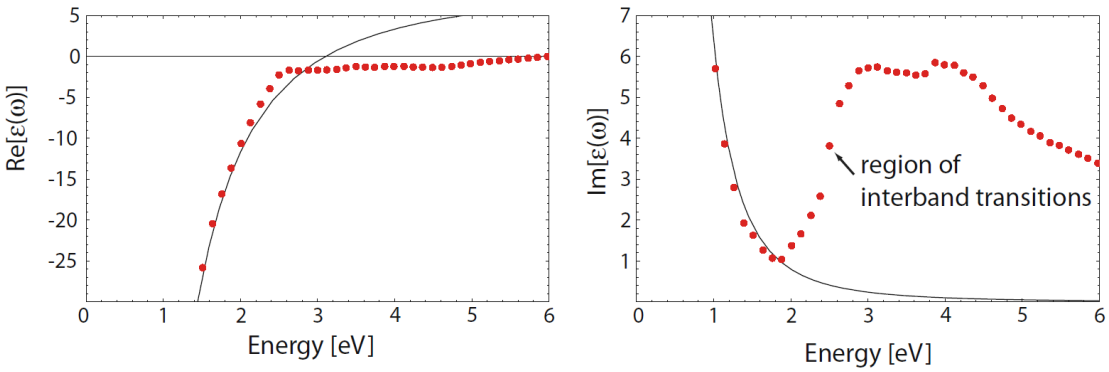

FIGURE 4.1: Real and imaginary experimental permittivity values for gold (red dots). Solid line is the free electron model. Above excitation frequency 2 eV the model fails due to interband electron transitions. Silver permittivity values are shown in Appendix B.1. Figure adapted from Ref. [71].

the discussion to structures with particle radius R and gap distances D large enough to be described classically.

Plasmons can be classified based on their propagation or confinement. Electron located at the interface of two materials with different dielectrics can couple to electromagnetic fields, and are referred to as Surface Plasmon Polaritons (SPPs). They can be thought of as ripples or waves moving through the surface of a sea of electrons (surface charge density waves). SPPs can propagate through continuous waveguides with sizes far below the electromagnetic diffraction limit [124]. Localized Surface Plasmons (LSPs) on the other hand are spatially confined due to the size of the structure such as in metallic nanoparticles. Individual and coupled LSPs will be the focus of our discussion and we refer the reader to Refs. [10, 98] for a complete review on SPPs. Note that it is possible to propagate plasmons through chains of closely spaced nanoparticles just as through a chain of coupled harmonic oscillators [72, 120]. Before discussing the plasmon models, let's look at the frequency dependence of a given material. For that, consider the Drude-Sommerfeld model (or plasma model). Electrons are treated as a free gas that moves against a fixed positive ion

background. We can write the force equation as,

$$m\ddot{x} + m\gamma\dot{x} = -eE(t) \tag{4.1}$$

with solution,

$$x(t) = \frac{e}{m(\omega^2) + i\gamma\omega}E(t) \tag{4.2}$$

where the m is the effective mass, and a dissipation damping factor. By relating the electric field to the polarization, $P = -nex = \epsilon_o(\epsilon_r - 1)E$, we obtain the frequency dependent permittivity,

$$\begin{aligned}\epsilon(\omega) &= \epsilon_\infty - \frac{\omega_p^2}{\omega^2 + i\gamma\omega} \\ &= \epsilon_\infty - \frac{\omega_p^2}{\omega^2 + \gamma^2} + i\frac{\omega_p^2}{\omega^2 + \frac{\omega^2}{\gamma^2}}\end{aligned} \tag{4.3}$$

where $\omega_p^2 = ne^2/(\epsilon_o m^*)$ denotes the bulk plasma frequency. The ϵ_∞ term was incorporated to account for the positive nuclei background. The instrinsic response of a scatterer to an external field is then encoded in the permittivity $\epsilon(\omega)$ of the material. If one neglects the damping term γ, the permittivity $\epsilon(\omega)$ reduces to $\epsilon(\omega) = 1 - \epsilon_p^2/\epsilon^2$. We can identify two distinct regions: i) when $\omega > \omega_p$ the index of refraction n is real, and light is transmitted (i.e. the electrons respond slowly and the material becomes transparent); and ii) when $\omega < \omega_p$, n is imaginary, light is fully reflected (i.e. the electrons respond quickly, screening the incident light); Figure 4.1 shows the experimental values of gold permittivity along with a plot of the Drude model (Eq. 4.3). It can be readily seen that the model fails at frequencies above the interband electron transitions ($\omega > 2\ eV, \lambda < 620\ nm$). To account for these transitions, an additional Lorentz-oscillator term can be incorporated in the form [71],

$$L = \frac{A_i}{\omega_i - \omega^2 - i\gamma_i\omega} \tag{4.4}$$

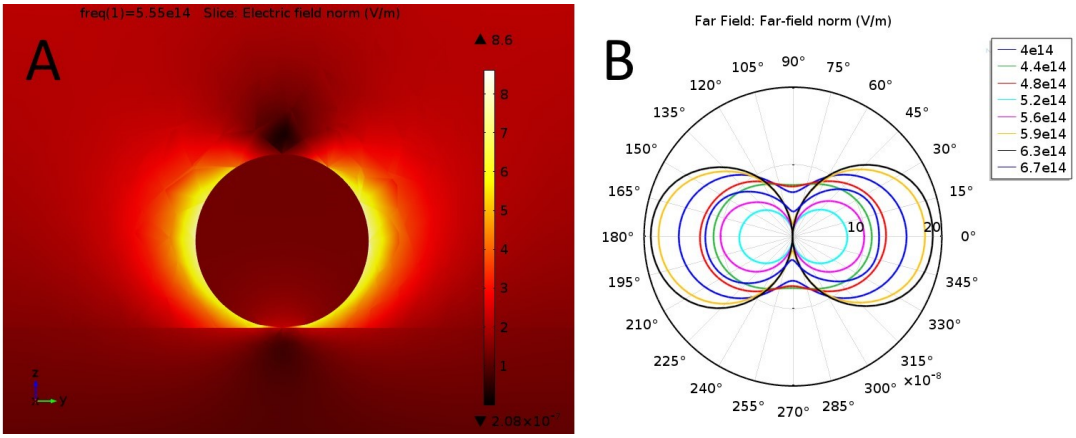

FIGURE 4.2: **a)** Spatial distribution and **b)** far field radiation pattern of a single 40 nm AuNP sitting on top of a silicon substrate. Incident radiation wavelength is 545 nm with y-axes polarization. Simulations using COMSOL Multiphysics [18].

4.2 Single Spherical Scatterers

4.2.1 Quasistatic Approximation

Let us first consider nanoparticles with dimensions much smaller than the excitation wavelength, $R \ll$. Under this condition, the phase of the field can be considered to be uniform throughout the metallic structure. One can then solve for the resonance behavior and field distribution without considering the oscillatory behavior of the driving field, and incorporate it later to the final solution. This gives the reason for its name, the quasi-static approximation. The field distribution of a spherical geometry immersed in a constant electric field is obtained by solving the Laplace equation $\nabla^2\Phi = 0$ with appropriate boundary conditions to obtain (Appendix A.1.1),

$$\begin{aligned} E_{in} &= \frac{3\epsilon_d}{\epsilon(\omega) + 2\epsilon_d} E_o \hat{\mathbf{z}} \\ E_{out} &= \frac{\epsilon(\omega) - \epsilon_d}{\epsilon(\omega) + 2\epsilon_d} E_o \left(2\, cos(\theta)\hat{\mathbf{r}} + sin(\theta)\hat{\theta}\right) \end{aligned} \tag{4.5}$$

with the dipole moment,

$$p = 4\pi\epsilon_o\epsilon_d\ a^3\ \frac{\epsilon(\omega)-\epsilon_d}{\epsilon(\omega)+2\epsilon_d}E_o = \epsilon_d\alpha E_o \tag{4.6}$$

Here, $\alpha = 4\pi\epsilon_o\ a^3\ \frac{\epsilon(\omega)-\epsilon_d}{\epsilon(\omega)+2\epsilon_d}$ is the polarizability factor. It is clear that the resonant enhancement of the field is a consequence of the resonance from the polarizability of the scatterer, and of the $\epsilon(\omega)$ frequency dependence. For spherical particles, resonance is obtained when $\epsilon(\omega) = -2\epsilon_d$ (a.k.a. Fröhlich condition). Specifically, for a Drude metallic sphere in vacuum the resonance occurs at $\omega = \omega_p/\sqrt{3}$. Looking at the permittivity of Au (Figure 4.1), one can see that as the permittivity ϵ_d of the medium embedding the NP is increased, the ϵ of the metal needed to obtain resonance also has to increase, producing a resonance red-shift.

It is easy to see that Equation 4.5 resembles a dipole immersed in an constant electric field. This provides two interesting insights: i) the incident field is spatially redistributed providing regions of enhanced field; ii) the plasmon excitation is confined in sub-wavelength regions. The former is of special interest for spectroscopy purposes, as will be further discussed in Chapter 5. To incorporate the time dependence $e^{-i\omega t}$ it is then possible to express the scattering fields off a spherical scatterer as the ones produced by an oscillating dipole. The corresponding scattering σ_{sca} and absorption σ_{abs} cross sections are given by (Appendix A.8),

$$\begin{aligned} \sigma_{sca} &= \frac{k^4}{6\pi}\alpha^2 \propto \frac{a^6}{\lambda^4} \\ \sigma_{abs} &= k\ Im(\alpha) \propto \frac{a^3}{\lambda} \end{aligned} \tag{4.7}$$

where $k = \omega/c$ is the wave vector. The extinction coefficient is defined as $\sigma_{ext} = \sigma_{scat}\sigma_{abs}$. Notice that both, scattering and absorption, are also in resonance when the scatterer is excited at the plasmon resonance frequency. For particles much smaller than the incident field ($R \ll$), the absorption is much larger than the scattering cross

section. Figure 4.2 shows the spatial distribution of the normalized field scattered from a 40 nm AuNP on top of a glass substrate. The dipole behavior is clear from the farfield radiation pattern. While the quasi-static approximation is able to describe the spatial distribution of the electric field induced by the dipole mode, no higher order modes are predicted (i.e. quadrupole). Additionally, it fails to predict the resonance dependence on the particle's size. As can be seen from Figure 4.3, the size dependence becomes significant for particles greater than 50 nm.

Before discussing the full analytical solution through the Mie approach, let's discuss the plasmons damping mechanisms. Plasmons decay through radiative (dipole radiation) and non-radiative channels [27]. Elastic collisions of electrons (ohmic loss) are the main non-radiative damping mechanism and result in plasmon dephasing. The next major non-radiative decay channel is Landau damping, responsible for generating electron-hole pairs via inter-band or intra-band transitions. Thermalization continues through electron-phonon coupling. The lifetime τ of a plasmon is inversely proportional to the width of the resonance Γ. The collision processes are responsible for broadening the plasmon resonance as the particles increase in size.

4.2.2 Mie Solutions Approach

If we consider scatteres smaller but not much smaller than the driving wavelength Rl ($\sim$ 100 nm), the quasi-static approximation is no longer valid and a more rigorous approach is needed [78]. A plane wave incident to a spherical scatterer must satisfy the wave equation $\nabla^2 E + k^2 E = 0$, be divergence free ($\nabla \cdot E = 0$), and comply with the appropriate boundary conditions. Since the problem involves spherical symmetry, it gets greatly simplified by expressing the fields in spherical coordinates, as an infinite series expansion of wave harmonics. This approach is known as the Mie Solution. As we will see, the Mie approach is an exact analytical solution for spherical scatterers. It is able to predict the multipolar nature of scattering by a sphere as well

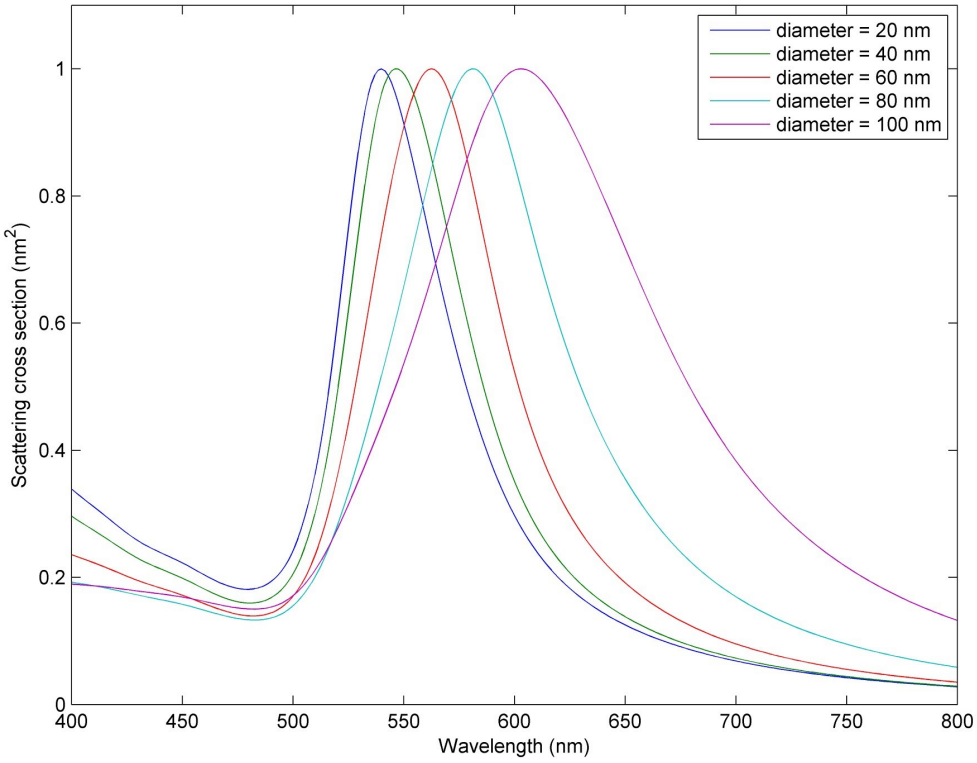

FIGURE 4.3: Normalized cross scattering of AuNPs of various sizes. As the particle size increases the resonance is red-shifted and the peak broadens. Numerical simulations using BEM.

as retardation effects. A scalar wave can be decomposed into orthogonal functions (a.k.a. partial wave expansion) and is given by [48, 46],

$$\begin{aligned} \psi_k(r) &= e^{ikrcos\theta} \\ &= \sum_{l=0}^{\infty}(2l+1)i^l \; j_l(kr)P_l(cos\theta) \end{aligned} \tag{4.8}$$

The incident plane wave can be written as,

$$E = E_1 \; e^{i(k\cdot r-\omega t)} \tag{4.9}$$

The solutions of a plane wave scattering from a perfectly spherical scatterer are determined by enforcing the boundary conditions between the inside and the outside

fields. It is convenient to break the field into perpendicular and parallel components with respect to the scattering plane. Detailed procedure on obtaining Mie solutions is described in Refs. [13, 48, 123] and in Appendix A.1.2. The solution is then given by,

$$E_{sca} = \frac{i}{kr} E_o[S_2 cos(\phi)\hat{\theta} + S_1 sin(\phi)\hat{\phi}] \tag{4.10}$$

S_1 and S_2 are the scattering amplitudes and are given by,

$$\begin{aligned} S_1 &= \sum_{l=1}^{\infty} \frac{2l+1}{l(l+1)} (a_l \pi_l + b_l \tau_l) \\ S_2 &= \sum_{l=1}^{\infty} \frac{2l+1}{l(l+1)} (b_l \pi_l + a_l \tau_l) \end{aligned} \tag{4.11}$$

Here, $\pi_l = \frac{P_l^1(cos\theta)}{sin(\theta)}$ and $\pi_l = \frac{\partial P_l^1(cos\theta)}{\partial \theta}$, and P_l^1 are the known Legendre polynomials. The Mie coefficients a_l and b_l determine the amplitudes of each oscillation mode, and are functions of the frequency in terms of spherical bessel functions. Each term of the expansion corresponds to a higher order term. The cross sections are given by

$$\sigma_{ext} = \frac{2\pi}{k^2} \sum_{l=1}^{\infty} (2l+1) Re(a_l + b_l) \tag{4.12}$$

As we have seen in the QSA, the resonance dependence is encoded within the polarizability. Let's look at the general form of the dipole term,

$$\alpha = \frac{4}{3}\pi a^3 \frac{1 - O(x^2) + O(x^4)}{\frac{1}{3} + \frac{\epsilon_d}{\epsilon - \epsilon_d} - i4\pi^2 \epsilon_d^{3/2} \frac{V}{\lambda_o^3} - O'(x^2) + O'(x^4)} \tag{4.13}$$

Here $O(x^n)$ are functions of the *size parameter* $x = \frac{\pi a}{\lambda}$. Several Matlab codes [76, 110] have been written, in which the user can specify the desired number of coefficients to be retained. Its interesting to note that the quasistatic approximation result is recovered when retaining only the first term within the dipole term of the Mie

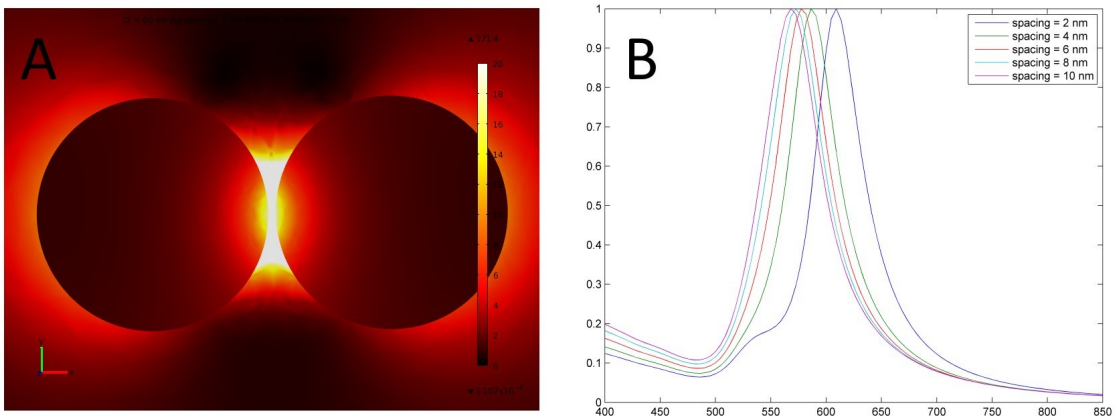

FIGURE 4.4: **a)** Electric field spatial distribution of 40 nm AuNP dimers. Incident field is polarized along the interparticle axes. **b)** Corresponding far-field spectra with gap distances ranging between 2-10 nm. The quadrupole mode starts to appear at a 2 nm gap. Simulations using COMSOL [18]) and MNPBEM [41] for a) and b), respectively.

solution (Eq. 4.5). The second term on the expansion captures the retardation effect, responsible for red-shifting the resonance as the size of the particle increases. It is given by [61, 71],

$$\begin{aligned} O(x^2) &= \frac{1}{10}(\epsilon - \epsilon_d)x^2 \\ O'(x^2) &= (\epsilon + 10\epsilon_d)x^2 \end{aligned} \tag{4.14}$$

From physical grounds, the red shift is intuitive from the fact that as the particle size increases, the distance between opposite charges also increases, lowering the restoring force and with it the location of the resonance frequency.

4.3 Multimeric Scatterers

Let's consider systems composed of more than one scatterer. In addition to the size and shape, the plasmonic coupling is determined by inter-particle separation, as well as the strength and polarization of the incident field. In a first approximation, one can depict the particle system as a set of interacting dipoles. The coupling between the particles changes the spatial distribution of the electric field and shifts

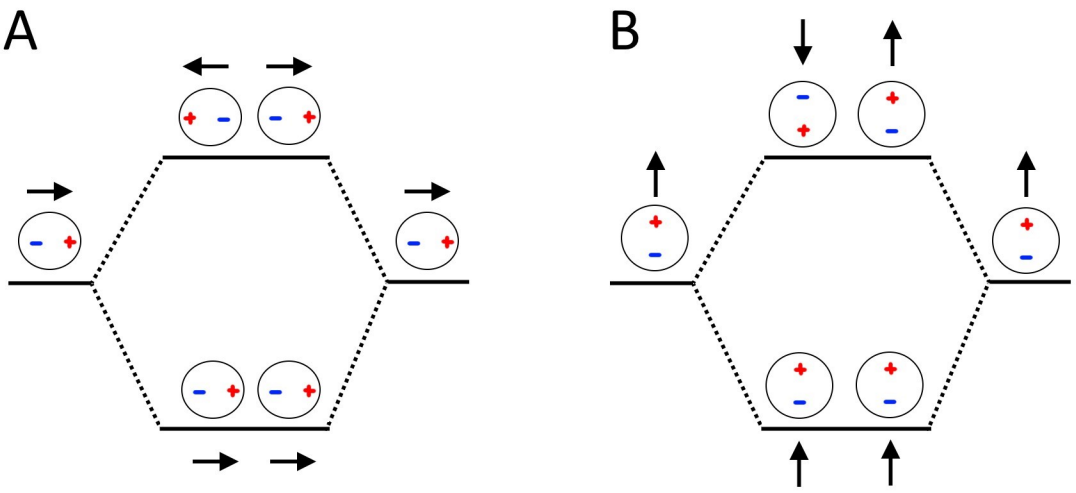

FIGURE 4.5: Plasmons hybridization is dependent on the incident polarization. Hybridized modes for **a)** parallel and **b)** perpedicular polarizations, in respect to the interparticle axes.

the plasmon resonance. Figure 4.4 shows numerical calculations of the electric field enhancement produced by 40 nm AuNPs dimers. Spatially, when the incident field is parallel to the interparticle axis and the nanoparticles are closely spaced, the field can become greatly enhanced in the interparticle gap, creating the so-called "hot spot." Notice that the far-field spectra is significantly red-shifted in comparison to individual NPs (Figure 4.3).

The resonance shift of individual modes is dependent on the polarization of the incident field. One can intuitively realize this by considering the charge distribution show on Figure 4.5: Energy is lower when opposite charges are further apart. For the case when the field is parallel to the interparticle axis, it occurs when the dipoles are aligned with each other. On the other hand, when the field is perpendicular to the interparticle axis, this occurs when the dipoles are antiparallel. The farfield spectra shows the appearance of a second mode for gaps of 2 nm. This is better explained in the context of a hybridization model.

4.3.1 Plasmon Hybridization Model

Borrowing concepts from molecular hybridization, coupling between nanoparticle modes can be predicted using point group theory. Moreover, a Lagrangian formalism can be applied to describe the interactions between individual plasmonic modes. This approach provides a physical and very intuitive sense of the interaction between plasmon modes. The coupling is expressed with a set of orthonormal modes such as the classical harmonic oscillator analog. Bonding and antibonding terms are used to describe the relative phase of oscillation between coupled plasmons (Figure 4.5. Nordlander and Prodan [84, 101, 100] introduced a plasmon hybridization model where they treated plasmons as incompressible, irrotational fluids requires that couple through electromagnetic interaction. Such fluid can be described using the continuity equation,

$$\frac{\partial \rho}{\partial t} + \nabla \cdot j = 0 \tag{4.15}$$

Here, ρ is the electron charge density with current density $j = \rho v$, where v is the electron-plasma velocity. Incompressibility requires ρ to be constant, while irrotationality that $\nabla \times j = 0$. We can define the function ϕ such that $v = \nabla \phi$ and require it to satisfy the Laplace equation, $\nabla^2 \phi = 0$. The induced surface charge density σ must obey

$$\frac{\partial \sigma}{\partial t} = n \cdot j = \rho n \cdot \nabla \phi \tag{4.16}$$

The incompressible fluid is described by the Lagrangian A.1.3,

$$\begin{aligned} \mathcal{L} &= T - V \\ &= \frac{n_o m_e}{2} \left(\sum_{l,m} \dot{N}_{l,m}^2 - \sum_{l,m} \omega_l^2 N_{l,m}^2 \right) \end{aligned} \tag{4.17}$$

and the dynamical equation,

$$\frac{d^2 N_{l,m}}{dt^2} + \omega_l^2 N_{l,m} = 0 \tag{4.18}$$

For two interacting NPs the Lagrangian is written as,

$$\begin{aligned}\mathcal{L} = \frac{n_o m_e}{2}[&\sum_{l,m}\left(\dot{N}_{1,lm}^2 + \dot{N}_{2,lm}^2\right) \\ &- \sum_{l,m}\left(\omega_l^2 N_{1,lm}^2 - \omega_l^2 N_{2,lm}^2\right) \\ &- \sum_{l_1 m_1, l_2 m_2} U_{l_1 m_1, l_2 m_2} N_{1,l_1 m_1}^2 N_{2,l_2 m_2}^2]\end{aligned} \tag{4.19}$$

where the last term is responsible for coupling the plasmons A.1.3. Using the Euler-Lagrange equations, one finds the dynamical solution of a two particle system to be,

$$\frac{d^2 N_{lm}}{dt^2} + \omega_l^2 N_{lm} + \frac{1}{2}\sum_{l_2 m_2} U_{l_1 m_1, l_2 m_2} N_{2,l_2 m_2}^2 \tag{4.20}$$

Considering the $l = 1$ mode only, the longitudinal couple dipoles predict two eigen-frequencies,

$$\omega_p^2 m = \omega_1^2 \pm \frac{|U_{1m_1,1m_2}|}{2} \tag{4.21}$$

as one would expect from the analog classical coupled harmonic oscillator. For the lowest frequency mode ω_-, the two dipoles are in phase, so this is referred to as the bonding or bright mode. The second mode corresponds to two out-of-phase dipoles, and is called the antibonding or dark mode. The transverse modes exhibit similar solutions but the higher frequency mode corresponds to in-phase oscillations, and the lower frequency mode to out of phase oscillations. The bright-dark notation was originally introduced to depict the states that are directly excited with the incident radiation. Hybridization coupling between nanoparticle dimers has been elegantly

realized by Alivisatos et al. [118], where DNA linkers were used to controllably space dimeric structures including gold-gold, gold-silver NPs. Additionally, by using NPs of different sizes, it was possible to observe dark-modes, not directly observable otherwise. Another realization of plasmons hybridization is Fano resonance, first realized by Maier's group, and expanded by Halas and Capasso groups [31, 30, 63, 127]. In a nutshell, a "bright mode" is able to couple directly to the incident radiation while a secondary "dark mode" couples indirectly through the bright mode. If the modes partially overlap, an interference between the phases is produced, creating a an asymetric line shape (with a characteristic dip on the spectra between the two modes). A comprehensive review about Fano Resonance as a universal interference phenomena is provided in Ref. [80].

4.4 Computational Methods

To conclude this chapter, let us briefly mention some computational methods used to predict the plasmonic response of radiation scattered from structures with arbitrary shapes. The plasmon resonance frequency is dependent on the geometry of the structure as shown in Figure 4.7 [81], and as one would expect, analytical solutions become rapidly cumbersome. It is now common to obtain the scattering spectra of complex geometries by resorting to computational numerical techniques such as Finite Difference Time Domain (FDTD) [18], discrete Dipole Approximation (DDA) [20, 26], and Boundary Element Method (BME) [42]. These methods are available on user-interface and command-based programs. Figure 4.3 shows scattering spectra of single metallic nanoparticles of various sizes obtained using FDTD through COMSOL (Figure refplasm3 A) and BEM through the MNPBEM Matlab toolbox [42] (Figure 4.3 B). The simulations are easy to implement and resemble experimental data well. A discussion on the advantages, drawbacks, and parameters

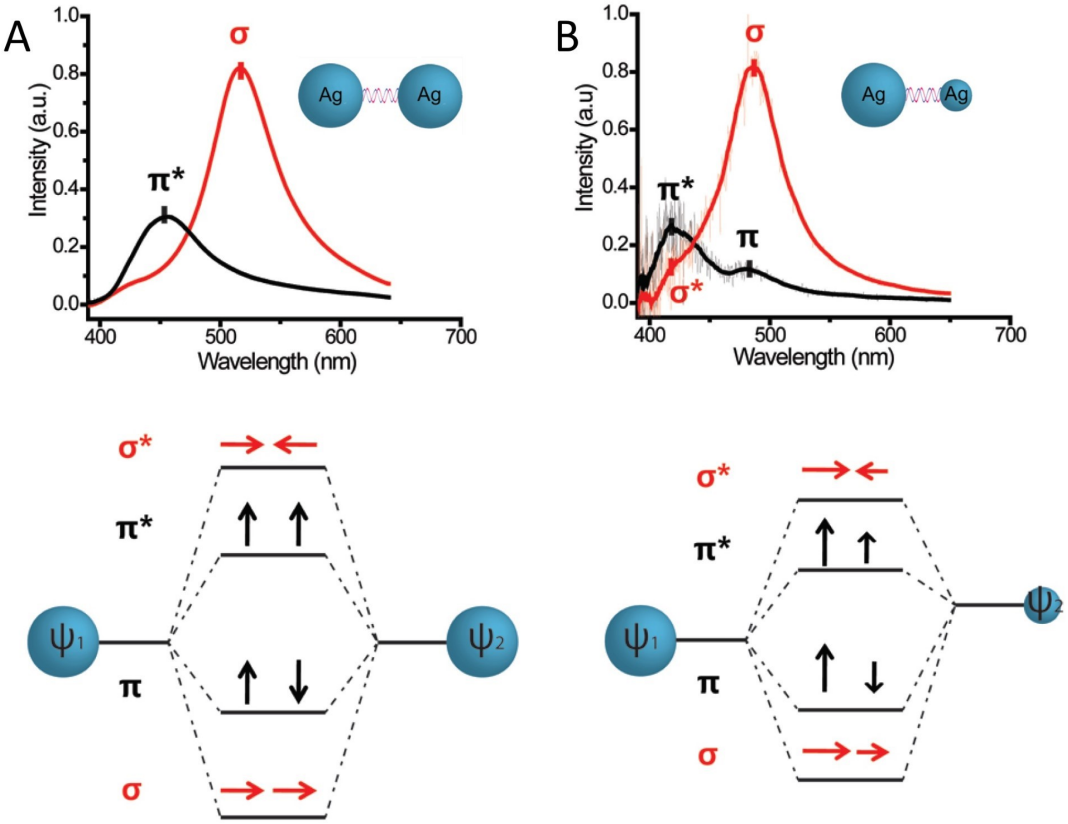

FIGURE 4.6: Experimental realization of plasmon hybridization coupling of silver nanoparticles of **a)** same sizes and **b)** different sizes. DNA linkers were used to control their spacing. Size variation was also used as a parameter to observe hybridized modes. Figure adapted from Ref. [118].

used in the calculations are given in Appendix **??**.

4.5 Conclusions

While exact solutions can be obtained by solving Maxwell Equations numerically, we have provided various analytical solutions for electromagnetic scattering from a spherical scatterer. Each of them provided its own physical insight. First, using the quasistatic approximation, we were able to get a sense of how the incident field is spatially redistributed when encountering a dielectric scatterer. Then, we used the Mie approach to obtain an exact analytical solution. The solution provided terms that

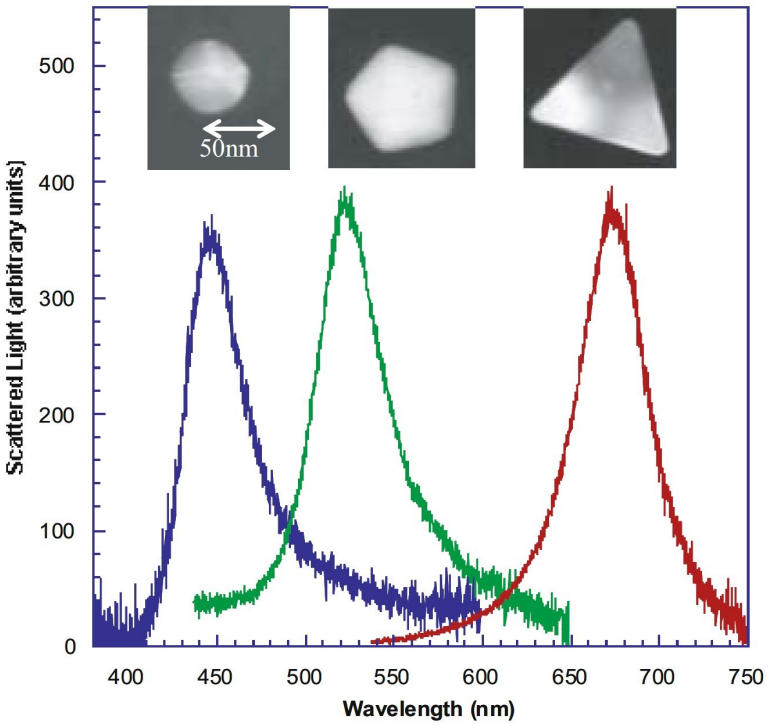

FIGURE 4.7: The resonance of the plasmon is affected by various parameters including geometry, size, composition, and interparticle arrangement. The shown spectra corresponds to experimental darkfield scattering of metallic nanostructures of different geometries along with their correspondent SEM images (insets). Figure adapted from [81].

accounted for retardation effects as well as higher order modes (i.e. quadrupoles). Lastly, interaction between plasmon modes were described in the context of plasmon hybridization and group theory, providing an intuitive physical sense towards plasmon mode coupling.

Chapter 5

Surface Enhanced Raman Spectroscopy (SERS)

This concluding chapter will first provide a quantum mechanical and classical description of SERS. It will then describe how emitters are affected by their surrounding environment. The second part will be devoted to address the main question of this dissertation: the test of the effectiveness of SERS substrates assembled using DNA templates.

5.1 Fundamentals of SERS

Raman scattering was first observed by Chandrasekhara Venkata Raman[1] in 1921 [102]. The Raman process is an inelastic scattering of photons, where energy of incident photons is transferred to the vibrational/rotational energy levels of a molecule. The energy difference is usually expressed in inverse centimeters pcm 1q and is given by,

$$RamanShift = \left(\frac{1}{\lambda_f} - \frac{1}{\lambda_i}\right) \tag{5.1}$$

where $_i$ and $_f$ are the wavelength of the incident and scattered photons, respectively. This Raman shift can be used to infer the energy gap between vibrational/rotational

[1] Nobel Prize 1930

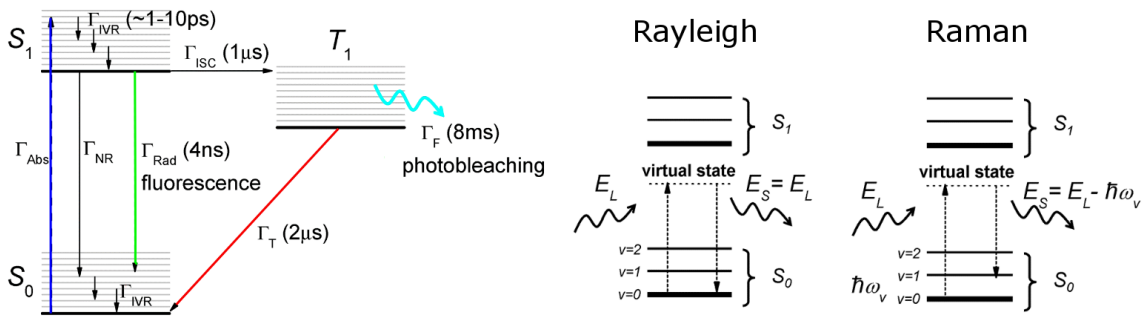

FIGURE 5.1: Jablonski diagram illustrating molecule interaction with incident photons **a)** Luminescence transitions involve energy absorption followed by emission (fluorescence and phosphorescence) **b)** Scattering processes: Rayleigh (elastic) and Raman (inelastic). Scattering processes are instantaneous and do not involve photon absorption.

levels. The scattered photons can loose (stokes) or gain (antistokes) energy depending if the molecule gets excited or relaxed. Raman spectroscopy has several advantages over other spectroscopic techniques: it is highly specific, it works with any incident wavelength, and virtually any molecule can exhibit a Raman spectra. Unfortunately, the Raman scattering cross section is small; SERS greatly increases the signal by utilizing the regions of intense electric field created near granular metallic surfaces. As described on Chapter 4, these "hot spots" are the result of localized surface plasmon modes resonantly excited by the incident laser. The analyte molecules that happen to be positioned in the hot spots provide disproportionately high contribution to the Raman scattering, resulting in a signal enhancement of several orders of magnitude [58, 105]. The great enhancement of the signal generated by SERS can be used to probe single-molecules, and to examine the plasmonic properties of metal assemblies.

Atoms can interact with photons through absorption, emission (spontaneous or stimulated), and scattering; and can result on interband electron transitions. In addition, molecules posses vibrations and rotations states which can be indirectly accessed by incident photons. First, incident photons distort the electronic cloud of the molecule. The oscillating electrons then couples to the vibrational/rotational

states. Luminescence is two-step processes which involves the absorption of a photon followed by its emission. The most common types of luminescence are fluorescence and phosphorescence. A different type of photon-molecule interaction is the scattering process. Depending on the energy difference between incident and scattered photon, scattering can be classified as Rayleigh (elastic) or Raman (ineslastic). Figure **??** shows the Jablonski diagram of various light-matter interactions. While both luminescence and Raman involve a change in the incident photon's energy, it is important to emphasize that scattering is an instantaneous process, and does not involve the absorption/emission of photons, as fluorescence does. In addition, Raman scattering cross section is several orders of magnitude smaller than luminescence processes. Let's first look at the quantum mechanical formalism of photon-molecule interaction, followed by a classical description of Raman scattering.

5.1.1 Molecule-Photon Interactions

The process of photon absorption and emission can be described using first order perturbation theory. The transition probability between two states with energy gap $\triangle E = \hbar\omega_{fi}$ and sinusodial perturbation $\hat{\mathbf{W}} = W sin(\omega t)$ is given by (Appendix A.3.1) and Refs. [17, 40]),

$$P_{f,i}(t,\omega) = \frac{||W_{i,f}|^2}{4\pi\hbar^2}\left|\frac{1-e^{it(\omega_{fi}+\omega)}}{\omega_{fi}+\omega} - \frac{1-e^{it(\omega_{fi}-\omega)}}{\omega_{fi}-\omega}\right|^2 \tag{5.2}$$

This result shows that there are two frequencies at which the perturbation (incident photons) can be in resonance with a two level system. This can induce an absorption of a photon ($E_n = E_1 + \hbar\omega$) or an stimulated emission ($E_n = E_1 - \hbar\omega$). A third process referred to as spontaneous emission occurs when a photon from an excited state couples in any direction or polarization toward the continuum [17, Chp. DXIII].

Raman scattering can be described with second-order time-dependent perturba-

tion theory [68]. Through a similar treatment the transition probabilities are given by (Appendix A.3.1),

$$\frac{1}{\tau} = \frac{2\pi}{\hbar^2} \sum_i \left| < b_i|H'|a > + \sum_c \frac{< b|H'|c >< c|H'|a >}{E_a - E_b} \right|^2 \tag{5.3}$$

The first term represents absorption or emission of a photon involving a change in the state of the molecule, $|a>$ to state $|b>$. The second term is a two-photon process. One can think of this transition as mediated by an intermediate virtual state $|c>$ located anywhere within the energy spectra. The key point is that this transition is instantaneous in nature. If the virtual state is at the same position as an energy level it is called resonant Raman scattering. Selection rules determine which transitions are allowed. IR spectra is complementary to Raman spectroscopy, since each spectra might display different transitions.

Let's now describe the Raman scattering from a classical point of view. Incident photons cause induced polarization of the electron cloud which then couples to the atomic nuclei and exciting the molecule. The rest of the energy is re-radiated as a photon. The Rayleigh and Raman scattering can be inferred from an expansion of the induced dipole vector (p_{ind}) about their normal modes (Q_k) (Appendix A.3.1),

$$\begin{aligned} p &= \alpha E_o cos(\omega t) \\ &+ \sum_k \left(\frac{\partial \alpha}{\partial Q_k} \right) \frac{Q_k E_o}{2} [cos(\omega_o - \omega_k + \nabla_k)t \\ &+ cos(\omega_o - \omega_k - \nabla_k)t])] \end{aligned} \tag{5.4}$$

This expression tells us that the induced dipole can have three distinct frequencies, each corresponding to a different scattering event: Rayleigh (ω_o), Raman stokes ($\omega_o - \omega_k$), and Raman anti-stokes ($\omega_o + \omega_k$). While the classical description provides a good qualitative understanding of the molecule interaction with radiation, the

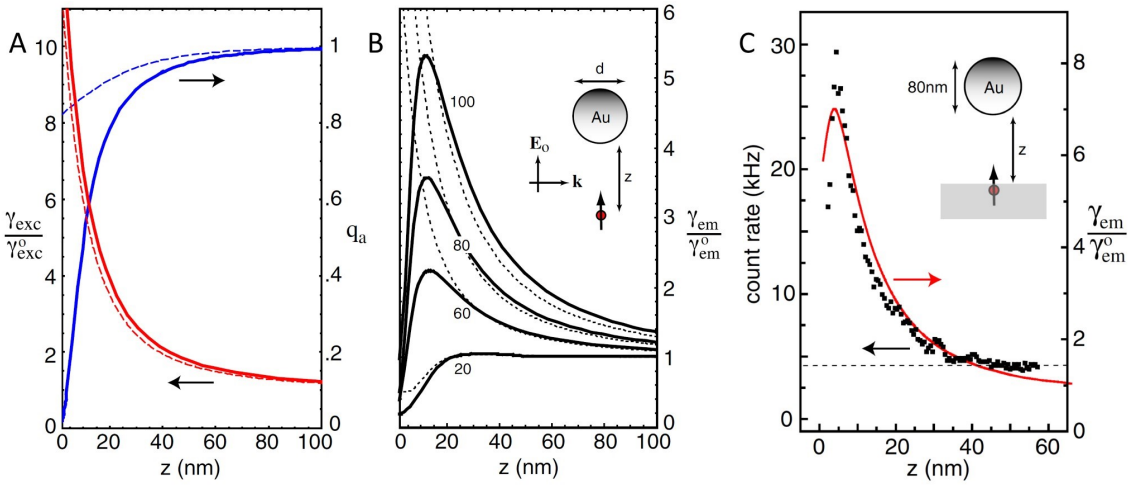

FIGURE 5.2: Competing enhancement versus quenching rates. Radiative and nonradiative decay pathways are influenced by their environment, such in the presence of a nearby metallic nanoparticle. **a)** Excitation rate (red), quantum yield (blue), and **b)** emission rate as a function of distance. **c)** Experimental fluorescence rate between an 80 nm AuNP and an fluorescent emitter. The distance z was varied by attaching the AuNP to an optical fiber supported to a tuning fork crystal. Calculations, experiment, and figure adapted from Ref. [6].

quantum treatment not only provides further insight onto the mechanisms involved on the interactions, but lays down the quantized nature of the energy landscape.

Enhancement and Quenching of Fluorescence

An excited state can decay via radiative and non-radiative pathways. When an excited molecule is placed nearby a metallic particle, multiple effects compete simultaneously: i) the excitation rate γ_{exc} is increased, and the ii) radiative γ_r and iii) non-radiative γ_{nr} (e.g. dipole-dipole) decay rates. It is convenient to define the measurable parameter quantum yield $q_a = \gamma_r \gamma_{tot}$, where γ_{tot} is the total decay rate. The excitation rate $\gamma_{exc} \propto |p \cdot E|^2$ is directly proportional to the strength of the field. The measurable emission rate is proportional to the excitation rate scaled by the amount of radiative decay, $\gamma_{em} = \gamma_{exc}[\gamma_r/\gamma]$. It is more complex in nature since its two competing mechanisms are also enhanced: when very close to the metallic

nanoparticle, both the radiative decay and the multipole-multipole coupling between the excited state and the metalic particle (non-radiative) are enhanced. Figure 5.2 shows calculated values for the quantum yield versus the normalized excitation rate as a function of distance [6]. The dashed line corresponds to a dipole approximation, while the solid line corresponds to a multipole approximation. Figure 5.2 c shows experimental data. The competing nature of both mechanisms is what gives rise to both, enhancement or quenching dependent on the emitters' position. It is clear from the emission rate (Figure 5.2) that there is an ideal separation between the excited system and the metallic nanoparticle where the the enhancement is a maxima. The quenching effect is further increased when the frequency of the emitter overlaps with the frequency of the absorption of the metallic nanoparticle.

Enhancement of SERS

Similar to fluorescence, the environment affects the enhancement of the Raman signal. Since the enhancement of the Raman signal is mostly attributed to the localization of the electric field, it is desired to establish their relation,

$$\begin{aligned} Enhancement &= (EF_{inc})(EF_{rad}) \\ &\propto \frac{|E_{loc}|^2}{|E_{inc}|^2}\frac{|E_{rad}|^2}{|E_{inc}|^2} \end{aligned} \tag{5.5}$$

Here, E_{inc}, E_{loc} and E_{rad} are the incident, local and radiative fields. The rate at which the atom absorbs or emits a photon is proportional to the perturbation's intensity($|E|^2$). The fact that both the rate of absorption and emission are affected by the local field enhancement is intuitive from the quantum mechanical treatment. Remember that Raman scattering is a two-photon process which involves an instantaneous absorption and emission of photons.

A similar argument could be used with fluorescence. An excited state cannot absorb another photon unless it radiates back to return to the ground state. Increas-

ing the rate at which the atom spontaneously decay will certainly increase the rate at which the signal is detected. Nonetheless, for fluorescence nonradiative emission starts to dominate at close enough distances (quenching), decreasing the $|E|^4$ factor.

We have already discussed that a metallic nanoparticles can enhance the Raman signal of an emitter due to the spatial localization of the incident field (Chp. 4). Calculations show that this sole enhancement does not seem to justify the large values observed on SERS substrates. For that, an additional chemical-enhancement effect that adds to the electromagnetic enhancement has been proposed. Two mechanisms are thought to be responsible for the chemical-enhancement: i) plasmon-excited electrons could be directly transferred onto the molecule, and/or ii) plasmons could disturb the electronic states by lowering the HOMO-LUMO gap. It is commonly accepted that the electromagnetic enhancement is greater than the chemical effect [105] and it is expected that the Raman signal is enhanced at a maximum when the incident radiation is at the same frequency as the plasmon resonance.

To compare the enhancement among different SERS substrates, the concept of Enhancement Factor (EF) is used [105, Chp. 4]. Unfortunately, there is not a standard methodology to measure the EF, and even Raman signals between different molecules have been used just for comparison [59]. It is known that Raman scattering cross sections among molecules can vary up to 7 orders of magnitude [105] and not surprisingly there have been reports of enhancements up to 10^14. The average EF is defined as,

$$AEF = \frac{I_{SERS}/N_{RAMAN}}{I_{RAMAN}/N_{RAMAN}} \tag{5.6}$$

Here, I_{SERS} is the intensity using the SERS substrate, I_{Raman} using a solution of known concentration, and N is the number of molecules within the laser spot for each case. This methodology nonetheless neglects the substrate contribution into the Raman signal. For that, a common technique is to compare the EF using molecules

sitting on a plain substrate, under the exact same conditions (i.e. laser intensity, concentration of molecules). However, it is difficult to estimate the concentration of molecules deposited on SERS substrates. For example, the adsorption properties of molecules varies across different substrates. Additionally, the layers on direct contact with the SERS substrate have a different contribution the the subsequent layers, as the signal of the field decreases. Lastly, the molecular orientation in respect to the incident polarization is fixed for molecules chemically attached on a substrate but not in solution. To avoid all these uncertainties, we compared in our experiments the EF of the same substrates with and without hot spots. Measurement details and further discussion follows.

5.2 DNA as SERS Substrates

As we have seen in Chapter 2, DNA origami is a novel self-assembly technique allowing one to form various 2D shapes and position matter with nanometer accuracy. We use DNA origami templates to engineer Surface Enhanced Raman Scattering (SERS) substrates. Specifically, gold nanoparticles were selectively placed on the corners of rectangular origami and subsequently enlarged via solution-based metal deposition. The resulting assemblies exhibit hot spots of enhanced electromagnetic field between the nanoparticles. We observed a significant enhancement of the Raman signal from molecules covalently attached to the assemblies, as compared to control nanoparticle samples which lack inter-particle hot spots. Furthermore, Raman molecules were used to map out the hot spots' distribution, as they were burned when experiencing a threshold electric field. This method opens up the prospects of using DNA origami to rationally engineer and assemble plasmonic structures for molecular spectroscopy.

Building on the massively parallel formation of DNA origami and their capability

to serve as a nanobreadboard, one can further envision using them as biosensors. DNA origami templates have recently been used to promote interactions between attached nanocomponents, such as plasmonic coupling between gold nanorods [87] or gold nanoparticles [62], as well as enhancement and quenching of fluorophores [1, 2] or CdSe QDs [60].. One particularly attractive goal is to facilitate Raman spectroscopy, which provides a highly specific chemical fingerprint.

Pairwise complementary DNA strands can be used to position Raman-active molecules between functionalized gold nanoparticles (AuNPs), thus fabricating plasmonic structures with active hot spots [16, 37, 65, 64]. Although these methodologies have resulted in a reproducible enhanced Raman signal, they are somewhat limited by the fixed shape of the metallic structures, which in turn determines their plasmon modes. It is a common consensus that it is challenging to produce rationale NPs assemblies solely using DNA linkers due their lack of rigidity. Furthermore, one requires discretely functionalized NPs (e.g. with one or two strands) to selectively obtain discrete subunits [103]. DNA origami may serve as a nanobreadboard to controllably attach metallic nanoparticles. It has recently been shown that this NPs can be further enlarged via an in-solution metallization to create complex arbitrary metallic shapes [96, 113]. Here, we report on Raman measurements using these metallic assemblies and determine their suitability as SERS substrates.

We utilized DNA origami to fabricate more complex multi-particle assemblies, and determined their performance as SERS substrates. Specifically, we used DNA origami to organize the metallic structures, and then covalently attached Raman-active molecules to the metal. We found that the substrates with four nanoparticles (NPs) per origami produce a strongly enhanced Raman signal compared to the control samples with only one nanoparticle per origami. Indeed, the small gaps between closely spaced nanoparticles result in hot spots, which are absent in samples with individual nanoparticles (Figure 5.3). Furthermore, the Raman signal systematically

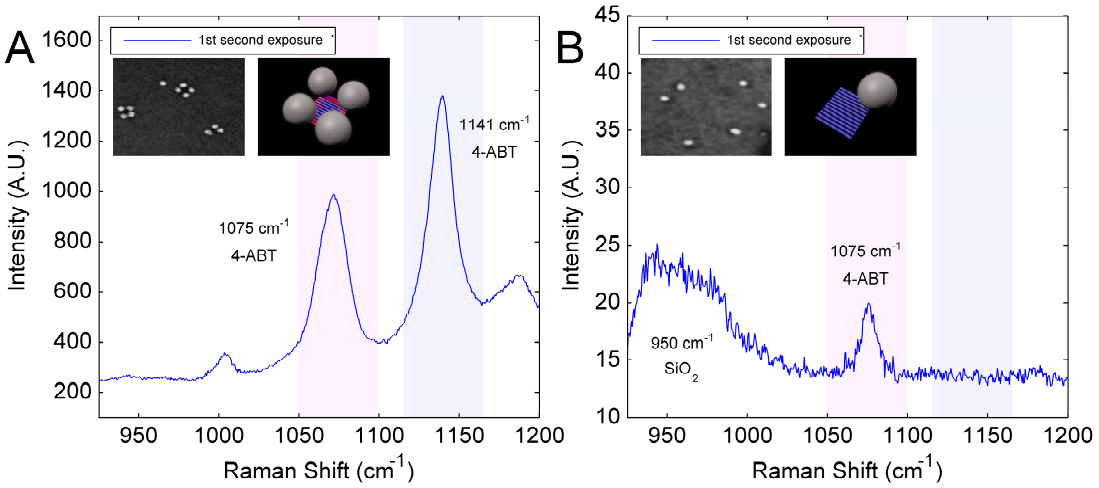

FIGURE 5.3: Typical SERS spectra of 4-aminobenzenethiol (4-ABT) attached to metal nanoparticles assembled on DNA origami. **a)** Four-particle assemblies ("tetramers") which have interparticle hot spots; **b)** control sample with one AuNP per origami ("monomers") which lack the interparticle hot spots. Spectra correspond to the first 1 second of the laser exposure and are normalized to the average density of nanoparticles in the illuminated region. Insets: SEM images taken from the measurement areas and cartoons representing the target structure. The origami template is shown in blue, while the red tint in (a) indicates the regions of enhanced electric field (hot spots).

decayed as a function of the laser exposure time in the samples with four particles per origami. We attribute this behavior to molecular damage caused by the high electric field at the hot spots. The one-particle control samples lacking the interparticle hot spots exhibited no such decay.

5.3 Results and discussion

We use DNA origami to control the composition, shape, geometry and arrangement of metallic structures, which in turn determine the local distribution of electromagnetic fields. DNA-metallic assemblies were prepared as we previously reported [96]. Briefly, select staple strands of the standard "tall" rectangular DNA origami ($90x70\ nm^2$) are extended by a specific ss-DNA sequence, referred to as X_{24}. The sequence serves as an anchor for AuNPs; to increase the binding probability the

anchors were positioned in pairs on adjacent staples. The AuNPs are conjugated with 5 complementary sequence strands ($X_{24,comp}$) through standard thiol chemistry [69]. Appendix D.2 has a list of sequences used on the modified DNA strands).

Two different types of SERS samples were prepared: in the sample with engineered hot spots, four AuNPs were attached to each of the four corners of the origami template (tetramer samples); in the control samples, only one AuNP was placed in one of the corners (monomer samples). Each of the modified DNA template designs was attached to RCA cleaned (SC-1 and SC-2) and oxygen plasma ashed (SPI Plasma Prep II, 20 min, 100 mA) silicon dioxide substrates (1 m oxide, Silicon Quest) using a 10x TAE/125 mM/Mg^{2+} solution (the final DNA origami concentration was 0.5 nM). Functionalized AuNPs were then added to the solution (final concentration of 10 nM) resulting on the attachment to the origami templates. They were then incubated for 15 min and rinsed in DI water for 15 seconds, followed by gentle drying with nitrogen. We chose to assemble tetramers as opposed to dimers because they exhibit interesting plasmonic properties such as Fano resonances [116] which have been shown to provide much greater SERS enhancement due to near-field intensity variations [137]. The present work is a proof of concept that DNA origami can be used to assemble complex metallic structures for optical applications such as SERS substrates. The structures were then enlarged using a commercial silver metallization kit following the manufacturer directions (HQ silver enhancement, Nanoprobes INC), as performed in our previous works [90, 96] and described on Chapter 2. The incubation time was 12 min for the tetramer structures. This was the necessary time to have the nanoparticles closely spaced but typically not touching, permitting the formation of interparticle hot spots. The control samples were incubated for 10 min to achieve the same average NP size of 50 nm. Although measuring the gap between nanoparticles with nanometer precision is challenging, we estimate the average gap size to be below 3 nm (Figure 5.5). This separation distance was clearly

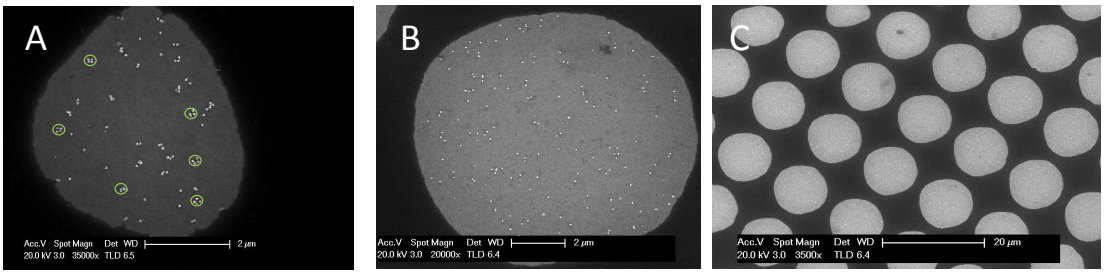

FIGURE 5.4: Typical SEM images of lithographically modified samples for **a)** designed structures ("tetramers") and **b)** control samples ("monomers"). **c)** Zoom-out of PMMA windows. The windows where no abnormal structures are present are selected to perform measurements.

small enough to produce a strong signal enhancement, as demonstrated from the Raman spectra (Figure 5.3). We lithographically patterned the samples with a set of markers, which allowed us to identify specific regions where the spectra were taken. Specifically, we spin-coated PMMA-A4 (MicroChem Corp.), followed by a 5 min UV exposure and development to open 10 μm windows (Figure 5.4). The samples were then imaged using a Scanning Electron Microscope (SEM); we selected for further study the windows which showed no abnormally assembled structures such as the multi-particle clusters seen in Figure 5.5. We also measured the average nanoparticle density in each window, used for normalization purposes. The Raman spectra exhibit no discernible difference before or after lithographic patterning. The samples were then incubated in a 5 mM solution of 4-aminobenzenethiol (4ABT) in ethanol for two hours (long enough to reach full surface coverage). Placement of multiple Raman molecules throughout the hot spot is imperative to obtain an estimate of the enhancement factor, which is not possible with a single molecule. The thiol functional group ensures that the Raman-active molecules are covalently attached only to the metallic surfaces. The samples were then thoroughly rinsed in pure ethanol to remove any physisorbed molecules. Similarly treated SiO2 substrates without NPs showed no detectable 4-ABT Raman signal, indicating the effectiveness of the

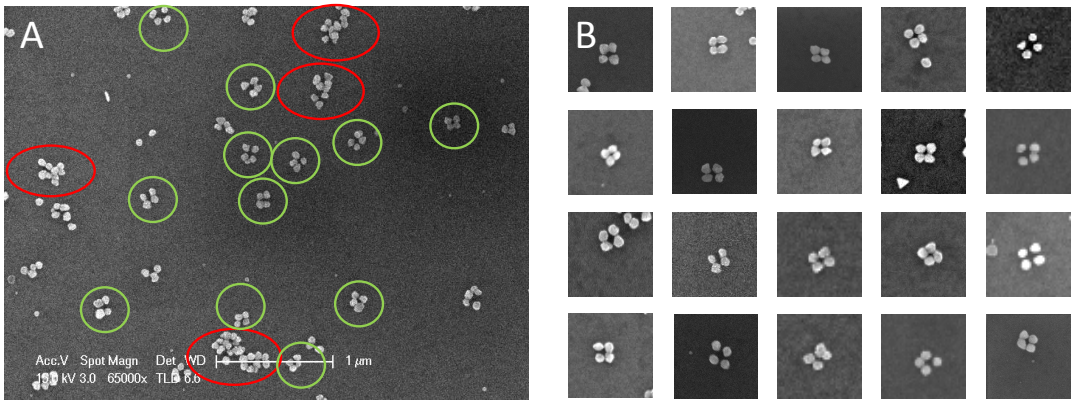

FIGURE 5.5: **a)** SEM images showing abnormal structures (red) and target structures (green). Lithographically modified windows allow us to select areas where no abnormal structures are present. **b)** Grid of zoomed-in SEM images of various tetramer structures.

rinsing procedure (Incidentally, we did not observe Raman signatures of any other molecules, such as DNA).

The Raman spectra were obtained using a Jobin Yvon LabRam ARAMIS (Horiba, Ltd) spectrometer using a 632.8 nm, 5 mW HeNe laser excitation, focused by a 100x objective to a 1 m spot. Figure 5.3 compares the Raman signal measured from tetramer and monomer samples during the first second exposure at maximal laser intensity (Io). The spectra were normalized to the average NP number in the corresponding lithographic window. We verified that the magnitude of Raman signal per particle was reproducible in other regions. The average relative Raman enhancement per NP is 100 in tetramer vs. monomer samples. Note that using the monomer samples as a control ensures that the surface concentration of the covalently attached 4-ABT layer is the same as in the tetramer samples. This eliminates the uncertainty in determining the SERS enhancement factor, common for the measurements which use molecular solutions as a control [105].

The observed SERS enhancement is naturally explained by the hot spots created in the tetramer sample. Numerical simulations indicate that the hot spots are located

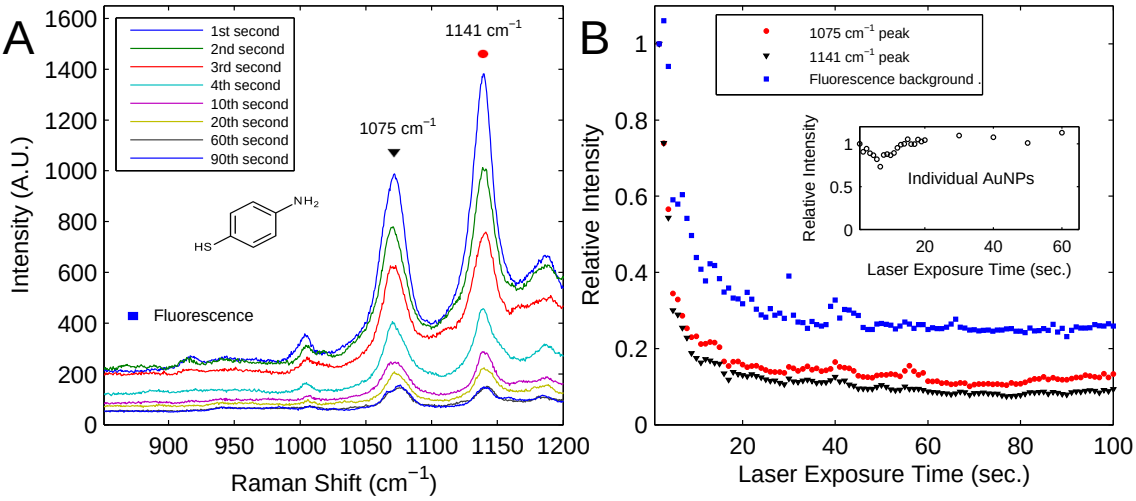

FIGURE 5.6: **a)** Raman spectra taken by repeatedly exposing the tetramer sample to 1 second HeNe laser pulses. b) Intensity of the 1075 cm^{-1} and 1141 cm^{-1} Raman peaks (background subtracted) and the fluorescence background as a function of the laser exposure time. The rapid decay is attributed to the photo-damage of the molecules caused by the intense field at the hot spots.

between pairs of NPs (see cartoon in Figure 5.7 c) similar to the hot spots created in nanoparticle dimers. Unlike dimers, where the enhancement disappears for an electric field perpendicular to the dimer axis, the hot spots in the tetramers should be activated by any laser polarization. Our control monomer samples lack the inter-particle hot spots; although the electric field is also enhanced at the particle poles, the enhancement factor should be much smaller, and we disregard it in the following discussion. Notice also that the 1141 cm^{-1} Raman mode (blue shadow on Figure 5.3) is no longer observed from the monomer samples. This can be attributed to a strong chemical dependence of the Raman mode, which requires a minimum excitation energy in order to promote a charge transfer [56, 55].

The importance of the hot spots is further evidenced by the time evolution of the Raman signal. Figure 5.6 a shows the sequence of spectra taken during successive 1 second exposures. The signal intensity initially drops rapidly and then saturates. Similar intensity decay has been attributed to photo-damaging of Raman molecules

by the enhanced field at the hot spots [29, 33, 136]. Alternatively, the decay has been assigned to morphological changes of the metallic structures due to heating [121]. Photo-damage is attributed to two potential causes: i) the molecule is more likely to transit to a Triplet state, which is highly reactive with oxygen, and ii) the field is strong enough to destroy the molecule. Although it is difficult to identify the mechanism responsible for the decay we observe [105], we tentatively attribute it to molecular photo-damage. SEM images of the structures before and after the Raman measurement do not show noticeable differences, within a resolution of a few nanometers. It is also important to emphasize that the molecules are covalently attached to the silver particles through the thiol crosslinker, preventing them from leaving the hot spots (photo-desorption).

Figure 5.6 b shows the integrated Raman signal for the 1075 cm^{-1} (CS stretch, 7a1) and the 1141 cm^{-1} (CH bend, b2) peaks, as well as the fluorescence background as a function of the laser exposure time. All the signals are normalized to the values measured at the first 1-second exposure. The signal decays rapidly at first, and then saturates at a constant value. The inset of Figure 5.6 b shows the integrated intensity of the 1075 cm^{-1} peak measured from the control monomer sample; no signal decay is observed in this case due to the lack of interparticle hot spots.

The saturation of the Raman signal after about 100 seconds allows us to further characterize the electric field enhancement in the hot spots [33, 28]. We assume that only the molecules experiencing an electric field exceeding a certain critical value are destroyed [105] No signal decay is observed at 1% of the maximal laser intensity I_o, indicating that the critical field is not yet reached even in the hot spots. To study the successive photo-damage of the hot spots by the laser, we increased the illumination intensity to 10%, 25%, 50% and 100% of I_o. Each successive increase of the intensity is followed by the gradual decay of the Raman signal, similar to the decay shown in Figure5.6. This behavior indicates the step-wise expansion of the regions where the

field exceeds the critical value and the molecules are photo-damaged (see schematics in Figure 5.7 c. As a result, the ratio of the time-saturated Raman signal to the laser intensity decreases with increasing intensity.

Figure 5.7 a illustrates this behavior by showing the time-saturated spectra for each subsequent intensity increment, all measured from the same spot. Notice the decay of the relative intensity of the 4-ABT Raman signal at 1075 cm^{-1} as compared to the substrate Raman band centered at 950 cm^{-1}. The latter signal was verified to scale proportionally to the laser intensity, while the 4-ABT signal is clearly sublinear: for example, at the full intensity of I_o the 4-ABT Raman peak is barely visible relative to the 950 cm^{-1} band, while at 1% of I_o the 4-ABT Raman peak dominates (this figure is not normalized to the number of particles. Also, it is measured from a more dilute sample compared to Figures 5.3 and 5.6, which increases the relative prominence of the 950 cm^{-1} substrate band and allows us to visualize the effect). In Figure 5.7 b, we plot the ratio of the 4-ABT Raman signal to the laser intensity, I_o. The horizontal axis is $\sqrt{I_o/I}$, proportional to the inverse incident electric field [33, 136]. Data taken at three different spots are represented by different colors, all normalized to 1 at $I = I_o$. In each of the curves, the relative Raman signal at $I = 0.01I_o$ is 20-40 times stronger than the signal at I_o. In other words, at the maximal laser intensity the high fields of the hot spots damage the molecules responsible for most of the Raman enhancement that was achieved at 1% of the intensity. Still, we recall that at I_o the signal measured from the tetramer sample is 100 times stronger compared to the monomers. Since the threshold photo-damage field is not yet reached in the monomer samples, even at I_o, their Raman signal should scale proportionally to the laser intensity. Therefore, at 1% of I_o, the enhancement factor of the tetramer could potentially reach 2000-4000. Unfortunately, the direct comparison was not feasible, because the Raman signal of the monomer sample was too weak at $0.01I_o$, while at I_o the Raman signal from the tetramer samples experiences a very significant

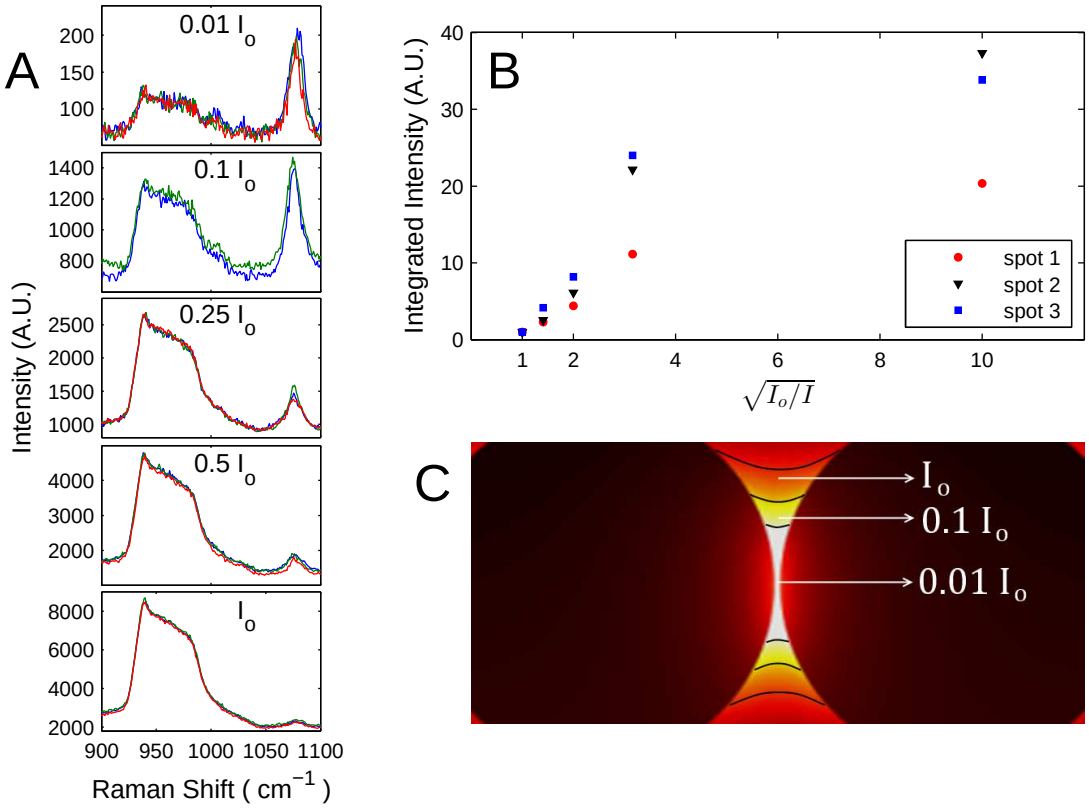

FIGURE 5.7: **a)** Raman spectra in the vicinity of the 950 $^{-1}$ substrate band and the 1075 $^{-1}$ 4-ABT peak. Each spectrum is taken after increasing the laser intensity to 1%, 10%, 25%, 50% and 100% of I_o and waiting for the signal to saturate at the new intensity level. Two or three spectra are consecutively taken at each intensity level, demonstrating the saturation of the signal. **b)** Ratio of the timesaturated 4-ABT Raman peak (background subtracted) to the laser intensity I as a function of $\sqrt{I_o/I} \propto 1/E$. The colored data sets correspond to different locations on the sample and are scaled to 1 at I I0. **(c)** Cartoon showing the electric field enhancement regions within the hot spot. Optical filters are interchanged in order to increase the incident field in steps, burning the molecules located in progressively larger regions of the hot spots.

degradation prior to the completion of the first 1-second exposure.

5.4 Conclusions

We have shown that DNA origami can be successfully used to engineer substrates for Surface Enhanced Raman Spectroscopy. The Raman signal of 4-ABT molecules deposited on the tetramer NP assemblies is enhanced at least a hundred times (and

potentially several thousand) per nanoparticle as compared to control samples with individual nanoparticles. The enhancement is due to hot spots, whose existence was verified by time and intensity-dependent measurements.

Chapter 6

Conclusions

Throughout this work, I have shown that it is possible to use DNA to controllably place metallic nanoparticles with nanometer resolution. Specifically, DNA Origami's effectiveness to be used as programmable templates was tested. The resulting structures demonstrate the design capabilities that origami-based metallic structures can offer for spectroscopic and plasmonic applications. The pre-programmability and self-assembly nature of DNA presents an unmatched methodology to massively form structures that are able to couple optically.

In the future, it is desired to use the addressability of the DNA origami to custom tune the plasmon resonance frequency of the DNA metallic structures by exploring different shapes and materials. This would allow to tailor the plasmonic resonances to match the laser frequency and/or the optimal excitation band of a given molecule. The methodology presented here opens up new possibilities to rationally engineer substrates using DNA origami for optical and plasmonic applications.

As the field moves forward, there are several challenges DNA Nanotechnology needs to address (and that many groups currently are):

1. Improvement of DNA-based structures rigidity
2. Reduce of assembly errors (e.g. missing staples)
3. Controllable placement and positioning of DNA structures on substrates [44]

4. Expansion of DNA-origami's maximal length [73]

Since the visionary proposal of Seeman in the 80's [115], the great advances made during the past decade shows that structural DNA is reaching a new stage of maturity. As interdisciplinary as it is, DNA Nanotechnology posses the necessary qualities to be integrated with other experimental techniques, making it a exciting area of current research.

Appendix A

Mathematical Formulations

A.1 Analytical Approaches for Plasmons

A.1.1 Quasi-static Approximation

For a spherical geometry or radius r immersed in a constant electric field E, the solution must satisfy the Laplace equation $\nabla^2\Phi = 0$ and the boundary conditions (following the approach from Jackson, Ref. [46])

$$\begin{aligned} \Phi_{in} &= \sum_{l=o}^{\infty} A_l r^l P_l(cos\theta) \\ \Phi_{out} &= \sum_{l=o}^{\infty} \left[B_l r^l + C_l r^{l+1}\right] P_l(cos\theta) \end{aligned} \tag{A.1}$$

Applying the boundary condition at infinity, the field must become,

$$\Phi \rightarrow E_o z = E_o r cos\theta \tag{A.2}$$

so $C_l = 0$ and $B_l = Eo$. The boundary conditions at $r = a$ require that,

$$\Phi_{in} = \Phi - out \tag{A.3}$$

$$\epsilon \frac{\partial \Phi_{in}}{\partial r} = \epsilon_o \frac{\partial \Phi_{out}}{\partial r} \tag{A.4}$$

All A_l and C_l terms are zero for $l \neq 0$. The only surviving terms provide,

$$\begin{aligned}
\Phi_{in} &= \frac{3\epsilon_d}{\epsilon + 2\epsilon_d} E_o r cos\theta \\
\Phi_{out} &= E_o r cos\theta + \frac{\epsilon - \epsilon_d}{\epsilon - 2\epsilon_d} E_o \frac{a^3}{r^2} cos\theta \\
&= E_o r cos\theta + \alpha \frac{a^3}{4\pi r^2} \cos\theta
\end{aligned} \tag{A.5}$$

where $\alpha = 4\pi a^3 \frac{\epsilon - \epsilon_d}{\epsilon + 2\epsilon_d} E_o$. The electric field is found by,

$$\begin{aligned}
E &= -\nabla\Phi \\
E_{in} &= \frac{3\epsilon_d}{\epsilon(\omega) + 2\epsilon_d} E_o \\
E_{out} &= E_o \frac{\epsilon(\omega) - \epsilon_d}{\epsilon(\omega) + 2\epsilon} E_o \left(2cos\theta\hat{\mathbf{r}} + sin\theta\hat{\theta}\right)\hat{\mathbf{z}}
\end{aligned} \tag{A.6}$$

The time dependence is incorporated by realizing that the results are similar to a dipole immersed on a constant electric field. One can then treat the system as an oscillatory dipole with time dependence $e^{i\omega t}$. The electric field is then given by,

$$E_{out} = E_o + \frac{|3n(n \cdot p) - p|}{4\pi\epsilon_o\epsilon_d} \frac{1}{r^3} \tag{A.7}$$

The cross sections can be found via the poynting vector or by relating the scattered and absorbed power with the incident power ($C_{sca} = I_{sca}/I_{inc}$ and $C_{abs} = I/I_{inc}$),

$$\begin{aligned}
\sigma_{sca} &= \frac{k^4}{6\pi}\alpha^2 \propto \frac{a^6}{\lambda^4} \\
\sigma_{abs} &= k\ Im(\alpha) \propto \frac{a^3}{\lambda}
\end{aligned} \tag{A.8}$$

A.1.2 Mie Solution Approach

For a spherical geometry, it is convenient to expand kprq as an infinite sum of spherical harmonics,

$$\psi_k(r) = \sum_{l,m} \psi_{klm}(r) \tag{A.9}$$

where

$$\psi_{klm}(r) = R_{kl}(r)Y_l^m(\theta,\phi) = \frac{u_l(r,k)}{r}Y_l^m(\theta,\phi) \tag{A.10}$$

The radial equation can then be written as,

$$\frac{d^2}{dr^2} + \left(k^2 - \frac{l(l+1)}{r^2}\right)(r\ u_l(r,k)) = 0 \tag{A.11}$$

which have as solutions the Ricatti-Bessel functions,

$$h_k(kr)^{1,2} = j_l(kr) \pm iy_l(kr) \tag{A.12}$$

The general solution is expressed as,

$$\psi_k(r) = \sum_{l,m}\left[A_{lm}h_l^1(kr) + B_{lm}h_l^2(kr)\right]Y_l^m(\theta\phi) \tag{A.13}$$

which for spherical scatterers (i.e. $m = 0$) reduces to

$$\psi_k(r) = \sum_{l,m}\left[A_{lm}h_l^1(kr) + B_{lm}h_l^2(kr)\right]P_l(cos\theta) \tag{A.14}$$

The incident wave is described by, An incident plane wave can be written as,

$$E = E_1 e^{i(k\cdot r - \omega t} \tag{A.15}$$

where we can perform the partial-wave expansion,

$$\begin{aligned}\psi_k(r) &= e^{ikrcos\theta} \\ &= \sum_{l=0}^{\infty}(2l+1)i^l\ j_l(kr)P_l(cos\theta)\end{aligned} \tag{A.16}$$

It is convenient to decompose the incident field onto perpendicular and parallel vectors E1 and E2 with respect to the scattering plane. For spherical scatterers, a scattering amplitude matrix can be written as,

$$\begin{pmatrix}E_2\\E_1\end{pmatrix} = \frac{e^{ikr}}{ikr}\begin{pmatrix}S_2 & 0\\0 & S1\end{pmatrix}\begin{pmatrix}E_2\\E_1\end{pmatrix}_{inc} \tag{A.17}$$

With the appropriate boundary conditions, the Mie scattering coefficients for a spherical scatterer are given by [48, Chp. 3, p. 83], [13, Chp. 4] or [123, Chp. 9],

$$E_{sca} = \frac{i}{kr} E_o [S_2 cos(\phi)\hat{\theta} + S_1 sin(\phi)\hat{\phi}] \tag{A.18}$$

S_1 and S_2 are the scattering amplitudes and are given by,

$$\begin{aligned} S_1 &= \sum_{l=1}^{\infty} \frac{2l+1}{l(l+1)} (a_l \pi_l + b_l \tau_l) \\ S_2 &= \sum_{l=1}^{\infty} \frac{2l+1}{l(l+1)} (b_l \pi_l + a_l \tau_l) \end{aligned} \tag{A.19}$$

Here, $\pi_l = \frac{P_l^1(cos\theta)}{sin(\theta)}$ and $\pi_l = \frac{\partial P_l^1(cos\theta)}{\partial \theta}$, and P_l^1 are the known Legendre polynomials. The Mie coefficients a_l and b_l can be expressed in terms of the Bessel functions, as a function of the frequency. They are responsible for determining the amplitudes of each oscillation mode.

A.1.3 Plasmon Hybridization Model

Here we follow the treatment from [14, Chp. 4] and first described on [84, 100]. Such fluid can be described using the continuity equation,

$$\frac{\partial \rho}{\partial t} + \nabla \cdot j = 0 \tag{A.20}$$

The electron charge density ρ has a current density $j = \rho v$, where v is the electron-plasma velocity. Incompressibility requires ρ to be constant, while irrotationality that $\nabla \times j = 0$. We can define the function ϕ such that $v = \nabla \phi$ and require it to satisfy the Laplace equation, $\nabla^2 \phi = 0$. The induced surface charge density σ must obey

$$\frac{\partial \sigma}{\partial t} = n \cdot j = \rho n \cdot \nabla \phi \tag{A.21}$$

The incompressible fluid is described by the Lagrangian. The kinetic energy of the plasmon fluid can be expressed in terms of the surface integral using the divergence theorem,

$$\begin{aligned} T &= \frac{1}{2}\int_V n_o m_e v^2 dV \\ &= \frac{1}{2}\int_S n_o m_e \phi \nabla\phi \cdot dS \end{aligned} \tag{A.22}$$

Here, m_e is the electron mass, v is the velocity of the charge density, and $n_o = \rho/q$ is the electron number density. The potential energy of the plasmon fluid is given by,

$$U = \int_{S_1}\int_{S_2} \frac{\sigma(r_1)\sigma(r_2)}{|r_1 - r_2|} dS_1 dS_2 \tag{A.23}$$

Using an orthonormal set one can express the scalar potential using the orthonormal set of spherical harmonics,

$$\phi = \sum_{l,m} (\alpha_{lm}\dot{N}_{lm})^2 \frac{r_<^l}{r_>^{l+1}} Y_{lm} \tag{A.24}$$

where r and r are chosen for inside and outside the sphere, respectively. N_{lm} are the spherical harmonic amplitudes. Lets now replace the expanded scalar onto both the kinetic and potential energies of the plasmon fluid. Choosing lm a1pla2l 1q and replacing it on A.22, we obtain for the kinetic energy,

$$\begin{aligned} T &= \frac{n_o m_e}{2}\sum_{l,m} (\alpha_{lm}\dot{N}_{lm})^2 l a^{2l+1} \\ &= \frac{n_o m_e}{2}\sum_{l,m} \dot{N}_{lm}^2 \end{aligned} \tag{A.25}$$

For the potential energy we get,

$$\begin{aligned} U &= 2\pi(n_o q)^2 \sum_{l,m} N_{lm}^2 \frac{l}{2l+1} \\ &= \frac{n_o m_e}{2}\sum_{l,m} \omega_l^2 N_{lm}^2 \end{aligned} \tag{A.26}$$

A.2 Computational Methods

Numerical calculations were performed using both FDTD (COMSOL) and Boundary Element Method (BEM, MNPBEM). COMSOL is a stand alone program with a user-friendly interface. It requires to input all the parameters associated with the calculation. This provides great flexibility and forces one to carefully set the values for the particular environment. This comes at the cost of a steeper learning curve. MNPBEM is a free toolbox that runs on MATLAB environemnt. It is easy to implement since many parameters are already predefined. I found that calculations performed using MNPBEM were significantly faster than using COMSOL. All the calculated results agreed with literature values obtained from similar or other numerical methods. When performing numerical computations it is customary to use permittivity experimental values. These are usually obtained from bulk materials and that there is some discrepancy of values within literature. Commonly used values are the ones provided by Johnson and Christy [47]. The resort to numerical solutions is imperative for the design and prediction of complex plasmonic nanostructures.

A.3 Matter-light interactions

A.3.1 Perturbation Theory of molecular transitions

Quantum treatment of Absorption and Emission The time dependent Schrodinger equation is given by,

$$u\hbar\dot{\psi} = (H_o + \lambda W)\psi \tag{A.27}$$

where H_o is the unperturbed hamiltonian and W is the perturbation with a dimensionless parameter λ. We want to calculate the probability,

$$P = |< \phi_f|\psi(t) >|^2 \tag{A.28}$$

which starts at an initial state $\psi(t=o)=\phi_I$. The time dependent wavefunction can be expanded on the phi basis,

$$\psi=\sum_{n=1}^{\infty}c_n(t)\phi_n \tag{A.29}$$

where $c_n(t)$ is the projection of the wavefunction onto the $|\phi>$ basis. It is convenient to express them as matrix elements,

$$\hat{\mathbf{W}}_{nk}(t)=<\phi_n|\hat{\mathbf{W}}(t)|\phi_k> \tag{A.30}$$

Substituting A.29 into A.27 and upon integration results in the time dependent probability amplitudes,

$$i\hbar\dot{c}_n(t)=E_nc_n(t)+\sum_k c_k\lambda\hat{\mathbf{W}}_{nk}(t)c_k(t) \tag{A.31}$$

Assuming $\lambda\ll 1$, we can treat $c(t)$ to be closed to the unperturbed solution (adiabatic change) $c(t)=b_ne^{-iE_nT/\hbar}$ and express A.32 after some manipulation as,

$$i\hbar\dot{b}_n(t)=\lambda\sum_k e^{i\omega_{nk}t}\hat{\mathbf{W}}_{nk}(t)b_k(t) \tag{A.32}$$

where $\omega_{n,k}=(E_n-E_k)/\hbar$ is the frequency that relates the initial and final states. Now, b_n can be expanded in powers of λ and set equal powers on each side of eq. A.33,

$$i\hbar\dot{b}^1_n(t)=\lambda\sum_k e^{i\omega_{nk}t}\hat{\mathbf{W}}_{nk}(t)b^{l-1}_k(t) \tag{A.33}$$

It can be shown that the first order provides,

$$i\hbar b^1_n(t)=\int_0^t e^{i\omega_{nk}t}\hat{\mathbf{W}}_{nk}(t)dt \tag{A.34}$$

The probability of a transition is therefore given by,

$$P_{i,f}(t)=\frac{1}{\hbar^2}\left|\int_0^t exp(i\omega_{if}t)W_{if}(t)\,dt\right|^2 \tag{A.35}$$

The perturbation matrix element W is dependent of the type of perturbation. A good approximation of incoming radiation is given by a sinusoidal perturbation $\hat{\mathbf{W}}(t) = Wsin(\omega t)$. We get a probability,

$$P_{f,i}(t,\omega) = \frac{|W_{i,f}|^2}{4\pi\hbar^2}\left|\frac{1-e^{it(\omega_{fi}+\omega)}}{\omega_{fi}+\omega} - \frac{1-e^{it(\omega_{fi}-\omega)}}{\omega_{fi}-\omega}\right|^2 \tag{A.36}$$

Quantum treatment of Scattering

The wavefunction of an atom or molecule in state $|a>$ is given by,

$$\psi(t) = e^{-i\hat{\mathbf{H}}t/\hbar}|a> \tag{A.37}$$

with transition probability to state $|b>$,

$$P = \left|<b|e^{-i\hat{\mathbf{H}}t/\hbar}|a>\right|^2 \tag{A.38}$$

The transition rate to any state is given by,

$$\frac{1}{\tau} = \frac{d}{dt}\sum_b \left|<b|e^{-i\hat{\mathbf{H}}t/\hbar}|a>\right|^2 \tag{A.39}$$

Using standard perturbation theory one obtains,

$$\frac{1}{\tau} = \frac{2\pi}{\hbar^2}\sum_i \left|<b_i|H'|a> + \sum_c \frac{<b|H'|c><c|H'|a>}{E_a - E_b}\right|^2 \tag{A.40}$$

Classical Raman Effect

A photon with frequency $Ecos(\omega t)$ induces a dipole,

$$p = \alpha E_o cos(\omega_o t) \tag{A.41}$$

Here, is the molecule's polarizability tensor and is dependent on the shape of the molecule. The polarizability tensor can then be expanded in respect to the normal

modes of the molecule,

$$\alpha = \alpha_o + \sum_k \left(\frac{\partial \alpha}{\partial Q_k}\right)_o Q_k + \frac{1}{2}\sum_{k,l} \frac{\partial^2 \alpha}{\partial Q_k \partial Q_l} Q_k Q_l \tag{A.42}$$

Here o is the polarizability of the molecule at equilibrium, and Qi represents the normal coordinates of vibration. Keeping only up to the first linear term of the expansion and adding time dependence,

$$\alpha = \alpha_o + \sum_k \left(\frac{\partial \alpha}{\partial Q_k}\right)_o Q_k cos(\omega_k t + \delta_k) \tag{A.43}$$

the polarization of the molecules is expressed as,

$$\begin{aligned} p &= \alpha E_o cos(\omega t) \\ &+ \sum_k \left(\frac{\partial \alpha}{\partial Q_k}\right) Q_k E_o cos(\omega_k t + \delta_k) cos(\omega t) \end{aligned} \tag{A.44}$$

which can be expressed as,

$$\begin{aligned} p &= \alpha E_o cos(\omega t) \\ &+ \sum_k \left(\frac{\partial \alpha}{\partial Q_k}\right) \frac{Q_k E_o}{2} [cos(\omega_o - \omega_k + \delta_k)t \\ &+ cos(\omega_o - \omega_k - \delta_k)t])] \end{aligned} \tag{A.45}$$

Each of these terms correspond to the Raleigh (ω_o), stokes ($\omega_o - \omega_k$), and anti-stokes ($\omega_o + \omega_k$) scattering.

Appendix B

Additional Data

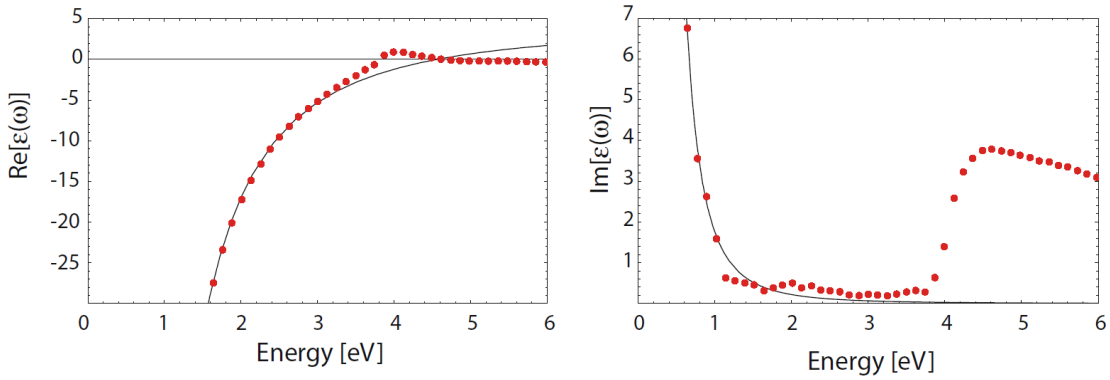

FIGURE B.1: Real and imaginary experimental permittivity values for silver (red dots). Solid line is the free electron model. Figure from Ref. [71].

Appendix C

Instrumentation Details

C.1 Lithography

Samples were spin coated with PMMA-A4 (MicroChem Corp) and baked on a hot plate (120 C surface temperature) for 2 min. A copper grid of 2000 mesh (Structure Probe, Inc) was placed on top and the sample was exposed to UV (500 W) for 5 min.

C.2 Raman measurements

DNA-metallic structures were incubated on a 5 mM 4-aminobenzenethiol ethanolic solution for 4 hrs followed by a thorough rinse on pure ethanol. Raman spectra were obtained using a Jobin Yvon LabRam ARAMIS (Horiba, Ltd) Raman instrumentation. Measurements were taking using a 5 mW HeNe 632.8 nm laser using 1 second intervals. A 100x objective, resolution grating of 1800 grooves, and a slit of 100 μm were used on all measurements. The spectra ranged from 1000 to 1600 cm^{-1}.

Appendix D

Methods

D.1 Experimental Protocols

D.1.1 DNA-AuNPs Conjugation Protocols

Functionalization - Phosphination Method

Following the recipe of Refs. [69, 140], 3 mg of bis(p-sulfonatophenyl)phenylphosphine (BSPP, Sigma-Aldrich) were added to 10 ml of purchased AuNP solution (British Biocell International). After overnight incubation, the AuNPs were concentrated by adding 260 mg of NaCl and centrifuging for 30 min at 800 g. The supernatant was removed without disturbing the visible Au pellet. 200 μl of methanol and 200 μl of BSPP (3 mg in 10 mL DI water) were added, after which the solution was centrifuged a second time for 30 min. The supernatant was again removed and the AuNPs were resuspended in the same BSPP solution to a total volume of 200 mL. Typical AuNP concentrations were 2-3 μM. The disulfide-modified DNA sequence was added at a ratio of 1:5 Au:DNA, at which time the buffer was adjusted to 0.5xTBE/50 mM NaCl. After 48 hours of incubation, thiolated T5 strands were added at a Au:T5 ratio of 1:60 to fully backfill the AuNP-DNA conjugates. Excess DNA strands were removed from the AuNP-DNA conjugates by running the conjugate solution on a 3% agarose gel (0.5xTBE) for 20 min, at 10 V/cm. The AuNP-conjugate band was extracted by

cutting out the band of interest, finely chopping it and centrifuging it using a Freeze and Squeeze kit (Bio-Rad Laboratories). Typical conjugate concentrations were 100-300 nM. The final buffer of the AuNP-conjugates is presumed to be 0.5xTBE, with some residual BSPP and NaCl. There may also be some residue from the Freeze and Squeeze product and from the agarose gel. Functionalization - Carboxyl-Amino Method Procedure:

1. Bring the AuNPs to a 1xTAE buffer.
2. Add EDC at 10:1 EDC:DNA.
3. Add the amino-modified DNA strands.
4. Incubate for two hours.

DNA-Metallic structures and individual nanoparticles formation

The modified DNA templates were attached to previously RCA cleaned and oxygen plasma ashed (SPI Plasma Prep II, 20 min, 100 mA) silicon dioxide substrates (1 μm oxide, Silicon Quest) using 10x TAE/125 mM Mg^{2+} solution. The final DNA origami concentration was 250 pM. Functionalized gold nanoparticles (AuNPs) were attached onto the templates by adding 1 μL of a concentrated solution, to a final concentration of 3 nM and incubated for 15 min and rinsed in water for 5 seconds, followed by nitrogen blow. The structures were then enlarged in size using in-solution silver metallization as indicated by the manufacturer (HQ silver enhancement, Nanoprobes INC) for 12 min for the DNA-metallic structures and 10 min for the individual nanoparticles.

D.2 DNA Sequences

All DNA origami staple sequences and modified sequences were purchased from Integrated DNA Technologies, Inc. Except for the modified staples at the AuNP binding

sites, all staples sequences were the same as the original "tall rectangle" staples [104]. All side staples (columns +/-7) were left out.

DNA sequences used to functionalize AuNPs

The sequence conjugated to the AuNPs (ending in $X_{24,comp}$):

5'/5DTPA/ TTTTT GCGTTGGTGACTGCATTAGAGTCT 3' T5

sequence used for backfilling:

5' TTTTT /3ThioMC3-D/ 3'

D.2.1 Binding sites: DNA extensions to staples

A single AuNP-DNA conjugate binding site consists of two neighboring staples (or combinations of staples), each extended to have a 3-base spacer, followed by X_{24}, a 24-base sticky end complementary to the sequence of the conjugates.

Parallel Bars

Right side:

```
combining parts of t7r0f and t7r2f:
5'TGAAAGTATTAAGAGGCTATTATTCTGAAACA TTT  AGACTCTAATGCAGTCACCAACGC 3'
combining parts of t7r2f and t7r4f:
5'GTCAGACGATTGGCCTCAGGAGGTTGAGGCAG TTT  AGACTCTAATGCAGTCACCAACGC 3'
combining parts of t7r6f and t7r8f:
5'AGACAAAAGGGCGACAGGTTTACCAGCGCCAA TTT  AGACTCTAATGCAGTCACCAACGC 3'
combining parts of t7r8f and t7r10f:
5'GCAGATAGCCGAACAATTTTTAAGAAAAGTAA TTT  AGACTCTAATGCAGTCACCAACGC 3'
combining parts of t7r12f and t7r14:
5'GCTTATCCGGTATTCTAAATCAGATATAGAAG TTT  AGACTCTAATGCAGTCACCAACGC 3'
combining parts of t7r14f and t7r16f:
```

5’ACGCGCCTGTTTATCAGTTCAGCTAATGCAGA TTT AGACTCTAATGCAGTCACCAACGC 3’

combining parts of t7r18f and t7r20f:

5’CATAGGTCTGAGAGACGTGAATTTATCAAAAT TTT AGACTCTAATGCAGTCACCAACGC 3’

combining parts of t7r20f and t7r22f:

5’GAAGATGATGAAACAAAATTACCTGAGCAAAA TTT AGACTCTAATGCAGTCACCAACGC 3’

combining parts of t7r24f and t7r26f:

5’GCCGTCAATAGATAATCAACTAATAGATTAGA TTT AGACTCTAATGCAGTCACCAACGC 3’

combining parts of t7r26f and t7r28f:

5’CCAGCAGAAGATAAAAAATACCGAACGAACCA TTT AGACTCTAATGCAGTCACCAACGC 3’

The staple sequences on the left side were chosen similarly:

5’ ATAGGAACCCATGTACAGGGATAGCAAGCCCA TTT AGACTCTAATGCAGTCACCAACGC 3’

5’ TTTTTTCACGTTGAAAGAATTGCGAATAATAA TTT AGACTCTAATGCAGTCACCAACGC 3’

5’ AAATTGTGTCGAAATCTGTATCATCGCCTGAT TTT AGACTCTAATGCAGTCACCAACGC 3’

5’ CTTGCCCTGACGAGAACATTCAGTGAATAAGG TTT AGACTCTAATGCAGTCACCAACGC 3’

5’ CAGAAAACGAGAATGAAATGCTTTAAACAGTT TTT AGACTCTAATGCAGTCACCAACGC 3’

5’ GATGGCTTAGAGCTTAAGAGGTCATTTTTGCG TTT AGACTCTAATGCAGTCACCAACGC 3’

5’ ATTCAAAAGGGTGAGATAATGTGTAGGTAAAG TTT AGACTCTAATGCAGTCACCAACGC 3’

5’ CCCAAAAACAGGAAGATGATAATCAGAAAAGC TTT AGACTCTAATGCAGTCACCAACGC 3’

5’ GAAAGGGGGATGTGCTTATTACGCCAGCTGGC TTT AGACTCTAATGCAGTCACCAACGC 3’

5’ TGTAAAGCCTGGGGTGAGCCGGAAGCATAAAG TTT AGACTCTAATGCAGTCACCAACGC 3’

Ring

Left and right sequences were the same as those listed for the “parallel lines” assembly. The modified top staples were:

t-3r0g: 5’ CCCTCAGAACCGCCACCCT TTT AGACTCTAATGCAGTCACCAACGC 3’

t-3r2e: 5’ TGCTAAACTCCACAGACAGCCCTCTACCG TTT AGACTCTAATGCAGTCACCAACGC 3’

t3r0g: 5’ TGCTCAGTACCAGGCGGAT TTT AGACTCTAATGCAGTCACCAACGC 3’

t3r2e: 5’ GGAAAGCGGTAACAGTGCCCGTATCGGGG AAA AGACTCTAATGCAGTCACCAACGC 3’

The modified bottom staples were:

t-3r30f: 5’CCGAAATCAACGTCAAAGGGCGAAAAGGG TTT AGACTCTAATGCAGTCACCAACGC 3’

t-3r32h: 5’CCCCGATTTAGAGCTTGAC TTT AGACTCTAATGCAGTCACCAACGC 3’

t3r30f: 5’CGGCCTTGGTCTGTCCATCACGCATTGAC TTT AGACTCTAATGCAGTCACCAACGC 3’

t3r32h: 5’CACGTATAACGTGCTTTCC GTT AGACTCTAATGCAGTCACCAACGC 3’

H-shape

Left and right binding sites were the same as those listed for the “parallel lines” assembly. The central bar of the H had the following modified staples:

t1r12f: 5’TCTTACCAACCCAGCTACAATTTTAAAGAAGT TTT AGACTCTAATGCAGTCACCAACGC 3’

t-1r12f: 5’CCAAAATAAGGGGGTAATAGTAAAAAAAGATT TTT AGACTCTAATGCAGTCACCAACGC 3’

t-3r14e: 5’GAAGCAAAAAAGCGGATTGCATCAATGTTTAG TTT AGACTCTAATGCAGTCACCAACGC 3’

t-3r12f: 5’CATAACCCGCGTCCAATACTGCGGTATTATAG TTT AGACTCTAATGCAGTCACCAACGC 3’

t-5r14e: 5’TACCTTTAAGGTCTTTACCCTGACAATCGTCA TTT AGACTCTAATGCAGTCACCAACGC 3’

t-5r12f: 5’GGAATTACCATTGAATCCCCCTCACCATAAAT TTT AGACTCTAATGCAGTCACCAACGC 3’

t-1r14e: 5’TTTTAATTGCCCGAAAGACTTCAACAAGAACG TTT AGACTCTAATGCAGTCACCAACGC 3’

t1r14e: 5’ATCGGCTGACCAAGTACCGCACTCTTAGTTGC TTT AGACTCTAATGCAGTCACCAACGC 3’

t3r12f: 5’CCTAATTTAAGCCTTAAATCAAGAATCGAGAA TTT AGACTCTAATGCAGTCACCAACGC 3’

t3r14e: 5’CTAATTTACCGTTTTTATTTTCATCTTGCGGG TTT AGACTCTAATGCAGTCACCAACGC 3’

t5r12f: 5’ATTATTTATTAGCGAACCTCCCGACGTAGGAA TTT AGACTCTAATGCAGTCACCAACGC 3’

t5r14e: 5’TAAGTCCTGCGCCCAATAGCAAGCAAGAACGC TTT AGACTCTAATGCAGTCACCAACGC 3’

Bibliography

[1] G. P. Acuna, F. M. Möller, P. Holzmeister, S. Beater, B. Lalkens, and P. Tinnefeld. *Fluorescence enhancement at docking sites of DNA-directed self-assembled nanoantennas.* **Science**. **vol.** 338, **no.** 6106 (**2012**), pp. 506–10. DOI: 10.1126/science.1228638 (see p. 58).

[2] G. P. Acuna, M. Bucher, I. H. Stein, C. Steinhauer, A. Kuzyk, P. Holzmeister, R. Schreiber, A. Moroz, F. D. Stefani, T. Liedl, F. C. Simmel, and P. Tinnefeld. *Distance dependence of single-fluorophore quenching by gold nanoparticles studied on DNA origami.* **ACS Nano**. **vol.** 6, **no.** 4 (**2012**), pp. 3189–95. DOI: 10.1021/nn2050483 (see p. 58).

[3] A. V. Akimov, A. Mukherjee, C. L. Yu, D. E. Chang, a. S. Zibrov, P. R. Hemmer, H. Park, and M. D. Lukin. *Generation of single optical plasmons in metallic nanowires coupled to quantum dots.* **Nature**. **vol.** 450, **no.** 7168 (**2007**), pp. 402–6. DOI: 10.1038/nature06230 (see p. 2).

[4] A. P. Alivisatos, K. P. Johnsson, X. Peng, T. E. Wilson, C. J. Loweth, M. P. Bruchez, and P. G. Schultz. *Organization of 'nanocrystal molecules' using DNA.* **Nature**. **vol.** 382, **no.** 6592 (**1996**), pp. 609–11. DOI: 10.1038/382609a0 (see p. 28).

[5] E. S. Andersen, M. Dong, M. M. Nielsen, K. Jahn, R. Subramani, W. Mamdouh, M. M. Golas, B. Sander, H. Stark, C. L. P. Oliveira, J. S. Pedersen, V. Birkedal, F. Besenbacher, K. V. Gothelf, and J. r. Kjems. *Self-assembly of a nanoscale DNA box with a controllable lid.* **Nature**. **vol.** 459, **no.** 7243 (**2009**), pp. 73–6. DOI: 10.1038/nature07971 (see pp. 12, 14).

[6] P. Anger, P. Bharadwaj, and L. Novotny. *Enhancement and Quenching of Single-Molecule Fluorescence.* **Phys. Rev. Lett. vol.** 96, **no.** 11 (**2006**), p. 113002. DOI: 10.1103/PhysRevLett.96.113002 (see pp. 54, 55).

[7] J. N. Anker, W. P. Hall, O. Lyandres, N. C. Shah, J. Zhao, and R. P. Van Duyne. *Biosensing with plasmonic nanosensors.* **Nat. Mater. vol.** 7, **no.** 6 (**2008**), pp. 442–53. DOI: 10.1038/nmat2162 (see p. 2).

[8] J.-M. Arbona, J.-P. Aimé, and J. Elezgaray. *Cooperativity in the annealing of DNA origamis.* **J. Chem. Phys. vol.** 138, **no.** 1 (**2013**), p. 015105. DOI: 10.1063/1.4773405 (see p. 15).

[9] C. Ayala-Orozco, C. Urban, M. W. Knight, A. S. Urban, O. Neumann, S. W. Bishnoi, S. Mukherjee, A. M. Goodman, H. Charron, T. Mitchell, M. Shea, R. Roy, S. Nanda, R. Schiff, N. J. Halas, and A. Joshi. *Au Nanomatryoshkas as Efficient Near-Infrared Photothermal Transducers for Cancer Treatment: Benchmarking against Nanoshells.* **ACS Nano**. **vol.** 8, **no.** 6 (**2014**), pp. 6372–81. DOI: 10.1021/nn501871d (see p. 2).

[10] W. L. Barnes, A. Dereux, and T. W. Ebbesen. *Surface plasmon subwavelength optics.* **Nature**. **vol.** 424, **no.** 6950 (**2003**). Ed. by J. Servaes, pp. 824–830 (see p. 36).

[11] S. Benabou, A. Aviñó, R. Eritja, C. Gonzalez, and R. Gargallo. *Fundamental aspects of the nucleic acid i-motif structures.* **RSC Adv.** (**2014**). DOI: 10.1039/c4ra02129k (see p. 5).

[12] M. L. Bochman, K. Paeschke, and V. a. Zakian. *DNA secondary structures: stability and function of G-quadruplex structures.* **Nat. Rev. Genet. vol.** 13, **no.** 11 (**2012**), pp. 770–80. DOI: 10.1038/nrg3296 (see p. 5).

[13] C. Bohren and D. Huffman. *Absorption and scattering of light by small particles.* **2008** (see pp. 42, 73).

[14] G. W. Bryant and M. Pelton. *Introduction to metal-nanoparticle plasmonics.* **2014** (see p. 73).

[15] H. Bui, C. Onodera, C. Kidwell, Y. Tan, E. Graugnard, W. Kuang, J. Lee, W. B. Knowlton, B. Yurke, and W. L. Hughes. *Programmable periodicity of quantum dot arrays with DNA origami nanotubes.* **Nano Lett. vol.** 10, **no.** 9 (**2010**), pp. 3367–72. DOI: 10.1021/nl101079u (see p. 16).

[16] Y. C. Cao, R. Jin, and C. a. Mirkin. *Nanoparticles with Raman spectroscopic fingerprints for DNA and RNA detection.* **Science**. **vol.** 297, **no.** 5586 (**2002**), pp. 1536–40. DOI: 10.1126/science.297.5586.1536 (see p. 58).

[17] C. Cohen-Tannoudji, B. Diu, and F. Laole. *Quantum Mechanics* (see p. 52).

[18] *COMSOL Multiphysics*. UK, **2013** (see pp. 38, 43, 47).

[19] T. Dauxois. *Dynamics of breather modes in a nonlinear helicoidal model of DNA*. **Phys. Lett. A**. **vol.** 159, **no.** 8-9 (**1991**), pp. 390–395. DOI: 10.1016/0375-9601(91)90367-H (see p. 7).

[20] *DDSCAT*. **2013** (see p. 47).

[21] B. Ding, Z. Deng, H. Yan, S. Cabrini, R. N. Zuckermann, and J. Bokor. *Gold nanoparticle self-similar chain structure organized by DNA origami.* **J. Am. Chem. Soc. vol.** 132, **no.** 10 (**2010**), pp. 3248–9. DOI: 10.1021/ja9101198 (see p. 16).

[22] R. M. Dirks and N. a. Pierce. *Triggered amplification by hybridization chain reaction.* **Proc. Natl. Acad. Sci. U. S. A. vol.** 101, **no.** 43 (**2004**), pp. 15275–8. DOI: 10.1073/pnas.0407024101 (see pp. 15, 16).

[23] S. M. Douglas, H. Dietz, T. Liedl, B. Högberg, F. Graf, and W. M. Shih. *Self-assembly of DNA into nanoscale three-dimensional shapes.* **Nature**. **vol.** 459, **no.** 7245 (**2009**), pp. 414–418. DOI: 10.1038/nature08016 (see p. 14).

[24] S. M. Douglas, A. H. Marblestone, S. Teerapittayanon, A. Vazquez, G. M. Church, and W. M. Shih. *Rapid prototyping of 3D DNA-origami shapes with caDNAno.* **Nucleic Acids Res. vol.** 37, **no.** 15 (**2009**), pp. 5001–6. DOI: 10.1093/nar/gkp436 (see p. 14).

[25] J. P. K. Doye, T. E. Ouldridge, A. a. Louis, F. Romano, P. Šulc, C. Matek, B. E. K. Snodin, L. Rovigatti, J. S. Schreck, R. M. Harrison, and W. P. J. Smith. *Coarse-graining DNA for simulations of DNA nanotechnology.* **Phys. Chem. Chem. Phys. vol.** 15, **no.** 47 (**2013**), pp. 20395–414. DOI: 10.1039/c3cp53545b (see p. 8).

[26] B. T. Draine and P. J. Flatau. *Discrete-dipole approximation for scattering calculations.* **J. Opt. Soc. Am. A**. **vol.** 11, **no.** 4 (**1994**), p. 1491. DOI: 10.1364/JOSAA.11.001491 (see p. 47).

[27] G. Dressel. *Electrodynamics of solids.* **2002** (see p. 40).

[28] P. G. Etchegoin, E. C. Le Ru, R. C. Maher, and L. F. Cohen. *Enhancement factor averaging and the photostability of probes in SERS vibrational pumping.* **Phys. Chem. Chem. Phys. vol.** 9, **no.** 35 (**2007**), pp. 4923–9. DOI: 10.1039/b706395d (see p. 64).

[29] P. G. Etchegoin, M. Meyer, and E. C. L. Ru. *Statistics of single molecule SERS signals : is there a Poisson distribution of intensities ?* (**2007**), pp. 3006–3010. DOI: 10.1039/b704013j (see p. 64).

[30] J. a. Fan, K. Bao, C. Wu, J. Bao, R. Bardhan, N. J. Halas, V. N. Manoharan, G. Shvets, P. Nordlander, and F. Capasso. *Fano-like interference in self-assembled plasmonic quadrumer clusters.* **Nano Lett. vol.** 10, **no.** 11 (**2010**), pp. 4680–4685. DOI: 10.1021/nl1029732 (see p. 47).

[31] J. A. Fan, C. Wu, K. Bao, J. Bao, R. Bardhan, N. J. Halas, V. N. Manoharan, P. Nordlander, G. Shvets, and F. Capasso. *Self-assembled plasmonic nanoparticle clusters.* **Science**. **vol.** 328, **no.** 5982 (**2010**), pp. 1135–8. DOI: 10.1126/science.1187949 (see p. 47).

[32] Z. Fan and A. O. Govorov. *Plasmonic circular dichroism of chiral metal nanoparticle assemblies.* **Nano Lett. vol.** 10, **no.** 7 (**2010**), pp. 2580–7. DOI: 10.1021/nl101231b (see p. 1).

[33] Y. Fang, N. Seong, and D. Dlott. *Measurement of the distribution of site enhancements in surface-enhanced Raman scattering.* **Science (80-.). no.** December (**2008**), pp. 388–393 (see pp. 64, 65).

[34] N. T. Fofang, N. K. Grady, Z. Fan, A. O. Govorov, and N. J. Halas. *Plexciton dynamics: exciton-plasmon coupling in a J-aggregate-Au nanoshell complex provides a mechanism for nonlinearity.* **Nano Lett. vol.** 11, **no.** 4 (**2011**), pp. 1556–60. DOI: 10.1021/nl104352j (see p. 1).

[35] M. D. Frank-Kamenetskii and S. Prakash. *Fluctuations in the DNA double helix: A critical review.* **Phys. Life Rev. vol.** 1 (**2014**), pp. 1–18. DOI: 10.1016/j.plrev.2014.01.005 (see p. 7).

[36] T. J. Fu and N. C. Seeman. *DNA double-crossover molecules.* **Biochemistry**. **vol.** 32, **no.** 13 (**1993**), pp. 3211–20 (see pp. 12, 13).

[37] D. Graham, D. G. Thompson, W. E. Smith, and K. Faulds. *Control of enhanced Raman scattering using a DNA-based assembly process of dye-coded nanoparticles.* **Nat. Nanotechnol. vol.** 3, **no.** 9 (**2008**), pp. 548–51. DOI: 10.1038/nnano.2008.189 (see p. 58).

[38] H. Gu, J. Chao, S.-J. Xiao, and N. C. Seeman. *A proximity-based programmable DNA nanoscale assembly line.* **Nature**. **vol.** 465, **no.** 7295 (**2010**), pp. 202–205. DOI: 10.1038/nature09026 (see p. 16).

[39] Q. Gu and D. Haynie. *DNA-templated nanowires: Context, fabrication, properties and applications.* **Annu. Rev. Nano Res.** (**2008**). DOI: 10.1142/9789812790248_0005 (see p. 16).

[40] H. Haken and H. C. Wolf. *Molecular Physics and Elements of Quantum Chemistry.* **vol.** 397. Advanced Texts in Physics. Berlin, Heidelberg: Springer Berlin Heidelberg, **2004**, p. 595. DOI: 10.1007/978-3-662-08820-3 (see p. 52).

[41] L. R. Hirsch, R. J. Stafford, J. a. Bankson, S. R. Sershen, B. Rivera, R. E. Price, J. D. Hazle, N. J. Halas, and J. L. West. *Nanoshell-mediated near-infrared thermal therapy of tumors under magnetic resonance guidance.* **Proc. Natl. Acad. Sci. U. S. A. vol.** 100, **no.** 23 (**2003**), pp. 13549–54. DOI: 10.1073/pnas.2232479100 (see p. 2).

[42] U. Hohenester and A. Trügler. *MNPBEM A Matlab toolbox for the simulation of plasmonic nanoparticles.* **Comput. Phys. Commun. vol.** 183, **no.** 2 (**2012**), pp. 370–381. DOI: 10.1016/j.cpc.2011.09.009 (see p. 47).

[43] A. M. Hung, C. M. Micheel, L. D. Bozano, L. W. Osterbur, G. M. Wallraff, and J. N. Cha. *Large-area spatially ordered arrays of gold nanoparticles directed by lithographically confined DNA origami.* **Nat. Nanotechnol. vol.** 5, **no.** 2 (**2010**), pp. 121–6. DOI: 10.1038/nnano.2009.450 (see pp. 16, 19, 20).

[44] A. M. Hung, H. Noh, and J. N. Cha. *Recent advances in DNA-based directed assembly on surfaces.* **Nanoscale**. (**2010**), pp. 2530–2537. DOI: 10.1039/c0nr00430h (see pp. 15, 68).

[45] S. J. Hurst, A. K. R. Lytton-Jean, and C. a. Mirkin. *Maximizing DNA loading on a range of gold nanoparticle sizes.* **Anal. Chem. vol.** 78, **no.** 24 (**2006**), pp. 8313–8. DOI: 10.1021/ac0613582 (see pp. 32, 33).

[46] J. Jackson. *Classical electrodynamics*. 3rd. **1998** (see pp. 41, 70).

[47] P. B. Johnson and R. W. Christy. *Optical Constants of the Noble Metals*. **Phys. Rev. B**. **vol.** 6, **no.** 12 (**1972**), pp. 4370–4379. DOI: 10.1103/PhysRevB.6.4370 (see p. 75).

[48] W. G. Jr and W. Grandy. *Scattering of waves from large spheres*. **2005** (see pp. 41, 42, 73).

[49] a. V. Kabashin, P. Evans, S. Pastkovsky, W. Hendren, G. a. Wurtz, R. Atkinson, R. Pollard, V. a. Podolskiy, and a. V. Zayats. *Plasmonic nanorod metamaterials for biosensing*. **Nat. Mater. vol.** 8, **no.** 11 (**2009**), pp. 867–71. DOI: 10.1038/nmat2546 (see p. 2).

[50] N. R. Kallenbach, R.-I. Ma, and N. C. Seeman. *An immobile nucleic acid junction constructed from oligonucleotides*. **Nature**. **vol.** 305, **no.** 5937 (**1983**), pp. 829–831. DOI: 10.1038/305829a0 (see pp. 12, 13).

[51] Y. Ke, L. L. Ong, W. M. Shih, and P. Yin. *Three-dimensional structures self-assembled from DNA bricks*. **Science**. **vol.** 338, **no.** 6111 (**2012**), pp. 1177–83. DOI: 10.1126/science.1227268 (see p. 15).

[52] Y. Ke, J. Sharma, M. Liu, K. Jahn, Y. Liu, and H. Yan. *Scaffolded DNA origami of a DNA tetrahedron molecular container*. **Nano Lett. vol.** 9, **no.** 6 (**2009**), pp. 2445–7. DOI: 10.1021/nl901165f (see p. 14).

[53] K. Keren, M. Krueger, R. Gilad, G. Ben-Yoseph, U. Sivan, and E. Braun. *Sequence-specific molecular lithography on single DNA molecules*. **Science**. **vol.** 297, **no.** 5578 (**2002**), pp. 72–5. DOI: 10.1126/science.1071247 (see p. 16).

[54] R. J. Kershner, L. D. Bozano, C. M. Micheel, A. M. Hung, A. R. Fornof, J. N. Cha, C. T. Rettner, M. Bersani, J. Frommer, P. W. K. Rothemund, and G. M. Wallraff. *Placement and orientation of individual DNA shapes on lithographically patterned surfaces*. **Nat. Nanotechnol. vol.** 4, **no.** 9 (**2009**), pp. 557–61. DOI: 10.1038/nnano.2009.220 (see pp. 15, 19).

[55] K. Kim, K. L. Kim, D. Shin, J.-Y. Choi, and K. S. Shin. *Surface-Enhanced Raman Scattering of 4-Aminobenzenethiol on Ag and Au: pH Dependence of b 2 -Type Bands*. **J. Phys. Chem. C**. **vol.** 116, **no.** 7 (**2012**), pp. 4774–4779. DOI: 10.1021/jp211730r (see p. 63).

[56] K. Kim, H. B. Lee, D. Shin, H. Ryoo, J. W. Lee, and K. S. Shin. *Surface-enhanced Raman scattering of 4-aminobenzenethiol on silver: confirmation of the origin of b2-type bands*. **J. Raman Spectrosc. vol.** 42, **no.** 12 (**2011**), pp. 2112–2118. DOI: 10.1002/jrs.2972 (see p. 63).

[57] C. Kittel. *Phase Transition of a Molecular Zipper*. **Am. J. Phys. vol.** 37, **no.** 9 (**1969**), p. 917. DOI: 10.1119/1.1975930 (see pp. 4, 6, 8, 9).

[58] S. L. Kleinman, J. M. Bingham, A.-i. Henry, K. L. Wustholz, and R. P. Van Duyne. *Structural and optical characterization of single nanoparticles and single molecule SERS*. Ed. by M. I. Stockman. **vol.** 7757. **2010**, 77570J–77570J–10. DOI: 10.1117/12.864654 (see p. 51).

[59] K. Kneipp, Y. Wang, H. Kneipp, L. Perelman, I. Itzkan, R. Dasari, and M. Feld. *Single Molecule Detection Using Surface-Enhanced Raman Scattering (SERS)*. **Phys. Rev. Lett. vol.** 78, **no.** 9 (**1997**), pp. 1667–1670. DOI: 10.1103/PhysRevLett.78.1667 (see p. 56).

[60] S. H. Ko, K. Du, and J. A. Liddle. *Quantum-dot fluorescence lifetime engineering with DNA origami constructs*. **Angew. Chem. Int. Ed. Engl. vol.** 52, **no.** 4 (**2013**), pp. 1193–7. DOI: 10.1002/anie.201206253 (see p. 58).

[61] H. Kuwata, H. Tamaru, K. Esumi, and K. Miyano. *Resonant light scattering from metal nanoparticles: Practical analysis beyond Rayleigh approximation*. **Appl. Phys. Lett. vol.** 83, **no.** 22 (**2003**), p. 4625. DOI: 10.1063/1.1630351 (see p. 43).

[62] A. Kuzyk, R. Schreiber, Z. Fan, G. Pardatscher, E.-M. Roller, A. Högele, F. C. Simmel, A. O. Govorov, T. Liedl, and E. Maria. *DNA-based self-assembly of chiral plasmonic nanostructures with tailored optical response*. **Nature**. **vol.** 483, **no.** 7389 (**2012**), pp. 311–4. DOI: 10.1038/nature10889 (see pp. 18, 58).

[63] J. B. Lassiter, H. Sobhani, J. a. Fan, J. Kundu, F. Capasso, P. Nordlander, and N. J. Halas. *Fano resonances in plasmonic nanoclusters: geometrical and chemical tunability*. **Nano Lett. vol.** 10, **no.** 8 (**2010**), pp. 3184–3189. DOI: 10.1021/nl102108u (see p. 47).

[64] D.-K. Lim, K.-S. Jeon, J.-H. Hwang, H. Kim, S. Kwon, Y. D. Suh, and J.-M. Nam. *Highly uniform and reproducible surface-enhanced Raman scattering from DNA-tailorable nanoparticles with 1-nm interior gap*. **Nat. Nanotechnol. vol.** 6, **no.** 7 (**2011**), pp. 452–60. DOI: 10.1038/nnano.2011.79 (see p. 58).

[65] D.-K. Lim, K.-S. Jeon, H. M. Kim, J.-M. Nam, and Y. D. Suh. *Nanogap-engineerable Raman-active nanodumbbells for single-molecule detection*. **Nat. Mater. vol.** 9, **no.** 1 (**2010**), pp. 60–7. DOI: 10.1038/nmat2596 (see p. 58).

[66] J. Liu, Y. Geng, E. Pound, S. Gyawali, J. R. Ashton, J. Hickey, A. T. Woolley, and J. N. Harb. *Metallization of Branched DNA Origami for Nanoelectronic Circuit Fabrication*, **no.** 3 (**2011**), pp. 2240–2247 (see p. 17).

[67] Q. Liu, C. Song, Z.-G. Wang, N. Li, and B. Ding. *Precise organization of metal nanoparticles on DNA origami template*. **Methods**. (**2013**). DOI: 10.1016/j.ymeth.2013.10.006 (see pp. 16, 27).

[68] D. a. Long. *The Raman Effect*. Chichester, UK: John Wiley & Sons, Ltd, **2002**. DOI: 10.1002/0470845767 (see p. 53).

[69] C. J. Loweth, W. B. Caldwell, X. Peng, A. P. Alivisatos, and P. G. Schultz. *DNA-Based Assembly of Gold Nanocrystals ***. **vol.** 5, **no.** 12 (**1999**), pp. 1808–1812 (see pp. 18, 60, 81).

[70] K. Lund, A. J. Manzo, N. Dabby, N. Michelotti, A. Johnson-Buck, J. Nangreave, S. Taylor, R. Pei, M. N. Stojanovic, N. G. Walter, E. Winfree, and H. Yan. *Molecular robots guided by prescriptive landscapes.* **Nature**. **vol.** 465, **no.** 7295 (**2010**), pp. 206–10. DOI: 10.1038/nature09012 (see p. 16).

[71] S. Maier. *Plasmonics: Fundamentals and Applications*. Ed. by. Fernandez-Nieves, H. M. Wyss, J. Mattsson, and D. A. Weitz. **vol.** 76. Chemistry and Materials Science. Springer, **2007**, p. 248 (see pp. 35–37, 43, 79).

[72] S. a. Maier, P. G. Kik, H. a. Atwater, S. Meltzer, E. Harel, B. E. Koel, and A. a. G. Requicha. *Local detection of electromagnetic energy transport below the diffraction limit in metal nanoparticle plasmon waveguides.* **Nat. Mater. vol.** 2, **no.** 4 (**2003**), pp. 229–32. DOI: 10.1038/nmat852 (see p. 36).

[73] A. N. Marchi, I. Saaem, B. N. Vogen, S. Brown, and T. H. LaBean. *Towards larger DNA origami*. **submitted**. (**2014**) (see pp. 15, 69).

[74] D. C. Marinica, a. K. Kazansky, P. Nordlander, J. Aizpurua, and a. G. Borisov. *Quantum plasmonics: nonlinear effects in the field enhancement of a plasmonic nanoparticle dimer.* **Nano Lett. vol.** 12, **no.** 3 (**2012**), pp. 1333–9. DOI: 10.1021/nl300269c (see p. 35).

[75] A. J. Mastroianni, S. a. Claridge, and a. P. Alivisatos. *Pyramidal and chiral groupings of gold nanocrystals assembled using DNA scaffolds.* **J. Am. Chem. Soc. vol.** 131, **no.** 24 (**2009**), pp. 8455–9. DOI: 10.1021/ja808570g (see p. 27).

[76] C. Mätzler. *MATLAB functions for Mie scattering and absorption*. Bern, Switzerland, **2002** (see p. 42).

[77] H. T. Maune, S.-P. Han, R. D. Barish, M. Bockrath, W. a. G. Iii, P. W. K. Rothemund, and E. Winfree. *Self-assembly of carbon nanotubes into two-dimensional geometries using DNA origami templates.* **Nat. Nanotechnol. vol.** 5, **no.** 1 (**2010**), pp. 61–6. DOI: 10.1038/nnano.2009.311 (see p. 16).

[78] G. Mie. *Beiträge zur Optik trüber Medien, speziell kolloidaler Metallösungen.* **Ann. Phys. vol.** 330, **no.** 3 (**1908**), pp. 377–445. DOI: 10.1002/andp.19083300302 (see p. 40).

[79] C. A. Mirkin, R. L. Letsinger, R. C. Mucic, and J. J. Storhoff. *A DNA-based method for rationally assembling nanoparticles into macroscopic materials.* **Nature**. **vol.** 382, **no.** 6592 (**1996**), pp. 607–9. DOI: 10.1038/382607a0 (see p. 28).

[80] A. E. Miroshnichenko, S. Flach, and Y. S. Kivshar. *Fano resonances in nanoscale structures*. **vol.** 82, **no.** September (**2010**), pp. 2257–2298. DOI: 10.1103/RevModPhys.82.2257. arXiv: 0902.3014 (see p. 47).

[81] J. J. Mock, M. Barbic, D. R. Smith, D. a. Schultz, and S. Schultz. *Shape effects in plasmon resonance of individual colloidal silver nanoparticles*. **J. Chem. Phys. vol.** 116, **no.** 15 (**2002**), p. 6755. DOI: 10.1063/1.1462610 (see pp. 47, 49).

[82] S. Neidle. *Principles of nucleic acid structure*. Elsevier, **2008** (see p. 5).

[83] W. G. Noid. *Perspective: Coarse-grained models for biomolecular systems*. **J. Chem. Phys. vol.** 139, **no.** 9 (**2013**), p. 090901. DOI: 10.1063/1.4818908 (see p. 8).

[84] P. Nordlander, C. Oubre, E. Prodan, K. Li, and M. I. Stockman. *Plasmon Hybridization in Nanoparticle Dimers*. **Nano Lett. vol.** 4, **no.** 5 (**2004**), pp. 899–903. DOI: 10.1021/nl049681c (see pp. 45, 73).

[85] T. E. Ouldridge, A. a. Louis, and J. P. K. Doye. *DNA Nanotweezers Studied with a Coarse-Grained Model of DNA*. **Phys. Rev. Lett. vol.** 104, **no.** 17 (**2010**), p. 178101. DOI: 10.1103/PhysRevLett.104.178101 (see p. 8).

[86] S. Pal, Z. Deng, B. Ding, H. Yan, and Y. Liu. *DNA-origami-directed self-assembly of discrete silver-nanoparticle architectures*. **Angew. Chem. Int. Ed. Engl. vol.** 49, **no.** 15 (**2010**), pp. 2700–4. DOI: 10.1002/anie.201000330 (see p. 16).

[87] S. Pal, Z. Deng, H. Wang, S. Zou, Y. Liu, and H. Yan. *DNA directed self-assembly of anisotropic plasmonic nanostructures*. **J. Am. Chem. Soc. vol.** 133, **no.** 44 (**2011**), pp. 17606–9. DOI: 10.1021/ja207898r (see pp. 16, 58).

[88] S.-J. Park, T. A. Taton, and C. a. Mirkin. *Array-based electrical detection of DNA with nanoparticle probes*. **Science**. **vol.** 295, **no.** 5559 (**2002**), pp. 1503–6. DOI: 10.1126/science.1067003 (see p. 17).

[89] S. H. Park, R. Barish, H. Li, J. H. Reif, G. Finkelstein, H. Yan, and T. H. Labean. *Three-helix bundle DNA tiles self-assemble into 2D lattice or 1D templates for silver nanowires*. **Nano Lett. vol.** 5, **no.** 4 (**2005**), pp. 693–6. DOI: 10.1021/nl050108i (see p. 17).

[90] S. H. Park, M. W. Prior, T. H. LaBean, and G. Finkelstein. *Optimized fabrication and electrical analysis of silver nanowires templated on DNA molecules*. **Appl. Phys. Lett. vol.** 89, **no.** 3 (**2006**), p. 033901. DOI: 10.1063/1.2234282 (see pp. 21, 60).

[91] S. H. Park, H. Yan, J. H. Reif, T. H. LaBean, and G. Finkelstein. *Electronic nanostructures templated on self-assembled DNA scaffolds*. **Nanotechnology**. **vol.** 15, **no.** 10 (**2004**), S525–S527. DOI: 10.1088/0957-4484/15/10/005 (see p. 17).

[92] A. Pérez, F. J. Luque, and M. Orozco. *Frontiers in molecular dynamics simulations of DNA*. **Acc. Chem. Res. vol.** 45, **no.** 2 (**2012**), pp. 196–205. DOI: 10.1021/ar2001217 (see p. 7).

[93] M. Peyrard and A. Bishop. *Statistical mechanics of a nonlinear model for DNA denaturation.* **Phys. Rev. Lett. vol.** 62, **no.** 23 (**1989**), pp. 2755–2758. DOI: 10.1103/PhysRevLett.62.2755 (see pp. 4, 6).

[94] M. Peyrard, S. Cuesta-López, and G. James. *Nonlinear analysis of the dynamics of DNA breathing.* **J. Biol. Phys. vol.** 35, **no.** 1 (**2009**), pp. 73–89. DOI: 10.1007/s10867-009-9127-2 (see p. 7).

[95] M. Peyrard and T. Dauxois. *Can we model DNA at the mesoscale?: Comment on "Fluctuations in the DNA double helix: A critical review" by Frank-Kamenetskii and Prakash.* **Phys. Life Rev. vol.** 1 (**2014**), pp. 10–12. DOI: 10.1016/j.plrev.2014.03.008 (see p. 7).

[96] M. Pilo-Pais, S. Goldberg, E. Samano, T. H. Labean, and G. Finkelstein. *Connecting the nanodots: programmable nanofabrication of fused metal shapes on DNA templates.* **Nano Lett. vol.** 11, **no.** 8 (**2011**), pp. 3489–3492. DOI: 10.1021/nl202066c (see pp. 1, 4, 16, 58–60, 100).

[97] M. Pilo-Pais, A. Watson, S. Demers, T. H. LaBean, and G. Finkelstein. *Surface-enhanced Raman scattering plasmonic enhancement using DNA origami-based complex metallic nanostructures.* **Nano Lett. vol.** 14, **no.** 4 (**2014**), pp. 2099–104. DOI: 10.1021/nl5003069 (see pp. 1, 100).

[98] J. M. Pitarke, V. M. Silkin, E. V. Chulkov, and P. M. Echenique. *Theory of surface plasmons and surface-plasmon polaritons.* **Reports Prog. Phys. vol.** 70, **no.** 1 (**2007**), pp. 1–87. DOI: 10.1088/0034-4885/70/1/R01 (see p. 36).

[99] D. Poland. *Occurrence of a Phase Transition in Nucleic Acid Models.* **J. Chem. Phys. vol.** 45, **no.** 5 (**1966**), p. 1464. DOI: 10.1063/1.1727786 (see pp. 4, 6, 9, 10).

[100] E. Prodan and P. Nordlander. *Plasmon hybridization in spherical nanoparticles.* **J. Chem. Phys. vol.** 120, **no.** 11 (**2004**), pp. 5444–54. DOI: 10.1063/1.1647518 (see pp. 45, 73).

[101] E. Prodan, C. Radloff, N. J. Halas, and P. Nordlander. *A hybridization model for the plasmon response of complex nanostructures.* **Science. vol.** 302, **no.** 5644 (**2003**), pp. 419–22. DOI: 10.1126/science.1089171 (see pp. 1, 45).

[102] C. V. Raman and K. S. Krishnan. *A New Type of Secondary Radiation.* **Nature. vol.** 121, **no.** 3048 (**1928**), pp. 501–502. DOI: 10.1038/121501c0 (see p. 50).

[103] J. M. Romo-Herrera, R. a. Alvarez-Puebla, and L. M. Liz-Marzán. *Controlled assembly of plasmonic colloidal nanoparticle clusters.* **Nanoscale. vol.** 3, **no.** 4 (**2011**), pp. 1304–15. DOI: 10.1039/c0nr00804d (see p. 58).

[104] P. W. K. Rothemund. *Folding DNA to create nanoscale shapes and patterns.* **Nature. vol.** 440, **no.** 7082 (**2006**), pp. 297–302. DOI: 10.1038/nature04586 (see pp. 1, 13–15, 17, 83).

[105] E. L. Ru and P. Etchegoin. *Principles of Surface-Enhanced Raman Spectroscopy: and related plasmonic effects*. First. Elsevier B.V., **2009** (see pp. 51, 56, 62, 64).

[106] E. C. Samano, M. Pilo-Pais, S. Goldberg, B. N. Vogen, G. Finkelstein, and T. H. LaBean. *Self-assembling DNA templates for programmed artificial biomineralization*. **Soft Matter**. **vol.** 7, **no.** 7 (**2011**), p. 3240. DOI: 10.1039/c0sm01318h (see p. 100).

[107] A. W. Sanders, D. a. Routenberg, B. J. Wiley, Y. Xia, E. R. Dufresne, and M. a. Reed. *Observation of plasmon propagation, redirection, and fan-out in silver nanowires.* **Nano Lett. vol.** 6, **no.** 8 (**2006**), pp. 1822–6. DOI: 10.1021/nl052471v (see p. 2).

[108] J. SantaLucia. *A unified view of polymer, dumbbell, and oligonucleotide DNA nearest-neighbor thermodynamics.* **Proc. Natl. Acad. Sci. U. S. A. vol.** 95, **no.** 4 (**1998**), pp. 1460–5 (see pp. 4, 10, 11).

[109] J. SantaLucia and D. Hicks. *The thermodynamics of DNA structural motifs.* **Annu. Rev. Biophys. Biomol. Struct. vol.** 33 (**2004**), pp. 415–40. DOI: 10.1146/annurev.biophys.32.110601.141800 (see p. 11).

[110] J. Schäfer. *MatScat* (see p. 42).

[111] A. E. Schlather, N. Large, A. S. Urban, P. Nordlander, and N. J. Halas. *Near-field mediated plexcitonic coupling and giant rabi splitting in individual metallic dimers.* **Nano Lett. vol.** 13, **no.** 7 (**2013**), pp. 3281–6. DOI: 10.1021/nl4014887 (see p. 1).

[112] R. Schreiber, J. Do, E.-M. Roller, T. Zhang, V. J. Schüller, P. C. Nickels, J. Feldmann, and T. Liedl. *Hierarchical assembly of metal nanoparticles, quantum dots and organic dyes using DNA origami scaffolds.* **Nat. Nanotechnol. vol.** 9, **no.** 1 (**2014**), pp. 74–8. DOI: 10.1038/nnano.2013.253 (see p. 18).

[113] R. Schreiber, S. Kempter, S. Holler, V. Schüller, D. Schiffels, S. S. Simmel, P. C. Nickels, and T. Liedl. *DNA Origami-Templated Growth of Arbitrarily Shaped Metal Nanoparticles.* **Small**. **no.** c (**2011**), pp. 1795–1799. DOI: 10.1002/smll.201100465 (see pp. 17, 58).

[114] N. C. Seeman. *Nanomaterials based on DNA.* **Annu. Rev. Biochem. vol.** 79 (**2010**), pp. 65–87. DOI: 10.1146/annurev-biochem-060308-102244 (see p. 12).

[115] N. C. Seeman. *Nucleic acid junctions and lattices.* **J. Theor. Biol. vol.** 99, **no.** 2 (**1982**), pp. 237–247. DOI: 10.1016/0022-5193(82)90002-9 (see pp. 1, 12, 13, 69).

[116] F. Shafiei, F. Monticone, K. Q. Le, X.-X. Liu, T. Hartsfield, A. Alù, and X. Li. *A subwavelength plasmonic metamolecule exhibiting magnetic-based optical Fano resonance.* **Nat. Nanotechnol. vol.** 8, **no.** 2 (**2013**), pp. 95–9. DOI: 10.1038/nnano.2012.249 (see p. 60).

[117] J. Sharma, R. Chhabra, Y. Liu, Y. Ke, and H. Yan. *DNA-templated self-assembly of two-dimensional and periodical gold nanoparticle arrays.* **Angew. Chem. Int. Ed. Engl. vol.** 45, **no.** 5 (**2006**), pp. 730–5. DOI: 10.1002/anie.200503208 (see p. 21).

[118] S. Sheikholeslami, Y.-W. Jun, P. K. Jain, and A. P. Alivisatos. *Coupling of optical resonances in a compositionally asymmetric plasmonic nanoparticle dimer.* **Nano Lett. vol.** 10, **no.** 7 (**2010**), pp. 2655–60. DOI: 10.1021/nl101380f (see pp. 47, 48).

[119] W. M. Shih, J. D. Quispe, and G. F. Joyce. *A 1.7-kilobase single-stranded DNA that folds into a nanoscale octahedron.* **Nature**. **vol.** 427, **no.** 6975 (**2004**), pp. 618–21. DOI: 10.1038/nature02307 (see pp. 13, 14).

[120] D. Solis, B. Willingham, S. L. Nauert, L. S. Slaughter, J. Olson, P. Swanglap, A. Paul, W.-s. Chang, and S. Link. *Electromagnetic energy transport in nanoparticle chains via dark plasmon modes.* **Nano Lett. vol.** 12, **no.** 3 (**2012**), pp. 1349–53. DOI: 10.1021/nl2039327 (see p. 36).

[121] D. U. Soudamini, C. Y. Fu, K. W. Kho, P. Thoniyot, A. Agarwal, and M. Olivo. *Fluctuation in Surface Enhanced Raman Scattering intensity due to plasmon related heating effect.* **Proc SPIE**. **vol.** 7394 (**2009**). Ed. by M. I. Stockman, 73940T–73940T–9. DOI: 10.1117/12.827234 (see p. 64).

[122] C. Steinhauer, R. Jungmann, T. L. Sobey, F. C. Simmel, and P. Tinnefeld. *DNA origami as a nanoscopic ruler for super-resolution microscopy.* **Angew. Chem. Int. Ed. Engl. vol.** 48, **no.** 47 (**2009**), pp. 8870–3. DOI: 10.1002/anie.200903308 (see p. 16).

[123] J. Stratton. *Electromagnetic theory.* **1941** (see pp. 42, 73).

[124] J. Takahara, S. Yamagishi, H. Taki, a. Morimoto, and T. Kobayashi. *Guiding of a one-dimensional optical beam with nanometer diameter.* **Opt. Lett. vol.** 22, **no.** 7 (**1997**), pp. 475–7 (see p. 36).

[125] N. Theodorakopoulos. *Melting of genomic DNA: Predictive modeling by nonlinear lattice dynamics.* **Phys. Rev. E**. **vol.** 82, **no.** 2 (**2010**), p. 021905. DOI: 10.1103/PhysRevE.82.021905 (see p. 8).

[126] S. Venkataraman, R. M. Dirks, P. W. K. Rothemund, E. Winfree, and N. a. Pierce. *An autonomous polymerization motor powered by DNA hybridization.* **Nat. Nanotechnol. vol.** 2, **no.** 8 (**2007**), pp. 490–4. DOI: 10.1038/nnano.2007.225 (see p. 16).

[127] N. Verellen, Y. Sonnefraud, H. Sobhani, F. Hao, V. V. Moshchalkov, P. Van Dorpe, P. Nordlander, and S. a. Maier. *Fano resonances in individual coherent plasmonic nanocavities.* **Nano Lett. vol.** 9, **no.** 4 (**2009**), pp. 1663–7. DOI: 10.1021/nl9001876 (see p. 47).

[128] N. V. Voigt, T. Torring, A. Rotaru, M. F. Jacobsen, J. B. Ravnsbaek, R. Subramani, W. Mamdouh, J. r. Kjems, A. Mokhir, F. Besenbacher, and K. V. Gothelf. *Single-molecule chemical reactions on DNA origami.* **Nat. Nanotechnol. vol.** 5, **no.** 3 (**2010**), pp. 200–3. DOI: 10.1038/nnano.2010.5 (see p. 16).

[129] R. Weaver. *Molecular Biology*. McGraw Hil. New York, NY, **2012** (see p. 5).

[130] B. Wei, M. Dai, and P. Yin. *Complex shapes self-assembled from single-stranded DNA tiles.* **Nature**. **vol.** 485, **no.** 7400 (**2012**), pp. 623–6. DOI: 10.1038/nature11075 (see p. 15).

[131] S. F. J. Wickham, M. Endo, Y. Katsuda, K. Hidaka, J. Bath, H. Sugiyama, and A. J. Turberfield. *Direct observation of stepwise movement of a synthetic molecular transporter.* **Nat. Nanotechnol. vol.** 6, **no.** 3 (**2011**), pp. 166–9. DOI: 10.1038/nnano.2010.284 (see p. 16).

[132] O. I. Wilner, S. Shimron, Y. Weizmann, Z.-g. Wang, and I. Willner. *Self-Assembly of Enzymes on DNA Scaffolds : En Route to Biocatalytic Nanowires 2009* (**2009**), pp. 5–8 (see p. 17).

[133] E. Winfree, F. Liu, L. a. Wenzler, and N. C. Seeman. *Design and self-assembly of two-dimensional DNA crystals.* **Nature**. **vol.** 394, **no.** 6693 (**1998**), pp. 539–44. DOI: 10.1038/28998 (see p. 13).

[134] P. Yakovchuk, E. Protozanova, and M. D. Frank-Kamenetskii. *Base-stacking and base-pairing contributions into thermal stability of the DNA double helix.* **Nucleic Acids Res. vol.** 34, **no.** 2 (**2006**), pp. 564–74. DOI: 10.1093/nar/gkj454 (see p. 6).

[135] H. Yan, S. H. Park, G. Finkelstein, J. H. Reif, and T. H. LaBean. *DNA-templated self-assembly of protein arrays and highly conductive nanowires.* **Science**. **vol.** 301, **no.** 5641 (**2003**), pp. 1882–4. DOI: 10.1126/science.1089389 (see p. 17).

[136] Y. Yang, J. M. Callahan, T.-h. Kim, A. S. Brown, and H. O. Everitt. *Ultraviolet Nanoplasmonics: A Demonstration of Surface-Enhanced Raman Spectroscopy, Fluorescence, and Photodegradation Using Gallium Nanoparticles* (**2013**) (see pp. 64, 65).

[137] J. Ye, F. Wen, H. Sobhani, J. B. Lassiter, P. Van Dorpe, P. Nordlander, and N. J. Halas. *Plasmonic nanoclusters: near field properties of the Fano resonance interrogated with SERS.* **Nano Lett. vol.** 12, **no.** 3 (**2012**), pp. 1660–7. DOI: 10.1021/nl3000453 (see p. 60).

[138] B. Yurke, A. J. Turberfield, A. P. Mills, F. C. Simmel, and J. L. Neumann. *A DNA-fuelled molecular machine made of DNA.* **Nature**. **vol.** 406, **no.** 6796 (**2000**), pp. 605–8. DOI: 10.1038/35020524 (see pp. 15, 16).

[139] J. N. Zadeh, C. D. Steenberg, J. S. Bois, B. R. Wolfe, M. B. Pierce, A. R. Khan, R. M. Dirks, and N. A. Pierce. *Software News and Updates NUPACK : Analysis and Design of Nucleic Acid Systems* (**2010**). DOI: 10.1002/jcc (see pp. 4, 12).

[140] D. Zanchet, C. M. Micheel, W. J. Parak, D. Gerion, and a. P. Alivisatos. *Electrophoretic Isolation of Discrete Au Nanocrystal/DNA Conjugates*. **Nano Lett. vol.** 1, **no.** 1 (**2001**), pp. 32–35. DOI: 10.1021/nl005508e (see pp. 18, 81).

[141] D. Y. Zhang and G. Seelig. *Dynamic DNA nanotechnology using strand-displacement reactions*. **Nat. Chem. vol.** 3, **no.** 2 (**2011**), pp. 103–13. DOI: 10.1038/nchem.957 (see p. 15).

[142] X. Zhang, M. R. Servos, and J. Liu. *Fast pH-assisted functionalization of silver nanoparticles with monothiolated DNA*. **Chem. Commun. (Camb). vol.** 48, **no.** 81 (**2012**), pp. 10114–6. DOI: 10.1039/c2cc35008d (see p. 29).

[143] X. Zhang, M. R. Servos, and J. Liu. *Instantaneous and quantitative functionalization of gold nanoparticles with thiolated DNA using a pH-assisted and surfactant-free route*. **J. Am. Chem. Soc. vol.** 134, **no.** 17 (**2012**), pp. 7266–9. DOI: 10.1021/ja3014055 (see p. 29).

[144] X. Zhang, M. R. Servos, and J. Liu. *Surface science of DNA adsorption onto citrate-capped gold nanoparticles*. **Langmuir**. **vol.** 28, **no.** 8 (**2012**), pp. 3896–902. DOI: 10.1021/la205036p (see p. 29).

[145] Z. Zhao, Y. Liu, and H. Yan. *Organizing DNA origami tiles into larger structures using preformed scaffold frames*. **Nano Lett. vol.** 11, **no.** 7 (**2011**), pp. 2997–3002. DOI: 10.1021/nl201603a (see p. 15).

[146] M. Zuker and P. Stiegler. *Optimal computer folding of large RNA sequences using thermodynamics and auxiliary information*. **Nucleic Acids Res. vol.** 9, **no.** 1 (**1981**), pp. 133–148. DOI: 10.1093/nar/9.1.133 (see p. 12).

Biography

Originally from Lima, Peru, Mauricio Pilo-Pais migrated to the United States in July of 2000. He commenced his studies in Physics attending Broward Community College in 2004, and then transferred to University of Florida in 2006. He obtained a dual B.S. in Physics and Chemistry in 2008 while working under guidance of Prof. Neil Sullivan. In 2009, Mauricio entered Duke University where he joined the group of Prof. Gleb Finkelstein. There, he completed a Ph.D. in Physics and a M.Sc. in Computer and Electrical Engineering. His current research focuses on studying optical phenomena of DNA-based self-assembled structures. After graduation, Mauricio plans to do a post-doctorate at Tim Liedl's group at the Ludwig Maximilian University of Munich (LMU).

Degrees and Certificates

- B.S. in Physics (University of Florida)
- B.S. in Chemistry (University of Florida)
- M.Sc. in Computer and Electrical Engineering (Duke University)
- Ph.D. in Physics (Duke University)
- Certificate in Nanoscience (Duke University)
- Certificate in Photonics (Fitzpatrick Institute for Photonics (FIP) - Duke University)

Publications

- M. Pilo-Pais, A. Watson, S. Demers, T. H. LaBean, and G. Finkelstein. *Surface-enhanced Raman scattering plasmonic enhancement using DNA origami-based complex metallic nanostructures.* **Nano Lett. vol.** 14, **no.** 4 (**2014**), pp. 2099–104. DOI: 10.1021/nl5003069

- M. Pilo-Pais, S. Goldberg, E. Samano, T. H. Labean, and G. Finkelstein. *Connecting the nanodots: programmable nanofabrication of fused metal shapes on DNA templates.* **Nano Lett. vol.** 11, **no.** 8 (**2011**), pp. 3489–3492. DOI: 10.1021/nl202066c

- E. C. Samano, M. Pilo-Pais, S. Goldberg, B. N. Vogen, G. Finkelstein, and T. H. LaBean. *Self-assembling DNA templates for programmed artificial biomineralization.* **Soft Matter**. **vol.** 7, **no.** 7 (**2011**), p. 3240. DOI: 10.1039/c0sm01318h